SAPIENZA
UNIVERSITÀ DI ROMA

SAPIENZA, University of Rome

DEPARTMENT OF MECHANICAL AND AEROSPATIAL ENGINEERING
Theoretical and Applied Mechanics XXV Ph.D. Course

Large scale and small scale turbulence in an orifice jet: experimental study based on planar and volumetric techniques

Candidate:
Giovanni Lacagnina

Thesis advisor:
Professor Giovanni Paolo Romano

Thesis submitted in 2012

Contents

Chapter 1

Introduction

Turbulence is one of the bases of natural phenomena involving fluid flows. Most of flows in natural environment and in engineering applications are turbulent, like for example interstellar gas clouds, jet streams in the upper troposphere, water currents below the surface of the oceans. In addition boundary layers on aircraft wings, the wakes of any vehicle and the flows of fluids in rivers, canals and pipelines are turbulent. In everyday life examples can be found in the smoke leaving a burning cigarette or in the plume of a smokestack.

One of the most studied turbulent phenomena are jets. They have a key role in many applications. For example most combustion processes involve turbulence and often depend on it, in the same way that chemical reactions in liquids or gases do. In general cooling/heating, drying, mixing and processes like gas-liquid separation or chemical vapor deposition (CVD) involve turbulent jets. Therefore studying jets phenomenon is useful to reach a deep knowledge of them in order to improve them.

There exist basically three different configurations to generate jet flows: smoothly contracting (*contoured*) nozzles, long pipes and orifice plates. Since now, most studies, especially on round jets, have been performed using contoured nozzles because they produce nearly uniform "top-hat" profiles at jet exit (Wygnanski and Fiedler (1969) [53], Hinze (1975) [12], Rodi (1975) [38], Townsend (1976) [46], Panchapasekan and Lumley(1993) [27], Hussein et al. (1994) [13], Lubbers et al. (2001) [21], Xu and Antonia (2002) [54]). Numerous studies have also been realized making use of long pipes (Richards and Pitts (1993) [36], Djeridane et al. (1996) [7], Mi et

al. (2001) [23]), which generate non-uniform velocity profiles describable empirically by a power law. By comparison, investigations on orifice plates flows are really fewer, probably because the initial velocity profile and the near field flow structures are more complex. However the orifice plate is easier to manufacture than the other configurations, especially when non circular shapes are involved. The mean feature of orifice jets is the existence of the *vena contracta* phenomenon. Due to the necessity for the flow to pass through the orifice, which has a limited diameter, the streamlines of the jet have to converge, figure 1.1. Then they should change direction to get the original parallel and horizontal one, but they are not able to perform it abruptly. Hence the contraction goes on a little further from the plate until the area of the jet becomes a minimum. This section is called *vena contracta* , see Falkovich (2011) [8]. There exists a characteristic dimensionless quantity, known as the coefficient of contraction C_c, which is the ratio between the area of the vena contracta A and the area of the orifice A_0.

$$C_c = \frac{A}{A_0}$$

For a sharp circular orifice its value is generally near to 0.6 [24], but it is also dependent on the specific shape of the contraction [3] and of the orifice, increasing in all of 10 per cent moving in order from the circular shape, to the square, the triangular and the rectangular [16]. Jets will be considered in detail in section 1.1.

Due to the complexity of the turbulent phenomena, many and many articles and books have been written on turbulence, starting from different points of view ([45], [29] and [9]). However, there exist several universal characteristics of turbulence, starting from the evidence that turbulence is not a feature of fluids but of fluid flows. Other features are: randomness of the phenomenon, therefore a statistical approach is needed; diffusivity, that involves high rates of momentum, heat and mass transfer; high Reynolds numbers; three-dimensionality and rotationality, flows substantially two-dimensional are not turbulent themselves because important vorticity-maintenance mechanisms like vortex stretching are absent in two-dimensional flow; and finally dissipation that implies a continuous supply of

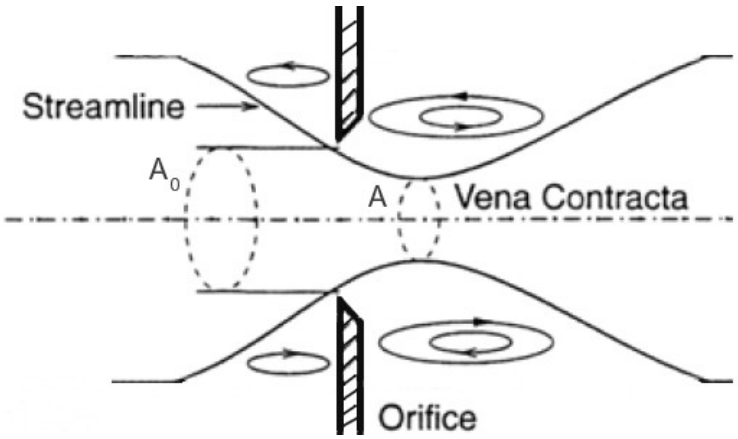

Figure 1.1: Sketch of an orifice jet

energy to make up for viscous losses. Another important characteristic can be enlightened by looking at any image of a turbulent flow, such as image 1.2. Turbulence can be considered to be composed of eddies of different size. At eddies of size l is associated a characteristic velocity *u(l)* and a characteristic timescale $\tau(l) = \frac{l}{u(l)}$. An eddie can't be easily defined, it can be described as a turbulent motion, localized within a region of size l and at least somewhat coherent over this region. A region occupied by a large eddie can also contain smaller eddies. The largest eddies are characterized by a lengthscale l_0, which is comparable to the flow scale L that is the characteristic scale of the phenomenon, e.g., the radius of a pipe through which fluid is flowing or the size of an object while studying its wake, and their own velocity $u_0 = u(l_0)$ is comparable to the characteristic velocity scale of the flow U.

The first contribution to the theory of turbulence was due to Richardson and his book of 1922 [37], according to which there exist a transfer of energy, called *energy cascade*, from the bigger scales toward the smaller ones. He concisely explained this notion using these words: *"Big whirls have little whirls that feed on their velocity, and little whirls have lesser whirls and so on to viscosity"*. The meaning is that the kinetic energy introduces energy at the large scales, this energy then is transferred to smaller and smaller scales, until it is dissipated by viscosity at the smallest scales. Putting the dissipation at the end of the sequence of events means that its amount can be quantified by the first term in the sequence,

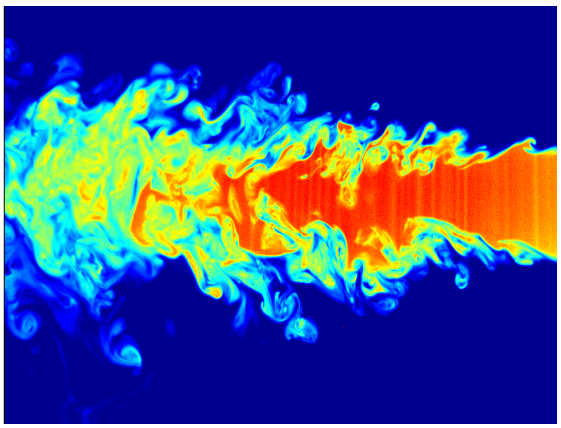

Figure 1.2: LIF visualization of a turbulent jet (Author's Master Degree Thesis)

that is the transfer of energy from the largest eddies. This concept has been refined later but remains still the basis of all the following theories.

The next important contribution was the one of Kolmogorov in 1941, with the publication of two famous works [18] [17], who laid the foundations for the phenomenology of turbulence as we know it, with a partial correction in 1962 by the same author to reply to the experimental evidences about intermittency of turbulent kinetic energy dissipation. Based on his studies on stochastic processes, he came to the conclusion that someway, at the scales where energy dissipation occurs, there exists a universality so that the features of the flow at large scales disappear at small scales. Starting from here he stated three hypothesis, which can be resumed in a shorter form [29]:

Kolmogorov's hypothesis of local isotropy: *At sufficiently high Reynolds numbers, the small-scales turbulent motions are statistically isotropic.*

According to this hypothesis, the velocity field is supposed to be invariant to rotation and reflection for every scale $l < l_0$. For example the large eddies are anisotropic and influenced by the boundary conditions of the flow but the vortex stretching mechanism, that reduces the eddies size, occurs in a random way, changing vortex orientation in a three-dimensional space, so that, at small scales, all the original orientation is lost and every flow appears similar. That is isotropy can be assumed at the smaller scales. Moreover can be assumed that no direct interaction exists between large and small eddies, there exists only an interaction through the velocity fluctuations of intermediate vortices.

Based on this hypothesis and on a dimensional analysis, he could state the second hypothesis:

Kolmogorov's first similarity hypothesis : *In every turbulent flow at sufficiently high Reynolds number, the statistics of the small-scale motions have a universal form that is uniquely determined by ν and ϵ.*

According to this hypothesis can be stated that at small scales the structure functions, which are the statistical moments of the velocity increments between two points at a distance r, depend only on the spacing r, on the mean turbulent kinetic energy dissipation ϵ_T and on the kinematic viscosity ν. Therefore it can be written that:

$$\langle \delta u_{\parallel}^{k} \rangle = S_k(r, \epsilon_T, \nu) \tag{1.1}$$

In this expression the angle brackets $\langle\rangle$ denote an ensemble averaging, while S_k is the generic structure function of k-th order. The symbol $\parallel$ reminds that the velocity increment is evaluated in the streamwise direction. If $\underline{l}$ identifies this direction, we have by definition that:

$$\delta u_{\parallel} = \delta u \cdot \underline{l} \tag{1.2}$$

The scale η at which the condition 1.1 is met, called Kolmogorov's scale or dissipative scale, is identified by the relation:

$$\eta = \left[\frac{\nu^3}{\langle \epsilon_T \rangle} \right]^{\frac{1}{4}} \tag{1.3}$$

Again basing on the first hypothesis and on a dimensional analysis, Kolmogorov stated:

Kolmogorov's second similarity hypothesis : *In every turbulent flow at sufficiently high Reynolds number, the statistics of the motions of scale l in the range $l_0 \gg l \gg \eta$ have a universal form that is uniquely determined by ϵ, independent of ν.*

In this range of scales, called inertial range, therefore the structure functions depend only on the spacing r and on the mean turbulent kinetic energy dissipation ϵ_T. Then it can be assumed that the viscosity effect in a turbulent flow can be felt only in correspondence to scales of the order of η.

Kolmogorov obtained an equation which links the structure functions of different order (second and third order) and the turbulent dissipation. It

is one of the few exact, but non-trivial, results in the statistical theory of isotropic turbulence and is valid in the limit $r << L$:

$$\left\langle (\delta u_{\parallel})^3 \right\rangle - 6\nu \frac{d\langle (\delta u_{\parallel})^2 \rangle}{dr} = -\frac{4}{5}\langle \epsilon_T \rangle r \tag{1.4}$$

In the inertial range, over which kinematic viscosity effects are negligible, this equation becomes:

$$\left\langle (\delta u_{\parallel})^3 \right\rangle = -\frac{4}{5}\langle \epsilon_T \rangle r \tag{1.5}$$

From here it can be evaluated that

$$\delta u_{\parallel} \simeq \epsilon_T^{\frac{1}{3}} r^{\frac{1}{3}} \tag{1.6}$$

Writing the equation 1.4 in correspondence to the dissipative scales and adimensionalizing it, the following expression can be obtained:

$$\frac{6}{Re} \frac{d\left\langle (\delta u_{\parallel})^2 \right\rangle}{dr} = \frac{4}{5} \left\langle \epsilon_T \right\rangle r \tag{1.7}$$

So that first and second member be equal in the limit as r approaches zero, must be

$$\delta u_{\parallel} \propto r$$

From which can be deduced that

$$\frac{\left\langle (\delta u_{\parallel})^2 \right\rangle}{r^2} = \frac{2}{15} Re \left\langle \epsilon_T \right\rangle \tag{1.8}$$

The passage from the inertial to the diffusive range happens in correspondence to η.The Kolmogorov's scale can then be evaluated by requiring that the inertial velocity increment $\delta u_{\parallel} \propto \epsilon_T^{\frac{1}{3}} r^{\frac{1}{3}}$ be equal to the diffusive one $\delta u_{\parallel} \propto \sqrt{Re\epsilon_t} r$. This condition becomes:

$$\epsilon_T^{\frac{1}{3}} \eta^{\frac{1}{3}} = \sqrt{Re\epsilon_t}\eta$$

Involving that:

$$\eta = \epsilon_T^{-\frac{1}{4}} Re^{-\frac{3}{4}} \tag{1.9}$$

This expression implies that the higher the Reynolds number is, the

lower is the Kolmogorov's scale and the study of the turbulence as a whole becomes harder.

In addition to the basic statistics such as turbulent intensities, researchers are also interested in higher order quantities like the turbulent kinetic energy dissipation rate ϵ_T. This quantity is of interest because it is essential to characterize the smallest scales of turbulent motion, allows closure of energy budgets, and it is essential for verifying assumptions on turbulence characterization. In general, it is defined as [12]:

$$\epsilon_T = \nu \left(\left\langle \frac{\partial u_i}{\partial x_j} \frac{\partial u_i}{\partial x_j} \right\rangle + \left\langle \frac{\partial u_i}{\partial x_j} \frac{\partial u_j}{\partial x_i} \right\rangle \right) \text{ for } i, j = 1, ..., 3 \tag{1.10}$$

u_i and u_j are the generic velocity components, ν denotes the kinematic viscosity and the indexes i and j identify the orthogonal axes set. Writing explicitly its terms, equation 1.10 becomes:

$$\begin{aligned} \epsilon_T =& \nu \left\{ 2 \left[\left\langle \left(\frac{\partial u}{\partial x} \right)^2 \right\rangle + \left\langle \left(\frac{\partial v}{\partial y} \right)^2 \right\rangle + \left\langle \left(\frac{\partial w}{\partial z} \right)^2 \right\rangle \right] \right. \\ &+ \left[\left\langle \left(\frac{\partial u}{\partial y} \right)^2 \right\rangle + \left\langle \left(\frac{\partial v}{\partial x} \right)^2 \right\rangle + \left\langle \left(\frac{\partial u}{\partial z} \right)^2 \right\rangle \right. \\ &\left. + \left\langle \left(\frac{\partial w}{\partial x} \right)^2 \right\rangle + \left\langle \left(\frac{\partial v}{\partial z} \right)^2 \right\rangle + \left\langle \left(\frac{\partial w}{\partial y} \right)^2 \right\rangle \right] \\ &\left. + 2 \left(\left\langle \frac{\partial u}{\partial y} \frac{\partial v}{\partial x} \right\rangle + \left\langle \frac{\partial u}{\partial z} \frac{\partial w}{\partial x} \right\rangle + \left\langle \frac{\partial v}{\partial z} \frac{\partial w}{\partial y} \right\rangle \right) \right\} \end{aligned} \tag{1.11}$$

The intrinsic difficulty of evaluating this quantity is now clear. Making reference to the local isotropy hypothesis [18], some relations hold [12] :

$$\left\langle \left(\frac{\partial u}{\partial x} \right)^2 \right\rangle = \left\langle \left(\frac{\partial v}{\partial y} \right)^2 \right\rangle = \left\langle \left(\frac{\partial w}{\partial z} \right)^2 \right\rangle \tag{1.12}$$

$$\begin{aligned} 2 \left\langle \left(\frac{\partial u}{\partial x} \right)^2 \right\rangle &= \left\langle \left(\frac{\partial u}{\partial y} \right)^2 \right\rangle = \left\langle \left(\frac{\partial u}{\partial z} \right)^2 \right\rangle = \left\langle \left(\frac{\partial v}{\partial x} \right)^2 \right\rangle \\ &= \left\langle \left(\frac{\partial v}{\partial z} \right)^2 \right\rangle = \left\langle \left(\frac{\partial w}{\partial x} \right)^2 \right\rangle = \left\langle \left(\frac{\partial w}{\partial y} \right)^2 \right\rangle \end{aligned} \tag{1.13}$$

$$\left\langle \left(\frac{\partial v}{\partial x}\right)\left(\frac{\partial u}{\partial y}\right)\right\rangle = \left\langle \left(\frac{\partial w}{\partial y}\right)\left(\frac{\partial v}{\partial z}\right)\right\rangle = \left\langle \left(\frac{\partial u}{\partial z}\right)\left(\frac{\partial w}{\partial x}\right)\right\rangle = \frac{1}{2}\left\langle \left(\frac{\partial u}{\partial x}\right)^2\right\rangle \tag{1.14}$$

Making use of these relations, equation 1.11 gets a more simple expression associated to a single quantity, e.g. the mean quadratic derivative of streamwise velocity with respect to the streamwise coordinate:

$$\epsilon_T = 15\nu\left\langle \left(\frac{\partial u}{\partial x}\right)^2\right\rangle \tag{1.15}$$

This advantageous hypothesis still awaits confirmations both numerically and experimentally and certainly for orifice jets. There exists a different formulation, firstly expressed by Batchelor (1946) [2] and Chandrasekhar (1950) [6] and then proposed by George and Hussein more recently (1991) [11], based on the less stringent hypothesis of axial symmetry to rotation. Thanks to this approximation, the functional dependency of equation 1.11 can be reduced to four quantities, e.g., in the plane (x,y), the derivatives of velocity components in the same plane, useful in planar velocity measurements.

$$\epsilon_T = \nu\left[-\left\langle \left(\frac{\partial u}{\partial x}\right)^2\right\rangle + 2\left\langle \left(\frac{\partial u}{\partial y}\right)^2\right\rangle + 2\left\langle \left(\frac{\partial v}{\partial x}\right)^2\right\rangle + 8\left\langle \left(\frac{\partial v}{\partial y}\right)^2\right\rangle\right]$$

Nowadays, is still not clear under which conditions a phenomenon shows local isotropy or axial symmetry conditions or others, albeit a good amount of works have confirmed the goodness of the second one in correspondence to several turbulent flows, such as quasi-homogeneous shear flows, boundary layers, pipe jets, circular jets, round plumes, plane jets, mixing layers and two dimensional cylinder wakes [11]. This has rarely been studied on orifice jets [40]. A possible way of testing the fulfillment of those conditions is making use of some non-dimensional parameters [11]. They are:

$$K_1 = \frac{\left\langle \left(\frac{\partial v}{\partial y}\right)^2\right\rangle}{\left\langle \left(\frac{\partial u}{\partial x}\right)^2\right\rangle}\ K_2 = \frac{\left\langle \left(\frac{\partial w}{\partial z}\right)^2\right\rangle}{\left\langle \left(\frac{\partial u}{\partial x}\right)^2\right\rangle}\ K_3 = \frac{\left\langle \left(\frac{\partial u}{\partial y}\right)^2\right\rangle}{\left\langle \left(\frac{\partial u}{\partial x}\right)^2\right\rangle} \tag{1.16}$$

$$K_4 = \frac{\left\langle \left(\frac{\partial v}{\partial x}\right)^2 \right\rangle}{\left\langle \left(\frac{\partial u}{\partial x}\right)^2 \right\rangle} \; K_5 = \frac{\left\langle \left(\frac{\partial u}{\partial z}\right)^2 \right\rangle}{\left\langle \left(\frac{\partial u}{\partial x}\right)^2 \right\rangle} \; K_6 = \frac{\left\langle \left(\frac{\partial w}{\partial x}\right)^2 \right\rangle}{\left\langle \left(\frac{\partial u}{\partial x}\right)^2 \right\rangle} \tag{1.17}$$

$$K_7 = \frac{\left\langle \left(\frac{\partial v}{\partial z}\right)^2 \right\rangle}{\left\langle \left(\frac{\partial u}{\partial x}\right)^2 \right\rangle} \; K_8 = \frac{\left\langle \left(\frac{\partial w}{\partial y}\right)^2 \right\rangle}{\left\langle \left(\frac{\partial u}{\partial x}\right)^2 \right\rangle} \; K_9 = \frac{\left\langle \frac{\partial u}{\partial y}\frac{\partial v}{\partial x} \right\rangle}{\left\langle \left(\frac{\partial u}{\partial x}\right)^2 \right\rangle} \tag{1.18}$$

$$K_{10} = \frac{\left\langle \frac{\partial u}{\partial z}\frac{\partial w}{\partial x} \right\rangle}{\left\langle \left(\frac{\partial u}{\partial x}\right)^2 \right\rangle} \; K_{11} = \frac{\left\langle \frac{\partial v}{\partial z}\frac{\partial w}{\partial y} \right\rangle}{\left\langle \left(\frac{\partial u}{\partial x}\right)^2 \right\rangle} \tag{1.19}$$

With the aim of confirming axial symmetry, some different parameters can be introduced [11]:

$$\begin{aligned} R_1 &= \frac{\frac{1}{3}\left\langle \left(\frac{\partial u}{\partial x}\right)^2 \right\rangle + \frac{1}{3}\left\langle \left(\frac{\partial v}{\partial z}\right)^2 \right\rangle}{\left\langle \left(\frac{\partial v}{\partial y}\right)^2 \right\rangle} \\ R_2 &= \frac{\frac{1}{6}\left\langle \left(\frac{\partial u}{\partial x}\right)^2 \right\rangle - \frac{1}{3}\left\langle \left(\frac{\partial v}{\partial z}\right)^2 \right\rangle}{\left\langle \frac{\partial v}{\partial z}\frac{\partial w}{\partial y} \right\rangle} \end{aligned} \tag{1.20}$$

The expected value of these non-dimensional parameters, if the isotropy hypotheses were fulfilled, has been evaluated by Taylor in his paper in 1935 [44]. Starting from equation 1.11, simply stating the statistical isotropy allows to obtain the following relations:

$$\left\langle \left(\frac{\partial u}{\partial x}\right)^2 \right\rangle = \left\langle \left(\frac{\partial v}{\partial y}\right)^2 \right\rangle = \left\langle \left(\frac{\partial w}{\partial z}\right)^2 \right\rangle \tag{1.21}$$

$$\left\langle \left(\frac{\partial u}{\partial y}\right)^2 \right\rangle = \left\langle \left(\frac{\partial u}{\partial z}\right)^2 \right\rangle = \left\langle \left(\frac{\partial v}{\partial x}\right)^2 \right\rangle = \left\langle \left(\frac{\partial v}{\partial z}\right)^2 \right\rangle = \left\langle \left(\frac{\partial w}{\partial x}\right)^2 \right\rangle = \left\langle \left(\frac{\partial w}{\partial y}\right)^2 \right\rangle \tag{1.22}$$

$$\left\langle \left(\frac{\partial v}{\partial x}\right)\left(\frac{\partial u}{\partial y}\right) \right\rangle = \left\langle \left(\frac{\partial w}{\partial y}\right)\left(\frac{\partial v}{\partial z}\right) \right\rangle = \left\langle \left(\frac{\partial u}{\partial z}\right)\left(\frac{\partial w}{\partial x}\right) \right\rangle \tag{1.23}$$

which lead to a new expression of equation 1.11:

$$\epsilon_T = 6\nu \left[\left\langle \left(\frac{\partial u}{\partial x} \right)^2 \right\rangle + \left\langle \left(\frac{\partial u}{\partial y} \right)^2 \right\rangle + \left\langle \left(\frac{\partial v}{\partial x} \right) \left(\frac{\partial u}{\partial y} \right) \right\rangle \right] \tag{1.24}$$

All the three terms of this equation are related to each other, so quantifying one of them implies the knowledge of the value of the other two. In order to demonstrate this, a first relation is obtained making use of the condition of continuity:

$$\frac{\partial u}{\partial x} + \frac{\partial v}{\partial y} + \frac{\partial w}{\partial z} = 0.$$

From which can be obtained:

$$\frac{\partial u}{\partial x}^2 + \frac{\partial v}{\partial y}^2 + \frac{\partial w}{\partial z}^2 = -2 \left(\frac{\partial u}{\partial x} \frac{\partial v}{\partial y} + \frac{\partial v}{\partial y} \frac{\partial w}{\partial z} + \frac{\partial w}{\partial z} \frac{\partial u}{\partial x} \right). \tag{1.25}$$

therefore

$$\left\langle \left(\frac{\partial u}{\partial x} \right)^2 \right\rangle = -2 \left\langle \frac{\partial u}{\partial x} \frac{\partial v}{\partial y} \right\rangle \tag{1.26}$$

Consider all the possible combinations of the quantities

$$\begin{array}{c} \frac{\partial u}{\partial x}; \frac{\partial v}{\partial x}; \frac{\partial w}{\partial x} \\ \frac{\partial u}{\partial y}; \frac{\partial v}{\partial y}; \frac{\partial w}{\partial y} \\ \frac{\partial u}{\partial z}; \frac{\partial v}{\partial z}; \frac{\partial w}{\partial z} \end{array} \tag{1.27}$$

taken 2 at a time. They are in all 45 which, when the motion is statistically isotropic, can be divided into 10 groups of equal elements, table 1.1.

Equation 1.24 can be expressed in terms of these symbols:

$$\epsilon_T = \nu(6a_1 + 6a_3 + 6a_8) \tag{1.28}$$

as well as the relation 1.26:

$\left\langle \left(\frac{\partial u}{\partial x}\right)^2 \right\rangle$	$\left\langle \frac{\partial u}{\partial x}\frac{\partial u}{\partial y} \right\rangle$	$\left\langle \left(\frac{\partial u}{\partial y}\right)^2 \right\rangle$	$\left\langle \frac{\partial u}{\partial y}\frac{\partial u}{\partial z} \right\rangle$	$\left\langle \frac{\partial u}{\partial x}\frac{\partial v}{\partial x} \right\rangle$
a_1	a_2	a_3	a_4	a_5
$\left\langle \frac{\partial u}{\partial x}\frac{\partial v}{\partial y} \right\rangle$	$\left\langle \frac{\partial u}{\partial x}\frac{\partial v}{\partial z} \right\rangle$	$\left\langle \frac{\partial u}{\partial y}\frac{\partial v}{\partial x} \right\rangle$	$\left\langle \frac{\partial u}{\partial y}\frac{\partial v}{\partial z} \right\rangle$	$\left\langle \frac{\partial u}{\partial z}\frac{\partial v}{\partial z} \right\rangle$
a_6	a_7	a_8	a_9	a_{10}

Table 1.1

$$a_1 = -2a_6$$

Further relations can be obtained as follows. Simply transform u, v, w, x, y, z by rotating the x and y axes through 45° around the z axis so that:

$$\sqrt{2}x' = x + y \qquad \sqrt{2}u' = u + v \tag{1.29}$$

$$\sqrt{2}y' = -x + y \qquad \sqrt{2}v' = -u + v \tag{1.30}$$

$$z' = z \qquad w' = w \tag{1.31}$$

Hence

$$\frac{\partial u}{\partial x} = \frac{1}{2}\left(\frac{\partial u'}{\partial x'} - \frac{\partial v'}{\partial x'} - \frac{\partial u'}{\partial y'} + \frac{\partial v'}{\partial y'}\right) \tag{1.32}$$

$$\frac{\partial v}{\partial x} = \frac{1}{2}\left(\frac{\partial u'}{\partial x'} + \frac{\partial v'}{\partial x'} - \frac{\partial u'}{\partial y'} - \frac{\partial v'}{\partial y'}\right) \tag{1.33}$$

$$\frac{\partial w}{\partial x} = \frac{1}{\sqrt{2}}\left(\frac{\partial w'}{\partial x'} - \frac{\partial w'}{\partial y'}\right) \tag{1.34}$$

$$\frac{\partial u}{\partial y} = \frac{1}{2}\left(\frac{\partial u'}{\partial x'} - \frac{\partial v'}{\partial x'} + \frac{\partial u'}{\partial y'} - \frac{\partial v'}{\partial y'}\right) \tag{1.35}$$

$$\frac{\partial v}{\partial y} = \frac{1}{2}\left(\frac{\partial u'}{\partial x'} + \frac{\partial v'}{\partial x'} + \frac{\partial u'}{\partial y'} + \frac{\partial v'}{\partial y'}\right) \tag{1.36}$$

$$\frac{\partial w}{\partial y} = \frac{1}{\sqrt{2}}\left(\frac{\partial w'}{\partial x'} + \frac{\partial w'}{\partial y'}\right) \tag{1.37}$$

$$\frac{\partial u}{\partial z} = \frac{1}{\sqrt{2}}\left(\frac{\partial u'}{\partial z'} - \frac{\partial v'}{\partial z'}\right) \tag{1.38}$$

$$\frac{\partial v}{\partial z} = \frac{1}{\sqrt{2}}\left(\frac{\partial u'}{\partial z'} + \frac{\partial v'}{\partial z'}\right) \tag{1.39}$$

$$\frac{\partial w}{\partial z} = \frac{\partial w'}{\partial z'} \tag{1.40}$$

As an example, take the term $\left\langle \left(\frac{\partial u}{\partial x}\right)^2 \right\rangle = a_1$. Taking the mean value of the square of the transformed expression of $\left(\frac{\partial u}{\partial x}\right)$ and substituting the symbols of table 1.1 can be found that

$$\begin{aligned}\left\langle \left(\frac{\partial u}{\partial x}\right)^2 \right\rangle = a_1 &= \frac{1}{4}\left\{ \left(\frac{\partial u'}{\partial x'}\right)^2 + \left(\frac{\partial v'}{\partial x'}\right)^2 + ... + \left\langle \frac{\partial u'}{\partial x'}\frac{\partial v'}{\partial x'} \right\rangle .... \right\} \\ &= \frac{1}{2}(a_1 + a_3 - a_5 - a_2 + a_6 + a_8 - a_2 - a_5).\end{aligned} \tag{1.41}$$

Similarly

$$\left\langle \left(\frac{\partial v}{\partial y}\right)^2 \right\rangle = a_1 = \frac{1}{2}(a_1 + a_3 + a_5 + a_2 + a_6 + a_8 + a_2 + a_5). \tag{1.42}$$

$$\left\langle \left(\frac{\partial u}{\partial y}\right)^2 \right\rangle = a_3 = \frac{1}{2}(a_1 + a_3 - a_5 + a_2 - a_6 - a_8 + a_2 - a_5). \tag{1.43}$$

$$\left\langle \left(\frac{\partial v}{\partial x}\right)^2 \right\rangle = a_3 = \frac{1}{2}(a_1 + a_3 + a_5 - a_2 - a_6 - a_8 - a_2 + a_5). \tag{1.44}$$

These equations imply that:

$$a_2 = a_5 = 0$$

and

$$a_1 - a_3 - a_6 - a_8 = 0$$

.

Then transforming the terms a_2, a_5, a_6 and a_8 doesn't add more information which instead derives from the terms involving w or z.

$$\left\langle \frac{\partial u}{\partial z}\frac{\partial v}{\partial z} \right\rangle = a_{10} = \frac{1}{2}\left\{ \left(\frac{\partial u'}{\partial z'}\right)^2 - \left(\frac{\partial v'}{\partial z'}\right)^2 \right\} = \frac{1}{2}(a_3 - a_3) = 0 \qquad (1.45)$$

$$\left\langle \frac{\partial u}{\partial y}\frac{\partial v}{\partial z} \right\rangle = a_9 = \frac{1}{2\sqrt{2}}(a_2 - a_9 + a_4 - a_7 + a_7 - a_4 + a_9 - a_2) = 0 \quad (1.46)$$

$$\left\langle \frac{\partial u}{\partial x}\frac{\partial v}{\partial z} \right\rangle = a_7 = \frac{1}{2\sqrt{2}}(a_2 - a_9 - a_4 + a_7 + a_7 - a_4 - a_9 + a_2). \qquad (1.47)$$

Hence, since $a_2 = a_9 = 0$,

$$a_7\left(\sqrt{2} - 1\right) + a_4 = 0 \qquad (1.48)$$

$$\left\langle \frac{\partial u}{\partial y}\frac{\partial u}{\partial z} \right\rangle = a_4 = \frac{1}{2\sqrt{2}}(a_2 - a_9 + a_4 - a_7 - a_7 + a_4 - a_9 + a_2). \qquad (1.49)$$

hence

$$a_4\left(\sqrt{2} - 1\right) + a_7 = 0 \qquad (1.50)$$

The relations 1.48 and 1.50 imply that

$$a_4 = a_7 = 0. \qquad (1.51)$$

So far it has been found that 6 of the 10 elements, namely a_2, a_4, a_5, a_7, a_9 and a_{10} are equal to zero, while have been obtained two relations between the remaining 4 elements, which are:

$$a_1 = -2a_6$$

and

$$a_1 - a_3 - a_6 - a_8 = 0$$

Performing a volume integration on the turbulent dissipation as expressed in equation 1.11, can be obtained one further relation. This integration has been shown by Lamb in his book in 1895 [19], it is:

$$\begin{aligned}
\iiint \frac{\epsilon_T}{\nu}\partial x\partial y\partial z &= \iiint \left\{ 2\left[\left\langle \left(\frac{\partial u}{\partial x}\right)^2 \right\rangle + \left\langle \left(\frac{\partial v}{\partial y}\right)^2 \right\rangle + \left\langle \left(\frac{\partial w}{\partial z}\right)^2 \right\rangle \right] \right. \\
&+ \left[\left\langle \left(\frac{\partial u}{\partial y}\right)^2 \right\rangle + \left\langle \left(\frac{\partial v}{\partial x}\right)^2 \right\rangle + \left\langle \left(\frac{\partial u}{\partial z}\right)^2 \right\rangle + \left\langle \left(\frac{\partial w}{\partial x}\right)^2 \right\rangle + \left\langle \left(\frac{\partial v}{\partial z}\right)^2 \right\rangle + \left\langle \left(\frac{\partial w}{\partial y}\right)^2 \right\rangle \right] \\
&\left. +2\left(\left\langle \frac{\partial u}{\partial y}\frac{\partial v}{\partial x} \right\rangle + \left\langle \frac{\partial u}{\partial z}\frac{\partial w}{\partial x} \right\rangle + \left\langle \frac{\partial v}{\partial z}\frac{\partial w}{\partial y} \right\rangle \right) \right\} dx\, dy\, dz \\
&= \iiint \left(\xi^2 + \eta^2 + \zeta^2\right) dx\, dy\, dz - \iint \frac{\partial}{\partial n}(q^2) dS + 2\iint \begin{vmatrix} l & m & n \\ u & v & w \\ \xi & \eta & \zeta \end{vmatrix} dS
\end{aligned} \tag{1.52}$$

Where $\xi = \frac{\partial w}{\partial y} - \frac{\partial v}{\partial z}$, etc. The integrals are taken over the cloud surface S and through its volume. If the closed surface is large compared with the scale of the turbulence, the surface integrals are small compared with the volume integrals and therefore may be neglected. Averaging all the terms in equation 1.52 and using the symbology of table 1.1, can be obtained that

$$\frac{\epsilon_T}{\nu} = 6a_1 + 6a_3 + 6a_8 = 6a_3 - 6a_8 \tag{1.53}$$

Then

$$a_1 + 2a_8 = 0 \tag{1.54}$$

Finally from equations 1, 1 and 1.54 it can be obtained that:

$$a_1 = \frac{1}{2}a_3 = -2a_6 = -2a_8. \tag{1.55}$$

According to these last relations (equation 1.55), if local isotropy conditions were fulfilled we should get the following relations [11]:

$$K_1 = 1;\ K_2 = 1;\ K_3 = 2;\ K_4 = 2 \tag{1.56}$$

$$K_5 = 2;\ K_6 = 2;\ K_7 = 2;\ K_8 = 2 \tag{1.57}$$

$$K_9 = -0.5;\ K_{10} = -0.5;\ K_{11} = -0.5 \tag{1.58}$$

On the other hand, if the axial symmetry conditions were fulfilled, it would be got [11]:

$$\begin{gathered} K_1 = K_2;\ K_3 = K_5;\ K_4 = K_6; \\ K_7 = K_8;\ K_9 = K_{10} = -0.5 \\ K_1 = \frac{1}{3} + \frac{1}{3}K_7\ (that\ is\ R_1 = 1); \\ K_{11} = \frac{1}{6} - \frac{1}{3}K_7\ (that\ is\ R_2 = 1) \end{gathered} \tag{1.59}$$

As derived by Taylor [44], local homogeneity, that is the statistics of the velocity gradient field are independent of the location of the origin in space, yields for incompressible flows:

$$\begin{gathered} \left\langle \left(\frac{\partial v}{\partial x}\right)\left(\frac{\partial u}{\partial y}\right)\right\rangle + \left\langle \left(\frac{\partial u}{\partial z}\right)\left(\frac{\partial w}{\partial x}\right)\right\rangle + \left\langle \left(\frac{\partial w}{\partial y}\right)\left(\frac{\partial v}{\partial z}\right)\right\rangle = \\ \frac{1}{2}\left[\left\langle \left(\frac{\partial u}{\partial x}\right)^2\right\rangle + \left\langle \left(\frac{\partial v}{\partial y}\right)^2\right\rangle + \left\langle \left(\frac{\partial w}{\partial z}\right)^2\right\rangle\right] \end{gathered} \tag{1.60}$$

1.1 Jets

Jets are one of the most interesting phenomena in turbulence. Round jets have all a some common features of the flow field, especially in the far field. Some differences exist in the near field and orifice jets, as already pointed out, differ more from the other round jets, sufficing to cite vena contracta phenomenon [23]. First of all a right-handed Cartesian coordinate system has to be set univocally. It is shown in figure 1.3:

It has the x axis coinciding with the axis of the jet, while the y and z axes lie in the transversal plane.

The flow field of a round jet can be divided into three zones, [35]: the *core region* or *potential core*, the *flow-developing region* and the *flow-developed*

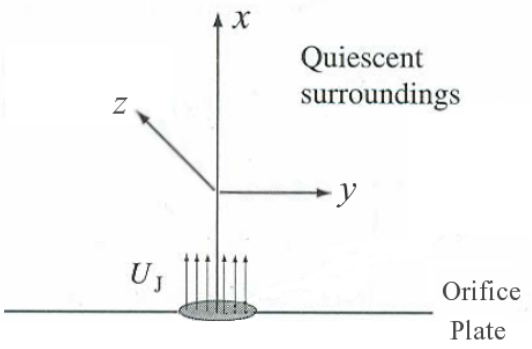

Figure 1.3: Coordinate system

region, which are shown in figure 1.4

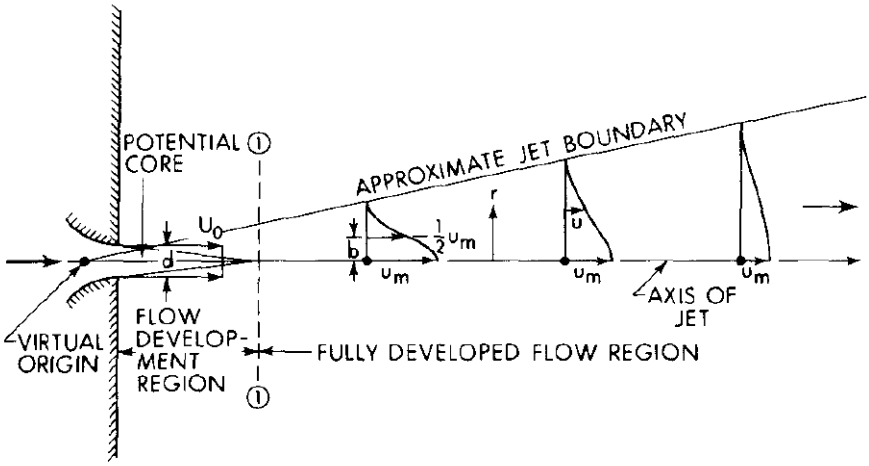

Figure 1.4: Jet sub-zones (taken from Rajaratnam 1976 [35])

The core region usually spans until $\frac{x}{D} = 4 - 5$, being D the jet exit diameter, in the jet flow direction and has a conical shape due to the increase, toward the axis of the jet, of the axisymmetrical mixing layer. In this zone, the majority of jets maintain a constant centreline velocity, equal to the initial one. This is not true for orifice jets, which in the core region experience an acceleration of the fluid due to the vena contracta effect and reach their maximum velocity at the end of this zone. Then the flow-developing region in which the centreline velocity starts to decrease and the jet to spread into the ambient fluid. The extent of this zone depends on the initial and boundary conditions but usually is near to 20-30 diameters. Finally the

flow-developed region whose characteristic is the *self-similarity* for all the quantities. It means that, once nondimensionalized using *ad hoc* variables, the fluid dynamic quantities show a behavior which is independent of the position along the axis of the jet. Making the local velocity U, i. e., non-dimensional by dividing it by the jet exit velocity U_0 and the transversal coordinate y non-dimensional by the so called jet's half-width $y_{\frac{1}{2}}$, which is the value of y where U is equal to half the centreline velocity, the radial profiles of $\frac{U}{U_0}$ against $\frac{y}{y_{\frac{1}{2}}}$ fall on one common curve [35].

Formalizing these results in a mathematical way, it can be written that, given the mean velocity field U(x,y,z), the centreline mean velocity is defined as

$$U_c(x) = U(x, 0, 0) \tag{1.61}$$

and the jet half width can be derived from

$$U(x, y_{\frac{1}{2}}, 0) = \frac{1}{2} U_c(x) \tag{1.62}$$

In the self-similar region the axial velocity decays with the axial distance according to a law [29] that can be fitted to

$$\frac{U_c(x)}{U_0} = \frac{B}{(x - x_0)/D} \tag{1.63}$$

where x_0 is the virtual origin, which is the theoretical origin of the jet if the linear decay law were preserved along all the extension of the jet and B is an empirical constant. Moreover the jet spreads into the ambient following a law [29] like:

$$\frac{Y_{\frac{1}{2}}}{D} = \frac{S(x - x_0)}{D} \tag{1.64}$$

Being S an empirical constant.

In table 1.2 some values for B and S in orifice jets [33] are presented.

Present work aims first of all to perform a complete study of the near and far field of a turbulent orifice jet, also with relation to the dependency on the Reynolds number of the features of the phenomenon, in order to improve

Investigators	Orifice type	B	S	Reynolds number
Quinn [33]	Contoured	0.164	0.096	1.84 x 10^5
Quinn [33]	Sharp-edged	0.167	0.098	1.84 x 10^5
Wygnanski and Fiedler [53]	Contoured	0.169	0.086	8.64 x 10^4
Rodi [38]	Contoured	0.160	0.086	8.08 x 10^4
Panchapakesan and Lumley[27]	Contoured	0.165	0.096	1.1 x 10^4
Obot et al. [26]	Square-edged	0.190	0.088	1.3 x 10^4

Table 1.2: Mean streamwise velocity decay and spreading rates on the jet centreline for orifice jets

the knowledge of this jet that is still not appropriate. To do this three different non-intrusive experimental techniques have been used, the PIV and the Stereo-PIV, which provide a two components planar information and a three components planar information on the velocity field respectively, and the Defocusing-PIV technique which provides a volumetric information on the three velocity components. The second aim is to compare these three techniques on the basis of their resulting velocity field.

Chapter 2

Experimental Setup

The experimental setup can be split in the jet apparatus and the acquisition system. The first consists of a closed loop hydraulic circuit starting from an auxiliary tank, from which a centrifugal pump transfers the water to a secondary constant level head tank to avoid artificial velocity fluctuations due to the pump, figure 2.1. The jet will be generated making use only of the potential energy owned by the water for being raised. Once flowed out of the head tank, the water enters through a honeycomb into the test tank which is subdivided by the orifice plate into a settling chamber (38 cm, upstream) and the test chamber (58 cm, downstream). Finally a second plate delimits a discharge chamber, downstream to the test one, through which the water comes back to the main tank, closing the loop. This second plate, having a larger hole compared with the orifice plate one, has the purpose of avoiding recirculation, allowing the flow to spill over through its hollow part and preventing the reversal due to the impingement on the back wall by means of its solid part.

Present study has been carried out making use of different techniques, namely PIV, Stereo-PIV and Defocusing-PIV, moving from a planar information on two components of velocity through a planar information on three components to a volumetric knowledge of three components of velocity. The quality of information on velocity components is in inverse proportion to its quantity. So the raising amount of information involves a larger uncertainty. Moreover the possibility of performing a simultaneous study of velocity and size of transparent particles, namely bubbles, joining PIV and ILIDS, a novel technique which measures the size of droplets and bubbles making use of the

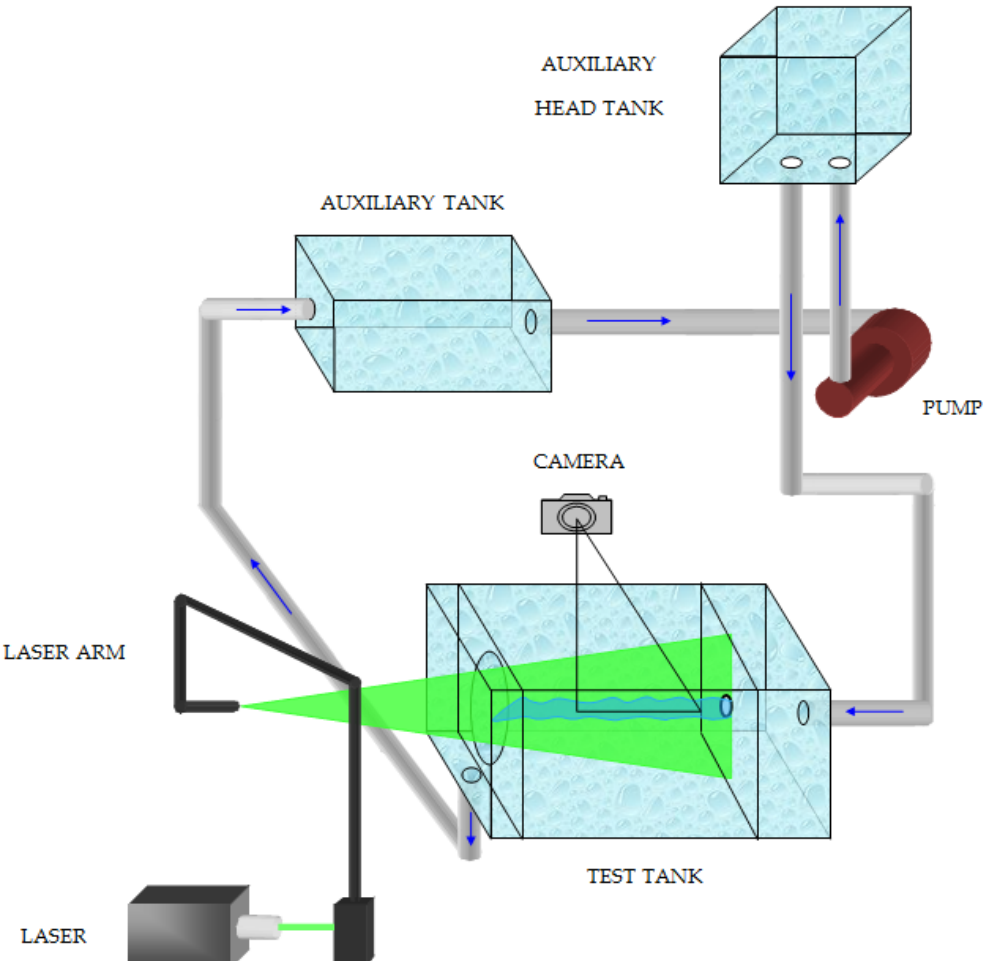

Figure 2.1: Experimental setup

interference fringe pattern of reflected and refracted rays, has been investigated. This is just a preliminary study laying the foundations for a future extension to the study of multiphase flows, namely jets containing bubbles. This part of the work is reported in the appendix (chapter 9).

The Particle Image Velocimetry is an almost well-known technique [1] which allows to obtain a spatial information on the velocity field into a plane illuminated by a coherent source of light, i. e. a laser, by means of a statistical analysis (auto or cross-correlation) on images acquired during two consecutive illuminations. In this way, groups of particles, opportunely dispersed into the fluid flow, into subareas of whole zone to be studied are identified during their movement. Thus knowing the displacement and the time interval between the two illuminations the local velocity can be evaluated. This information is the outcome of a spatial average into a finite area [34]. Making reference to figure 2.2, the relation between real particle displacement and the resulting one on the recording plane can be obtained.

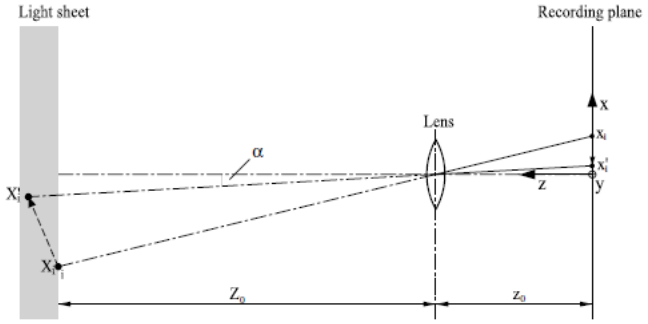

Figure 2.2: Imaging of a particle within the light sheet on the recording plane, taken from [34].

If we consider imaging of objects in air the focus criterion is given by:

$$\frac{1}{z_0} + \frac{1}{Z_0} = \frac{1}{f} \tag{2.1}$$

where z_0 is the distance between the image plane and lens, Z_0 the distance between the lens and the object plane and f is the focal length. Then the magnification factor can be defined as:

$$M = \frac{z_0}{Z_0} \tag{2.2}$$

Defining the angle α related to the imaging on the recording plane of a

particle at position x_i and x_i' and to the focal length z_0

$$tan(\alpha) = \frac{x_i'}{z_0} \tag{2.3}$$

and being $D = (D_X, D_Y, D_Z)$ the particle displacement between the two light pulses, the image displacement $\mathbf{d} = \mathbf{x_i'} - \mathbf{x_i}$ corresponding to a certain particle displacement D can be obtained:

$$x_i' - x_i = -M\left(D_X + D_Z\frac{x_i'}{z_0}\right) \tag{2.4}$$

$$y_i' - y_i = -M\left(D_Y + D_Z\frac{y_i'}{z_0}\right) \tag{2.5}$$

Assuming a particle displacement only in the X and Y directions ($D_Z \approx 0$) would simplify equation 2.4 and equation 2.5 considerably. Then, the in-plane particle displacement ($D = (D_X, D_Y)$) could easily be determined by multiplying the image displacement ($\mathbf{d} = (x_i' - x_i, y_i' - y_i)$) by (-M). In this particular case, the only uncertainty of the velocity measurement would be introduced by the uncertainty in determining the image displacement and the geometric parameters.

Present PIV setup consisted of a Quantel Twins BSL double-pulse Nd-Yag laser having 200 mJ energy per pulse and a pulse duration of 8 ns, and of a Photron Fasticam Ultima APX digital high speed camera (2000 frames/s), with 1024 x 1024 pixel resolution and a 10 bit CMOS sensor. Between them is interposed a BNC 575 pulse generator, that allows the synchronization between laser illumination and camera recording resulting in an interframe time ranging from 1/2000 to 1/125. The water was seeded by glass hollow beads having a diameter ranging from 8 to 12 μm, corresponding in present work to a Stokes number S_k, defined as the ratio between the particle response time τ and the characteristic flow time scale τ_f, quantifiable as $S_k < 0.1$, which returns an acceptable flow tracing accuracy with errors below 1 %, [47] . Laser sheet thickness was accurately set in order to be equal to approximately 1 mm. An overview on particle image velocimetry spatial resolution issue is postponed to chapter 3.

Figure 2.3 shows a reference PIV image. The particle seeding density was near to 0.05 particles per $pixel^2$ and the particle image diameter (dp) ranged was near to 3 pixels.

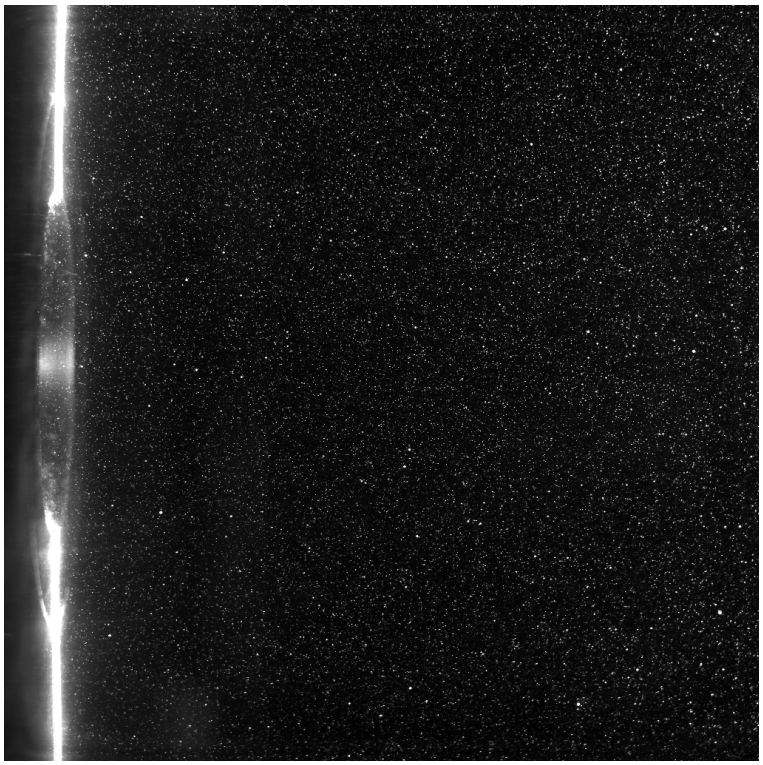

Figure 2.3: Reference PIV image

The Stereo-PIV is an evolution of the PIV which allows to evaluate the third component of velocity into a plane making use of the information coming from two simultaneous recordings from two different points of view [30]. Making reference to figure 2.4 and to the equations 2.4 and 2.5 and defining α as the angle between the Z axis and the ray from the tracer particle through the lens centre **O** to the recording plane and the angle β correspondingly in the YZ plane, the following relations can be obtained:

$$tan(\alpha) = \frac{x_i'}{z_0} \tag{2.6}$$

$$tan(\beta) = \frac{y_i'}{z_0} \tag{2.7}$$

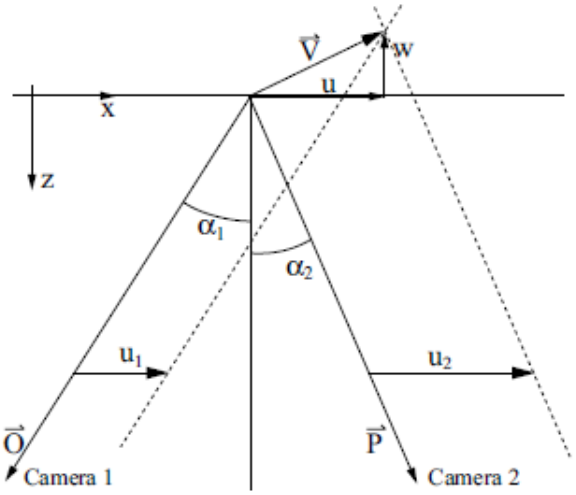

Figure 2.4: Stereo viewing geometry in the XZ plane, taken from [34]

The velocity components which are measured by the left camera are given by:

$$U_1 = -\frac{x_i' - x_i}{M\Delta t} \tag{2.8}$$

$$V_1 = -\frac{y_i' - y_i}{M\Delta t} \tag{2.9}$$

The velocity components U_2 and V_2 for the right camera can be determined similarly. Starting from these four measured values the three velocity

components *(U,V,W)* can be reconstructed. Assuming $\alpha, \beta \geq 0$ we obtain:

$$U = \frac{U_1 tan\alpha_2 + U_2 tan\alpha_1}{tan\alpha_1 + tan\alpha_2} \tag{2.10}$$

$$V = \frac{V_1 tan\beta_2 + V_2 tan\beta_1}{tan\beta_1 + tan\beta_2} \tag{2.11}$$

$$W = \frac{U_1 - U_2}{tan\alpha_1 + tan\alpha_2} \tag{2.12}$$

$$= \frac{V_1 - V_2}{tan\beta_1 + tan\beta_2} \tag{2.13}$$

The denominators of these formulae can approach zero as the viewing axes become collinear in either of their two dimensional projections. More commonly in a standard setup the cameras are approximately positioned in the same vertical position so that the angles β_1 and β_2 and their tangents $tan\beta_1$ and $tan\beta_2$ are very small. Therefore component W can be only be estimated with higher accuracy using equation 2.12, as well as V has to be rewritten using equation 2.12 which does not include $tan\beta_1$ and $tan\beta_2$ in the denominator:

$$V = \frac{V_1 + V_2}{2} + \frac{W}{2}(tan\beta_1 - tan\beta_2) \tag{2.14}$$

$$V = \frac{V_1 + V_2}{2} + \frac{U_1 - U_2}{2}\left(\frac{tan\beta_1 - tan\beta_2}{tan\alpha_1 + tan\alpha_2}\right) \tag{2.15}$$

If $tan\beta_1$ and $tan\beta_2$ are very small then the out-of-plane component W has no effect and V is given as the arithmetic mean of V_1 and V_2. Moreover note that in equations 2.10 - 2.13 there are three unknowns and four known measured values, which give rise to an overdetermined system that can be solved in a least-squares sense:

$$\begin{bmatrix} U_1 \\ V_1 \\ U_2 \\ V_2 \end{bmatrix} = \begin{bmatrix} 1 & 0 & -\frac{O_x}{O_z} \\ 0 & 1 & -\frac{O_y}{O_z} \\ 1 & 0 & -\frac{P_x}{P_z} \\ 0 & 1 & -\frac{P_y}{P_z} \end{bmatrix} \cdot \begin{bmatrix} U \\ V \\ W \end{bmatrix} \tag{2.16}$$

$$U_{meas} = A \cdot V \Rightarrow V = \left(A^T \cdot A\right)^{-1} \cdot A^T \cdot U_{meas} \tag{2.17}$$

Related to the optical access of the tank, the two cameras were placed on either side of the light sheet, as proposed by Willert in 1997 [51], figure 2.5. This configuration is a variation of one of two further existing stereoscopic configurations, the rotational one, where the two cameras are placed on the same side of the light sheet and their optical axes are rotated such that they intersect the object plane at the system axis. The other optical configuration is the translation one, where the the two cameras are placed on the same side of the light sheet and are parallel to each other, such that they are both orthogonal to the light sheet [30].

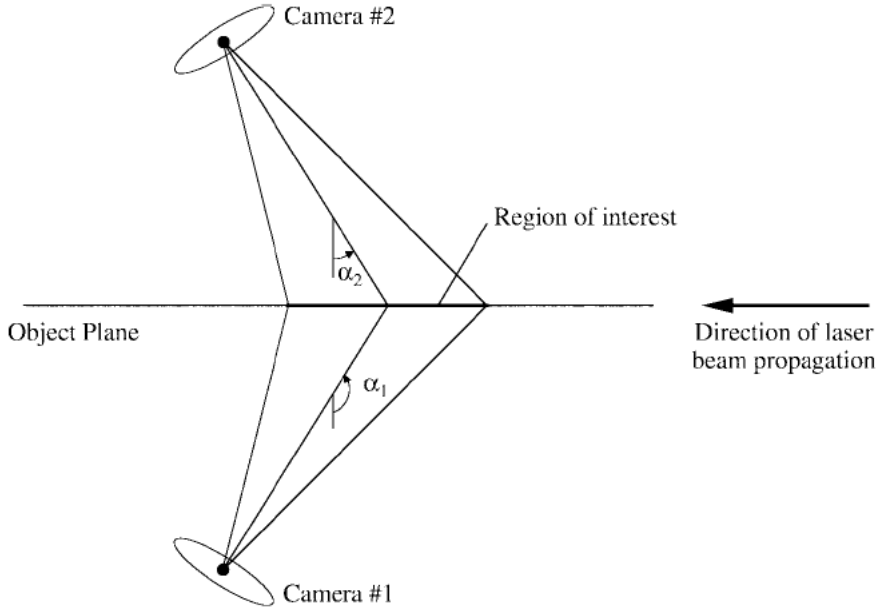

Figure 2.5: Stereoscopic arrangement with the two cameras on both sides of the light sheet (Willert 1997) [51]

This arrangement has two benefits. First of all it is possible to operate both cameras in forward scattering properly orienting the direction of propagation of the illuminating laser beam. Because scattering efficiency is higher in forward scatter, figure 2.6, both views can benefit of a higher and equal signal-to-noise ratio.

Moreover both views will be stretched identically, rather than the opposite stretching for cameras situated on the same side of the light sheet. However both views still have to be interpolated on a Cartesian grid. In order to obtain images in good focus over the entire image plane Scheimpflug

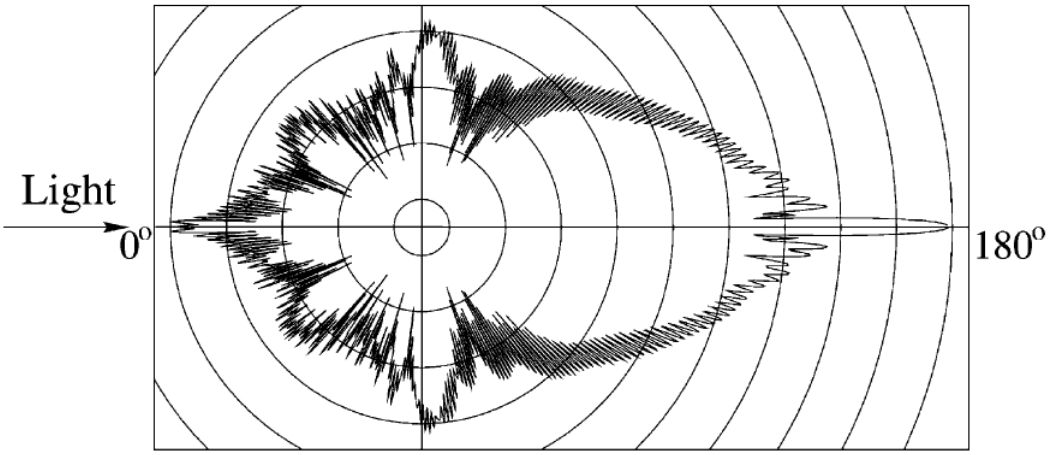

Figure 2.6: Light scattering by a 30 μm glass particle in water taken from [34]

condition has been imposed [31]. It requires that the object plane, the lens plane and the image plane are collinear as shown in figure 2.7.

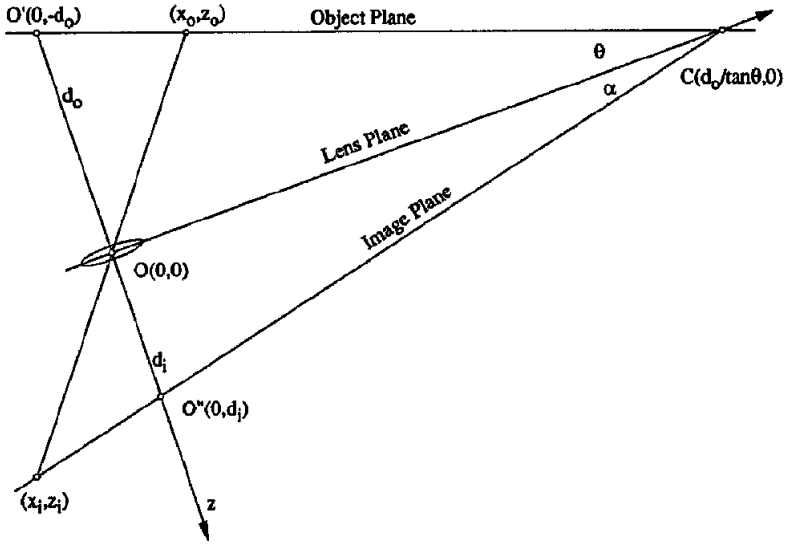

Figure 2.7: Scheimpflug condition, taken from [31]

The particles which are in the object plane (O'C) will be in sharp focus in the image plane (O"C) only when these two planes intersect in the lens plane (OC). If the centre of the lens O corresponds to the origin of the coordinate system, the following conditions can be written:

For the lens plane ,

$$z = 0, \tag{2.18}$$

For the object plane,

$$z = x\,tan\theta - d_o, \tag{2.19}$$

For the image plane,

$$z = -x\,tan\alpha + d_i, \tag{2.20}$$

where d_o and d_i are the nominal object and image distances from the lens. Any point lying in the object plane (x_o, z_o) will form an image at the point (x_i, z_i) such that

$$\frac{x_o}{z_o} = \frac{x_i}{z_i} \tag{2.21}$$

Making use of equations 2.18 - 2.21 can be shown that

$$\frac{1}{z_i} - \frac{1}{z_o} = \frac{1}{d_o} + \frac{1}{d_i}\left(= \frac{1}{f}\right), \tag{2.22}$$

where f is focal length of the lens. This is the condition that particle images will be in sharp focus in the image plane. The local magnification $-\frac{z_i}{z_o}$ varies across the image plane and equals the nominal magnification $M = \frac{d_i}{d_o}$ only for $x_o = x_i = 0$.

Moreover, in order to reduce optical distortions related to the inclined interface water/air two prisms filled with water were fixed at the wall of the test section so that the transition from air to water happens into a plane orthogonal to the two cameras, figure 2.8.

Figure 2.9 shows a reference Stereo-PIV image.

DDPIV is an extension of planar digital PIV to the third dimension [28]. The interrogation domain is a volume where 3D coordinates of fluid markers are determined prior to flow analysis. However, unlike PTV or stereo-based methods, DDPIV has one unique optical axis and is based on pattern matching rather than on stereoscopic matching of particle images. The other fundamental difference resides in the statistical evaluation of the particle displacement, which is here recovered by performing a 3D spatial correlation of particle locations. In that sense, DDPIV uses the same methodology as

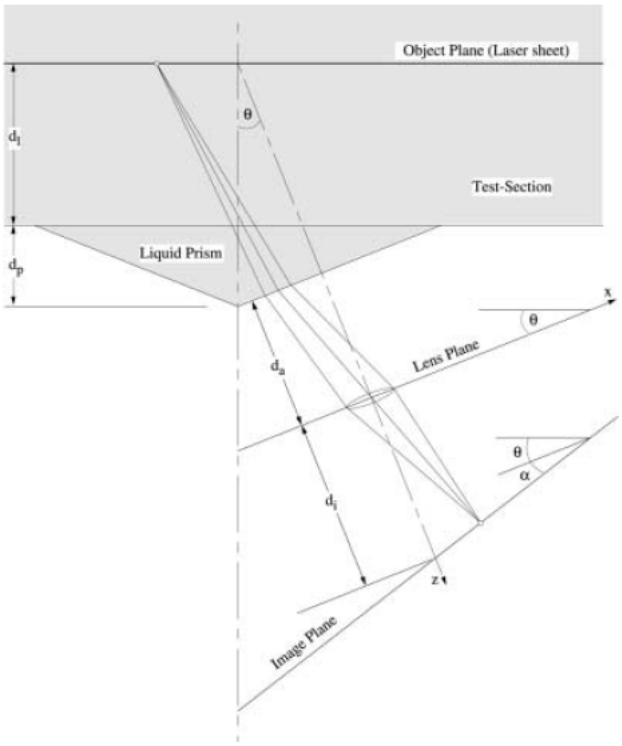

Figure 2.8: Scheimpflug stereocamera with a liquid prism, taken from [30]

Figure 2.9: Reference Stereo-PIV image

planar DPIV does in the pixel domain of the particle images. Terms such as single-frame double or multiple exposure, or multi-frame single exposure are still fully applicable, except that the DDPIV frame is here represented by a volumetric ensemble of particles. Figure 2.10 [28] helps to describe the DDPIV technique.

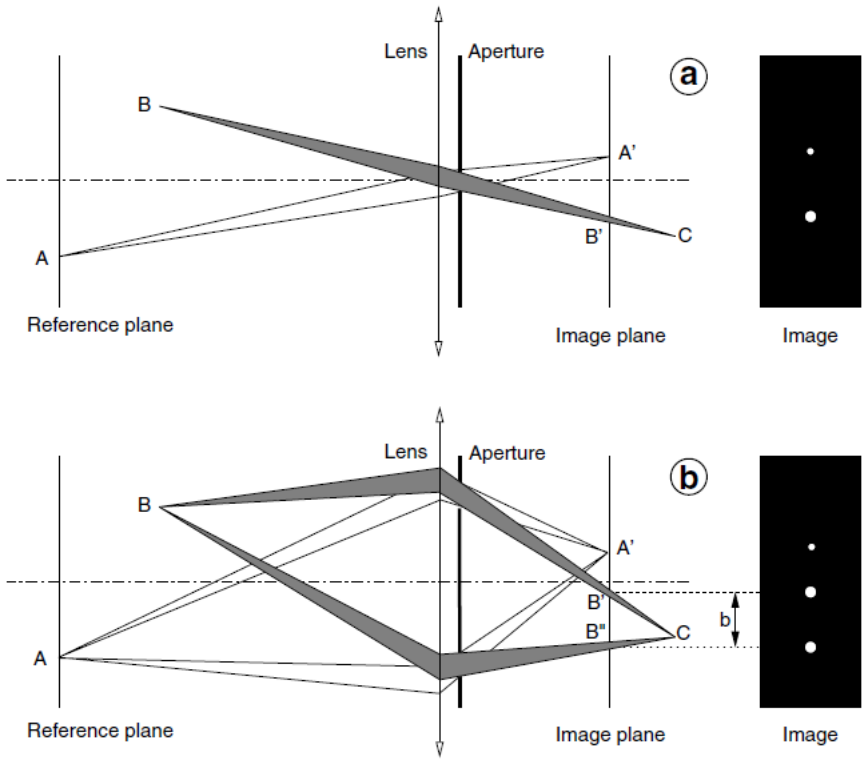

Figure 2.10: The defocusing principle: (a) standard imaging system, (b) defocusing system. Taken from [28]

Figure 2.10 (a) shows a typical two dimensional imaging system, consisting basically of a converging lens and of an aperture. The point A located on the object plane (reference plane) appears focused as A' on the image plane (sensor plane). On the other hand the point B located in between the object plane and the lens plane is projected as a blurred image B'. The DDPIV technique uses a perforated mask with two or more apertures shifted away from the optical axis to obtain multiple images from each scattering source. This can be seen in figure 2.10 (b) where B' and B" are the images of point B. The image shift b on the image plane, due to the off-axis location of these apertures, is related to the depth location of the source points.

PIV and Stereo-PIV acquired images have been analyzed by LaVision Davis 7 software making use of a multipass algorithm made of 2 passes in correspondence to a larger window size equal to 64x64 pixels and 4 passes in correspondence to a smaller window of 32x32 pixels, in both cases using a 75 % overlapping in order to improve spatial resolution and to prevent the appearance of spurious vectors. Thus the final spacing between velocity vectors was 8 pixel.

Results

Chapter 3

Spatial resolution effect

Due to the fact that an evaluation of all the terms involved in equations 1.16 - 1.19 is very challenging both experimentally and numerically due to the requirements of high temporal and spatial resolutions, a preliminary study on the effects that varying the spatial resolution has on the resulting features of the jet has been carried on. Several ways of extending spatial resolution in PIV have been already worked out. Keane et al [15] in 1995 and later Stitou et al. [43] in 2001, e.g. , used the knowledge of the velocity field from cross correlation of large sub-regions and particle tracking PTV in order to achieve an high spatial resolution, Westerweel et al. [48] in 1997 succeeded in it making use of a window offset in the analysis, whereas Scarano in 2002 [41] and in 2003 [42] developing an adaptive window shaping. Westerweel et al. [49] and later Billy et al. [4] in 2004 and Kähler [14] in 2006 applied a two-point ensemble correlation at single-pixel resolution, while finally Lavoie et al. [20] in 2007 compared PIV spatial resolution with the one of Hot-Wire-Anemometry, suggesting some spectral corrections in order to correct PIV results. However, once advanced window deformation procedures are employed, the simplest way to attain higher spatial resolution is still to consider the overlapping of several flow regions as small as possible (in terms of flow scales). Thus, the problem of spatial resolution is considered directly by decreasing the size of the acquired flow region (located right downstream to the orifice plate, so to deepen the knowledge of the near field of these jets). In detail 2D x 2D, being D orifice diameter (3 cm), 3D x 3D, 4D x 4D, 5D x 5D areas have been acquired at the same Reynolds number, i.e. 35000. Each case was studied acquiring and analyzing 10000 couples of images.

Resolution	Framed Area	Spatial Resolution $\left(\frac{pixel}{cm}\right)$	Spatial Resolution $\left(\frac{vector\ spacing}{Taylor\ microscale}\right)$
1	2Dx2D	~ 170	0.2232
2	3Dx3D	~ 110	0.3348
3	4Dx4D	~ 85	0.4464
4	5Dx5D	~ 65	0.5580

Table 3.1: Parameters of spatial resolution effect study

In table 3.1 the different experimental conditions are summarized. It is interesting to note that for the first two resolutions the image size is between 25 and 40 Taylor microscales, whereas for the other two is larger than 50.

The fourth column, reporting the ratio between vector spacing and Taylor microscale, offers a hint for an observation concerning Nyquist-Shannon sampling theorem. In fact the different spatial resolutions sampling ability of the inertial range (Taylor microscale λ) gets worse moving from Resolution 1 to Resolution 4 reaching the limit value of half of the Taylor microscale each vector spacing (sampling rate) [25].

3.1 Statistical moments

In order to get a better knowledge of the near field of this jet, in figure 3.1 the longitudinal mean velocity radial profiles have been plotted in correspondence to different downstream positions (0.1 D, 1 D, 2 D, 3 D, 4 D). First of all the distinctive shape of the mean velocity exit profile of an orifice jet, with the two velocity peaks near the edges of the orifice [23], can be clearly seen. This is different from the top hat profile of a nozzle jet and the power law profile $\left(\frac{1}{7}\right)$ of a pipe jet [23]. Then the interaction between jet and surrounding fluid starts and velocity tends to be distributed in the space and its profile to enlarge over and over.

The effect of spatial resolution can be better pointed out by the transversal profiles of the statistical moments and of the Reynolds stress tensor as the framed area varies, as presented in figures 3.2 to 3.8.

Figures 3.2 and 3.3 show the transversal profiles of axial mean velocity respectively at 0.1 D and 2 D downstream to the orifice. In figure 3.2, it can be noticed the slight difference between the results of the higher resolution

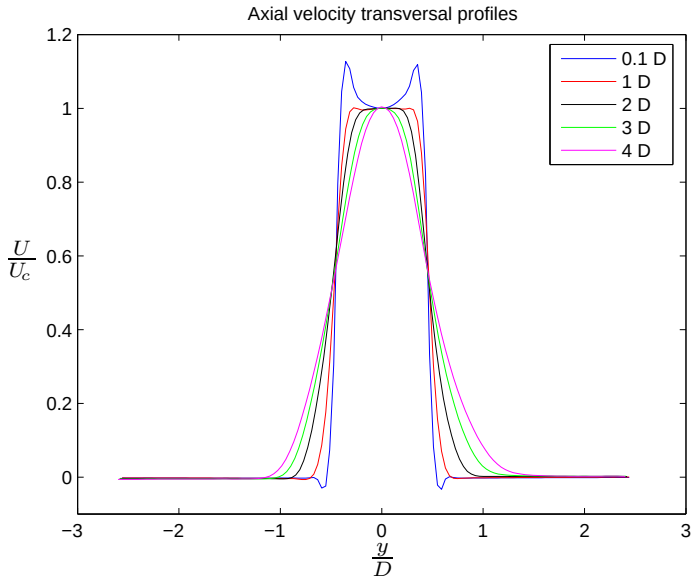

Figure 3.1: Axial velocity transversal profiles in correspondence to different positions downstream to the orifice

setups (Resolution 1 and 2, table 3.1) and the lower resolution setups (Resolution 3 and 4). Data coming from the resolution 3 and resolution 4 setups are averaged onto a large framed area between the moving fluid inside the jet and the quite still ambient fluid. On the other hand, at the downstream profile presented in figure 3.3, the effect of spatial resolution becomes less evident.

In the same figure 3.2 a comparison between the very near field axial velocity transversal profiles of the present work and the one by Mi et al. [23], which is the outcome of a Hot Wire Anemometry (HWA) measurement on an orifice jet at Re=16000, is shown. Mi data, which are characterized by the higher spatial resolution of HWA $\sim 10^{-5}$ m, lie near to the ones among present results which have higher resolution (Resolution 1 and 2). Thus can be ensured the goodness of a proper PIV study compared to HWA measurements, preserving the advantage of non-intrusivity.

The vena contracta phenomenon can also be observed in figure 3.4 that represents the radial velocity transversal profile in the very near zone (0.05 D downstream to the orifice). In contrast with the results from all the other turbulent jets, the radial velocity preserves a univocal sign along each of the two sides of the jet which are determined by the axis in the centre of jet. This means that the jet does not spread outwards, as the other jets, but

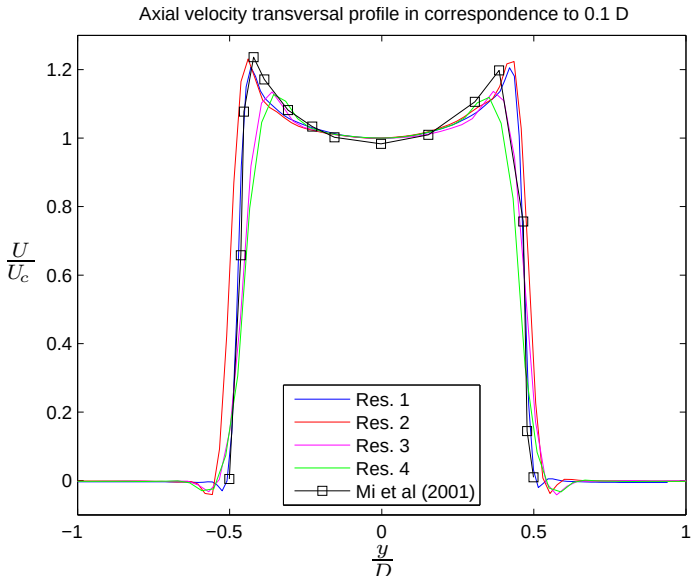

Figure 3.2: Axial velocity transversal profile 0.1 D downstream to the orifice

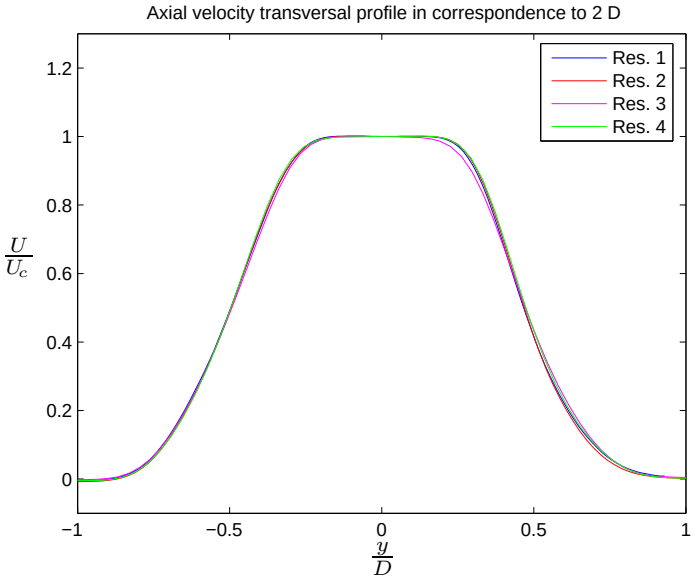

Figure 3.3: Axial velocity transversal profile 2 D downstream to the orifice

rather reduces its section due to the contraction that persists downstream to the orifice plate because of the sudden transit through the small hole.

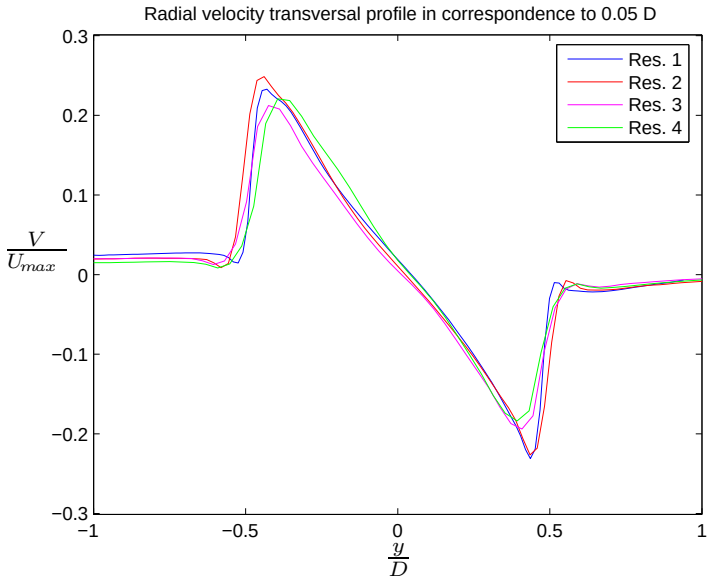

Figure 3.4: Radial velocity transversal profile 0.05 D downstream to the orifice

Also in RMS radial profiles a relevant effect of spatial resolution is observed close to the orifice. Figures 3.5 - 3.6 display the transversal profile of the root mean square of the axial component of velocity, in correspondence to a distance 0.1 D and 2 D downstream to the orifice. As for the mean velocity field, in figure 3.5 the distinctive shape of the RMS exit profile, which is low at the centre of the jet and high, with two sharp peaks, in correspondence to the edges of the orifice is noticed [23], [33]. Due to the different spatial resolution, these peaks appear highly sharp for the higher resolution data (Resolution 1) and then more and more smoothed as the spatial resolution decreases. The effect is less evident in the results in the radial profiles at a distance x=2D from the orifice, as presented in figure 3.6. The results in correspondence to 0.1 D are compared with the ones of Quinn (2005) [33], obtained by a HWA study. Again present results seem to split into two groups, one made of the higher resolution ones (Resolution 1 and 2), which remains near to the HWA result and the one made of lower resolution results (Resolution 3 and 4) which are quite different.

For higher order statistical moments, the effect of spatial resolution is felt also farther from the orifice. In figures 3.7 and 3.8, radial profiles of

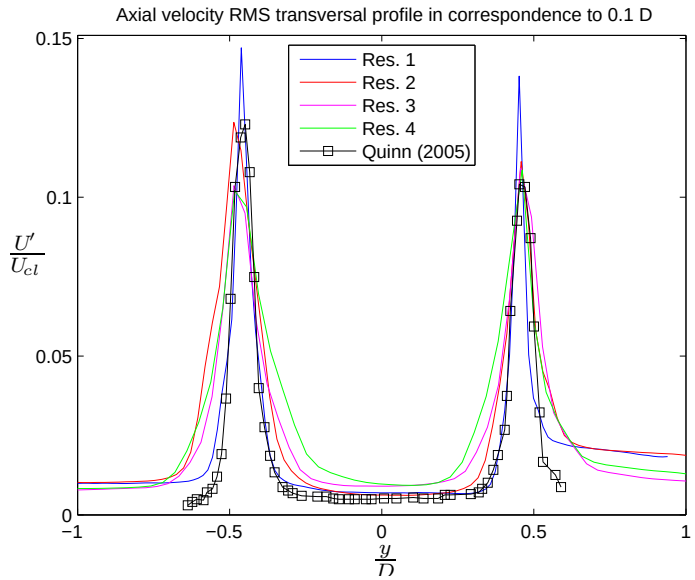

Figure 3.5: Axial velocity RMS transversal profile 0.1 D downstream to the orifice

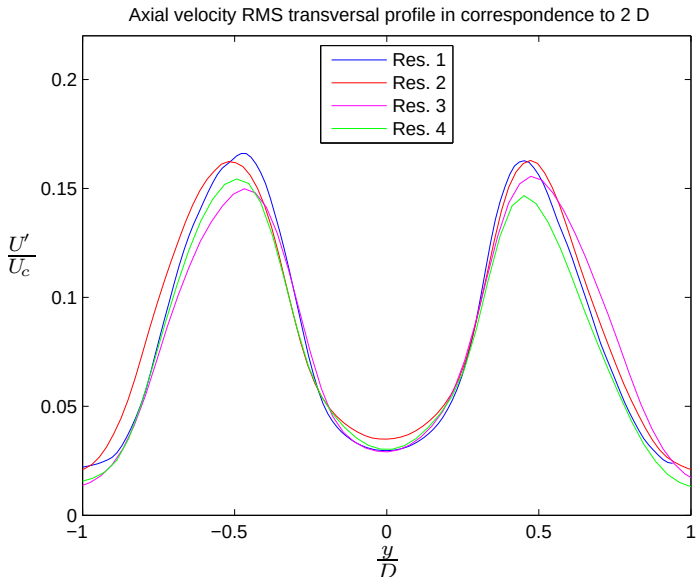

Figure 3.6: Axial velocity RMS transversal profile 2 D downstream to the orifice

skewness and flatness factors are presented at a distance x=2D from the orifice. This is the first time that higher order statistics of an orifice jet have been investigated. The larger framed areas generate a result slightly different from the one resulting from the smaller areas, especially near the centre of the jet. The larger is this zone the larger is the area on which each PIV resulting vector is averaged.

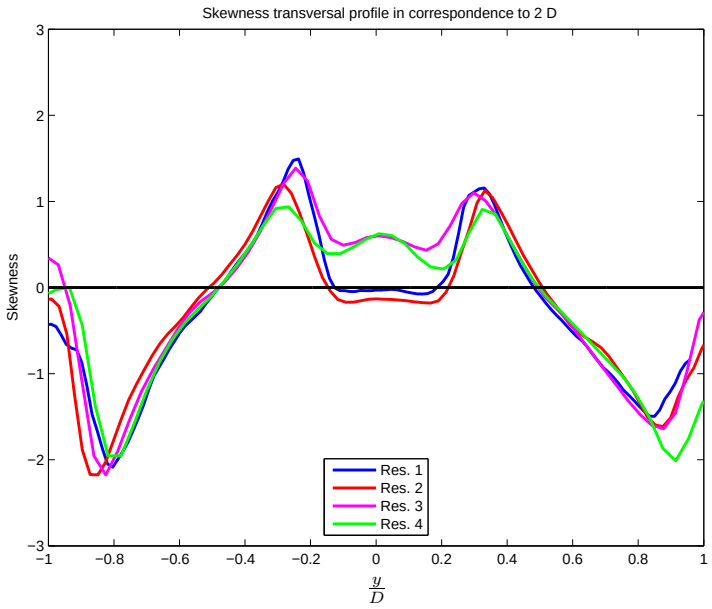

Figure 3.7: Axial velocity Skewness transversal profile 2 D downstream to the orifice

3.2 Large scale and small scale route to isotropy

In order to study the occurrence of large scale isotropy, a characteristic parameter can be evaluated. It is the ratio of streamwise to vertical *rms* velocities, i.e. $\frac{u'}{v'}$ [5],[7]. It is an indicator of the energy supplied to the large scales, due to the fact that the second order structure functions $\left\langle (\delta u')^2 \right\rangle (x,r) = \overline{(u'(x+r)-u'(x))^2}$ and $\left\langle (\delta v')^2 \right\rangle (y,r) = \overline{(v'(y+r)-v'(y))^2}$ tend to $2u'^2$ and $2v'^2$ when $r \to \infty$ [39]. If the phenomenon were isotropic at large scales this parameter should be equal to 1, being equivalent the transversal and the axial directions. Figure 3.9 shows the results of its evaluation.

For $\frac{x}{D} < 5$ the flow field is observed to be not fully isotropic in cor-

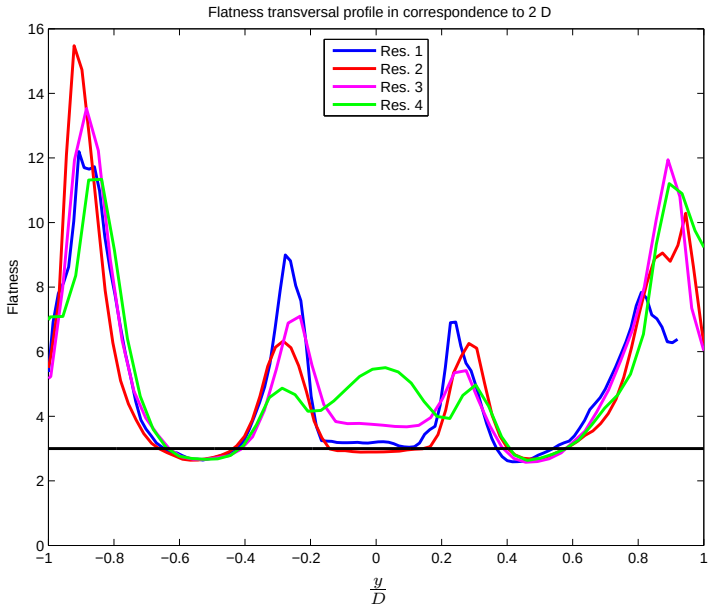

Figure 3.8: Axial velocity Flatness transversal profile 2 D downstream to the orifice

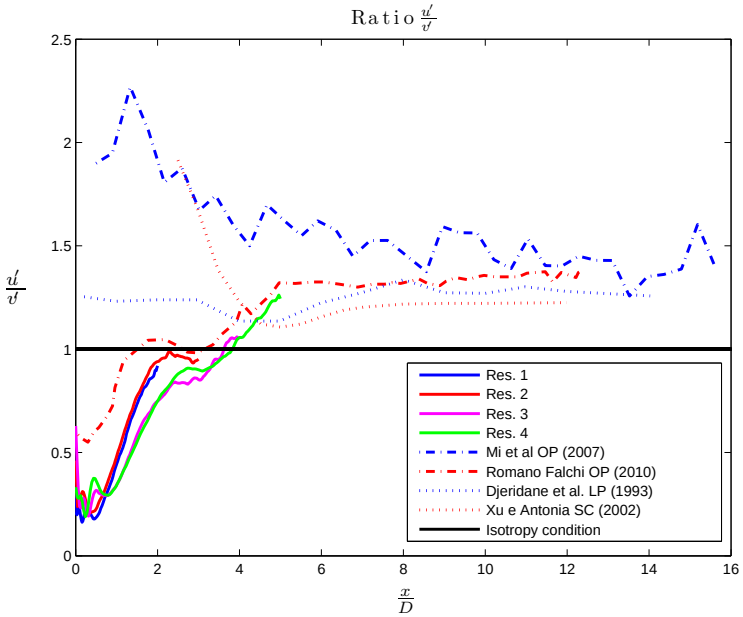

Figure 3.9: Axial evolution of large scale isotropy parameter $\frac{u'}{v'}$

respondence to large scales. Indeed the parameter tends towards a value near to 1.3 moving along jet axis. This fact is confirmed by the existing works on orifice jets (OP) [22] and [40], both made with the PIV technique and having a pixel resolution of 100 $\frac{pixel}{cm}$ and 95 $\frac{pixel}{cm}$ respectively, and also on long pipe jets (LP) [7], made with Laser Doppler velocimetry technique, having a reference spatial resolution of $\sim 10^{-4}$ m, and smooth contraction jets (SC) [54], made with Hot Wire Anemometry having a spatial resolution of $\sim 10^{-5}$ m. No substantial influence seems to be related to the different spatial resolutions. Therefore, the large scales, which mainly affect the results of $\frac{u'}{v'}$, have only a slight dependence on spatial resolutions, as also observed from the analysis of low order statistical moments.

With regard to the small scale isotropy, the isotropy parameters computable from the data available through a PIV study have been measured, namely K_1, K_3, K_4, K_9, and the results are shown in figures 3.10 - 3.13 compared with the ones of Romano and Falchi [40] on the same jet in correspondence to a Re=20000 and having a pixel resolution of 95 $\frac{pixel}{cm}$. Spatial derivatives have been approximated by finite differences, namely using a second order accurate central difference form on interior points and a first order accurate forward difference form on left and right edges.

The parameter $K_1 = \frac{\left\langle \left(\frac{\partial v}{\partial y}\right)^2 \right\rangle}{\left\langle \left(\frac{\partial u}{\partial x}\right)^2 \right\rangle}$ compares the spatial evolution of longitudinal and transversal velocities along their own direction. In an isotropic phenomenon all the directions are equivalent and therefore this ratio should be equal to 1, as given in equation 1.56. The results, shown in figure 3.10, confirm this hypothesis, already in the near zone $\left(\frac{x}{D} < 5\right)$, in correspondence to all resolutions. In the very near zone spatial gradients are more intense and therefore the effects of spatial resolution are more pronounced there and tend to diminish moving downstream as the spatial gradients are smeared out by viscosity.

The parameter $K_3 = \frac{\left\langle \left(\frac{\partial u}{\partial y}\right)^2 \right\rangle}{\left\langle \left(\frac{\partial u}{\partial x}\right)^2 \right\rangle}$ estimates the relative importance, with regard to the longitudinal velocity component, of the transversal evolution with respect to the axial one. If the isotropy conditions were fulfilled this parameter should be equal to 2 , as given in equation 1.56. From figure 3.11 this condition doesn't seem to be fulfilled in the near zone in agreement with Romano and Falchi results. Again the spatial resolution affects the

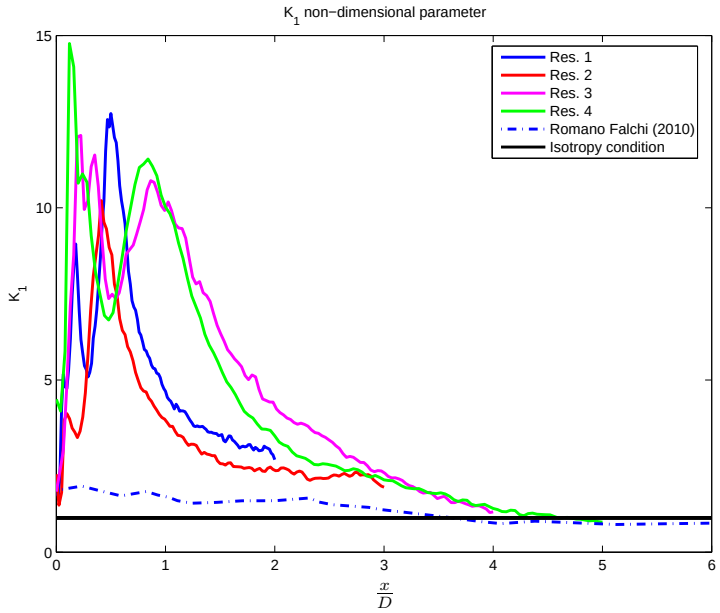

Figure 3.10: Axial evolution of small scale isotropy parameter K_1

very near zone and less all the rest of the jet.

$K_4 = \frac{\left\langle \left(\frac{\partial v}{\partial x}\right)^2 \right\rangle}{\left\langle \left(\frac{\partial u}{\partial x}\right)^2 \right\rangle}$ is corresponding and opposite to K_3 in regard to axial evolution of transversal velocity; the isotropic value is equal to 2 and again this condition doesn't seem to tend to be satisfied (figure 3.12) in the studied zone in conformity with Romano and Falchi results. Once more the effect of a different spatial resolution is noticeable in the very near zone and to a lesser degree moving downstream along the axis of the jet.

The last studied parameter was $K_9 = \frac{\left\langle \frac{\partial u}{\partial y}\frac{\partial v}{\partial x} \right\rangle}{\left\langle \left(\frac{\partial u}{\partial x}\right)^2 \right\rangle}$. It depends on the cross derivatives of axial and transversal velocities. The isotropy condition prescribes that its value should be equal to -0.5 and again doesn't seem to be satisfied, irrespective of the framed area, figure 3.13, showing however a splitting of the results between high resolution and low resolution ones.

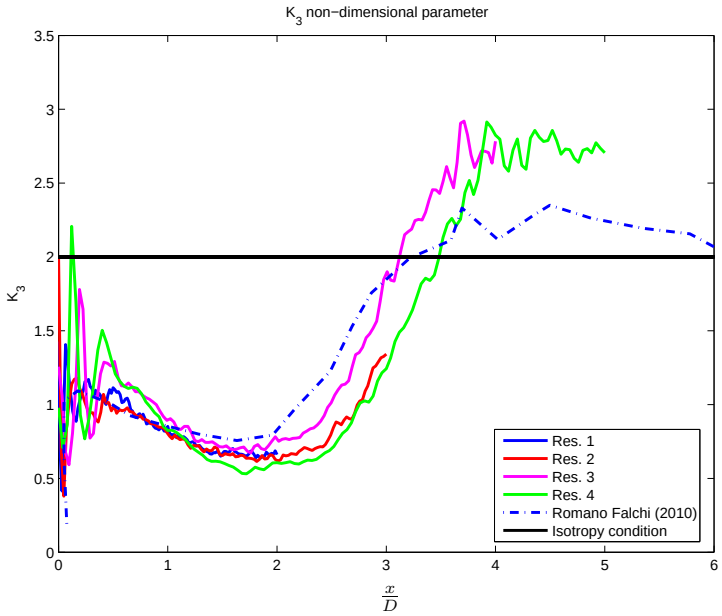

Figure 3.11: Axial evolution of small scale isotropy parameter K_3

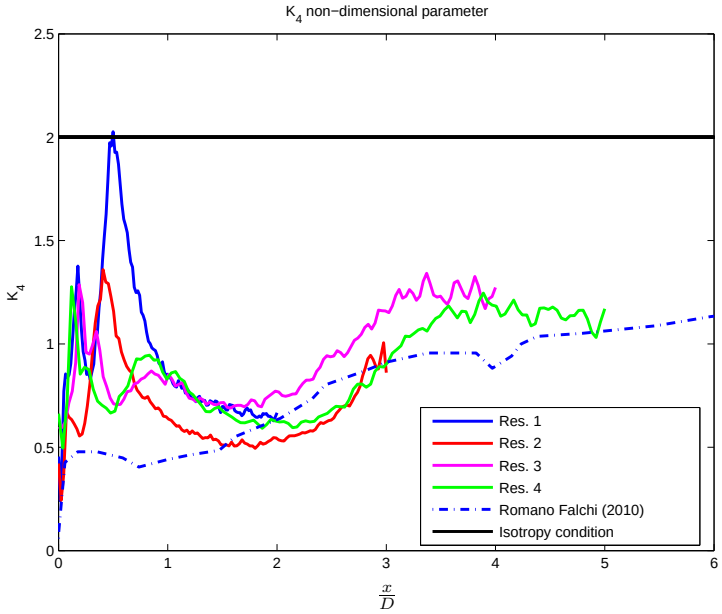

Figure 3.12: Axial evolution of small scale isotropy parameter K_4

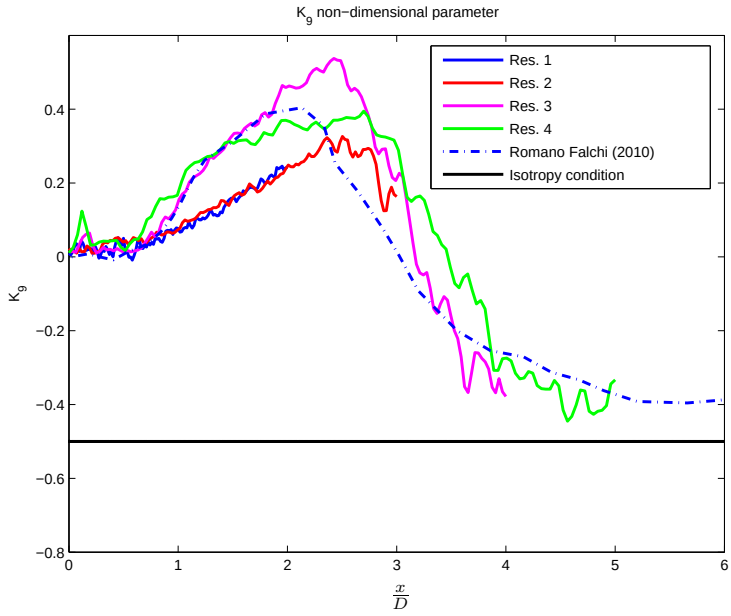

Figure 3.13: Axial evolution of small scale isotropy parameter K_9

Chapter 4

PIV Study

This chapter presents the results obtained by the use of the PIV technique. This part of the work aimed to deeply understand the orifice jet phenomenon and to investigate the influence of the Reynolds number on the far field and near field features of the jet, i.e. the position of the vena contracta and the ratio $\frac{U_e}{U_{max}}$, the fulfillment of self-similarity condition for all the quantities, the spreading rate of the jet and jet's half-width, etc... Therefore a wide zone, nearly 20 D long, along the axis of the jet has been investigated varying the Reynolds number, namely setting its value to 70000, 35000, 15000, 8000, 4000 and 2000. The whole zone has been divided into six subzones, each one equal to 4 orifice diameters $\left(95\ \frac{pixel}{cm}\right)$. In correspondence to each zone 10000 images (5000 couples) have been acquired in subsets of 1000 at a repetition rate of 8 Hz, so that each acquisition took 125 s e.g.. Being the integral length scale near to $3x10^{-2}$ m, the integral time scale can be evaluated making reference to the local mean velocity, ranging from 3.5 $\frac{m}{s}$ to 0.1 $\frac{m}{s}$, to be equal to a value moving from $\sim$ 6 ms to $\sim$ 0.3 s. Due to the fact that, in the processing of random signals, samples are statistically independent if they are separated by a period of the least 2 times the integral time scales [10] and being the time distance between each couple of images equal to 0.125 s, the statistical independence between all samples can be stated for the higher Reynolds numbers (70000-8000) and between most of samples for the other ones (4000 and 2000).

In order to evaluate the effectiveness of the number of images, tests on statistical convergence have been performed. In figure 4.1 is represented the difference between the value of the velocity averaged on an increasing amount

of samples (instantaneous fields) and the value of the velocity averaged on the total amount of samples (in present case 5000) in correspondence to a position at the center of the jet. Figure 4.2 represents a similar difference in correspondence to the RMS of the axial velocity at the center of the jet is represented.

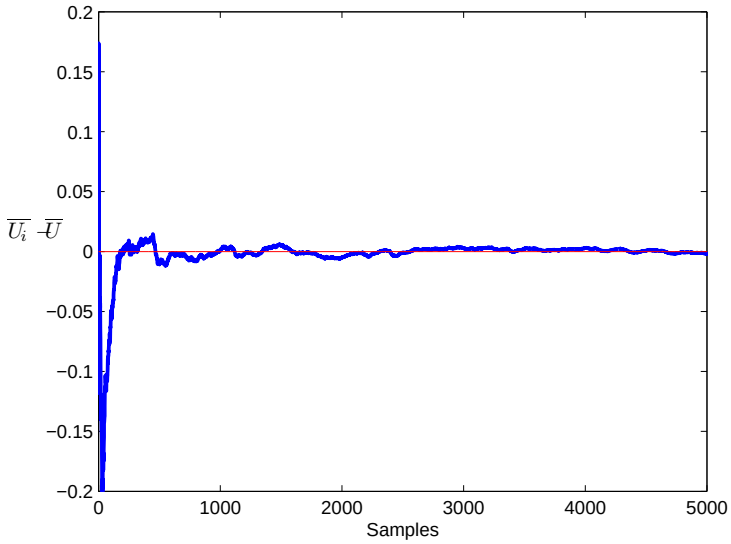

Figure 4.1: Convergence of the mean axial velocity evaluated with different sample number in correspondence to the jet centreline

In both cases, starting from an amount of 2500 samples the convergence of the results can be stated.

4.1 Statistical moments

First of all, in order to have an overview on the phenomenon, the overall plots of U_{mean} and of the Reynolds stress in correspondence to an intermediate Reynolds number (Re=15000) are presented. They were obtained simply adjoining the results obtained in correspondence to the different zones and aligning them vertically due to small misalignments.

In figure 4.3 (a) first of all the vena contracta phenomenon can be observed. The mean axial velocity reaches its maximum nearly 1 D downstream to the orifice plate. All those jet features developing from $\frac{x}{D} = 0$ in a contraction or pipe jet are now displayed starting from $\frac{x}{D} = 1$ due to

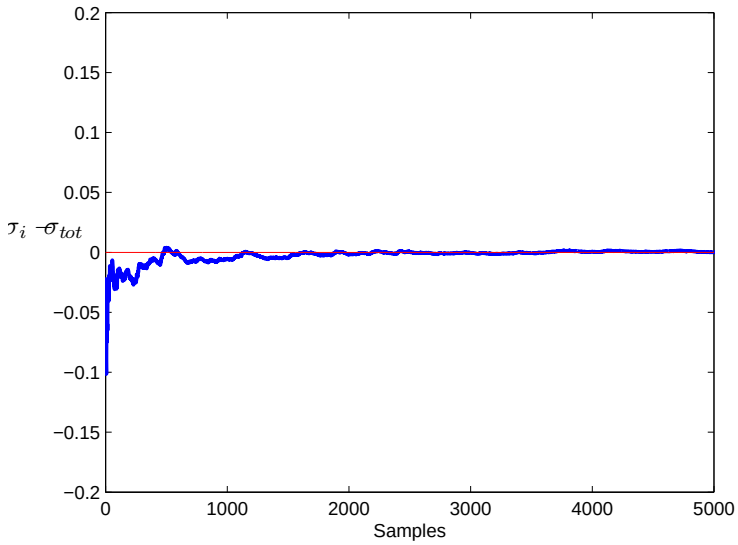

Figure 4.2: Convergence of the RMS of the axial velocity evaluated with different sample number in correspondence to the jet centreline

the vena contracta phenomenon. The Reynolds stress plot instead is someway a standard one with the two interaction zones between the jet and the surrounding fluid where the turbulence intensities are the strongest.

The first result to be plotted is the longitudinal behaviour of the mean axial velocity at different Reynolds numbers in correspondence to the centre of the jet, figure 4.4, normalized by its maximum value, which occurs in correspondence to the *vena contracta*.

The results are compared with the ones present in literature and coming from the papers of Quinn (1989) [32] ($Re \approx 200000$), based on the hot wire anemometry technique, of Mi et al. (2001) (Re=16000) [23], based as well on the HWA and finally on the paper of Mi et al. (2007) [22], based on the PIV technique (Re=72000). Except for the lower Reynolds number (Re=2000), whose momentum gets quickly lost in the still fluid and therefore has a different behavior, the Reynolds number doesn't seem to have a substantial effect on this feature of the jet, most of all in the far field $\left(\frac{x}{D} \geq 10\right)$. In order to better investigate this feature a new figure has been created, figure 4.5, which is a blow up of the previous image in correspondence to the far field $\left(\frac{x}{D} = 10 - 20\right)$.

Can be clearly seen how all the different trends of the axial velocity approach a common linear decay law, which can be expressed e.g. as:

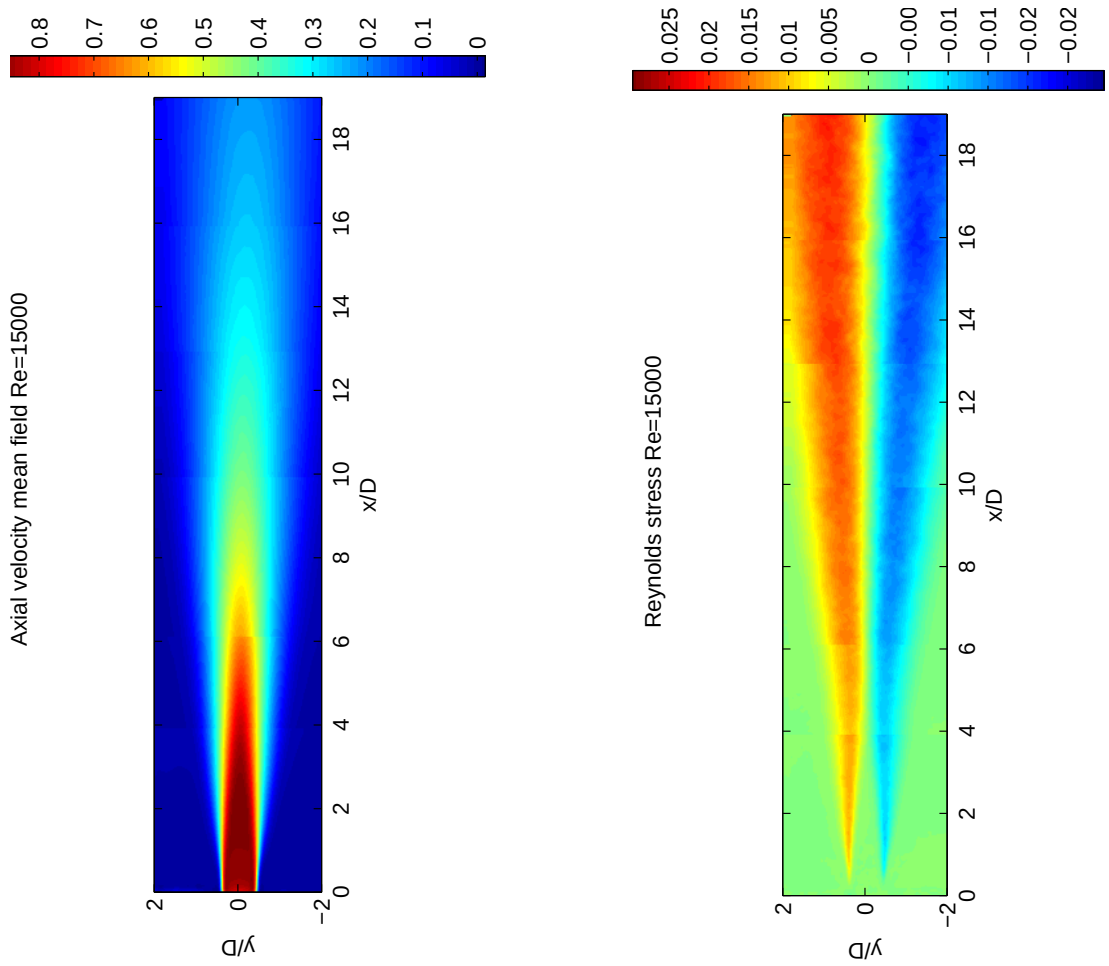

(a) *Mean field.* (b) *Reynolds stress.*

Figure 4.3: Whole field of the mean axial velocity and of the Reynolds stress

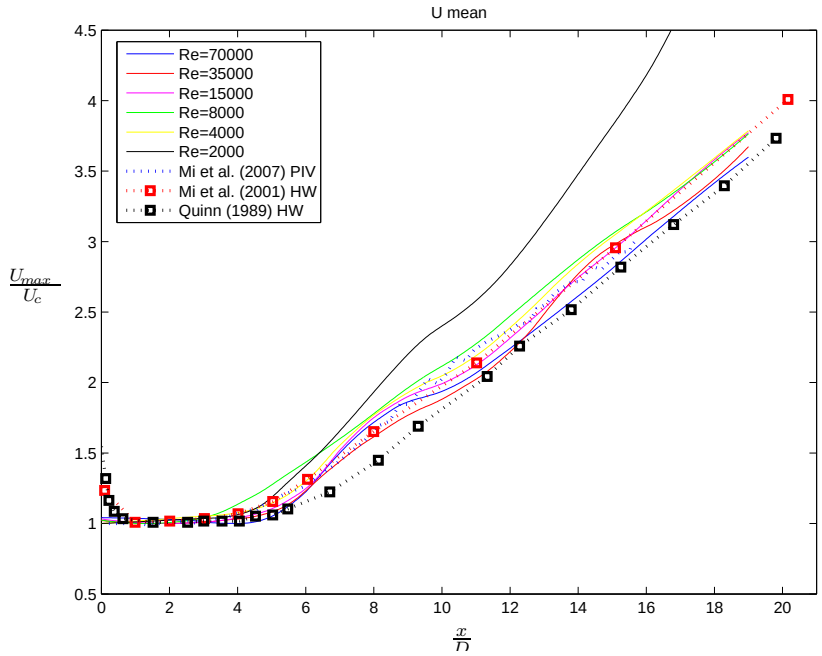

Figure 4.4: Longitudinal profile of the axial velocity in correspondence to the centre of the jet

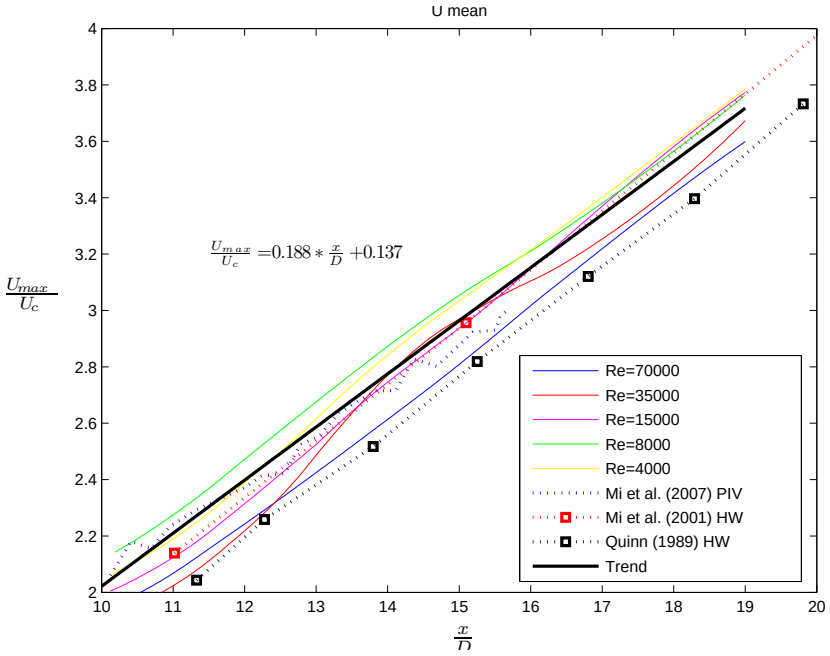

Figure 4.5: Magnification of the longitudinal profile of the axial velocity in correspondence to the centre of the jet

$$\frac{U_{max}(x)}{U_c} = 0.188 * \frac{x}{D} + 0.137 \tag{4.1}$$

The only evaluated linear regression fit present in literature are the ones of Quinn [32] and [33], respectively equal to $\frac{U_{max}(x)}{U_c} = 0.202 * \frac{x}{D} - 0.3525$ and $\frac{U_{max}(x)}{U_c} = 0.167 * \frac{x}{D} - 0.359$. Moreover the moderate influence of the Reynolds number can be better appreciated.

Another interesting physical quantity of turbulent jets is the so called jet half-width. It is basically the distance from the longitudinal axis in correspondence to which the velocity is equal to one half of that at the centerline. It is an indicator of how much the jet spreads into the still ambient fluid and therefore also of the mixing efficiency of such a jet. Figure 4.6 shows the behavior of such a quantity moving along the longitudinal axis of the jet and at different Reynolds numbers.

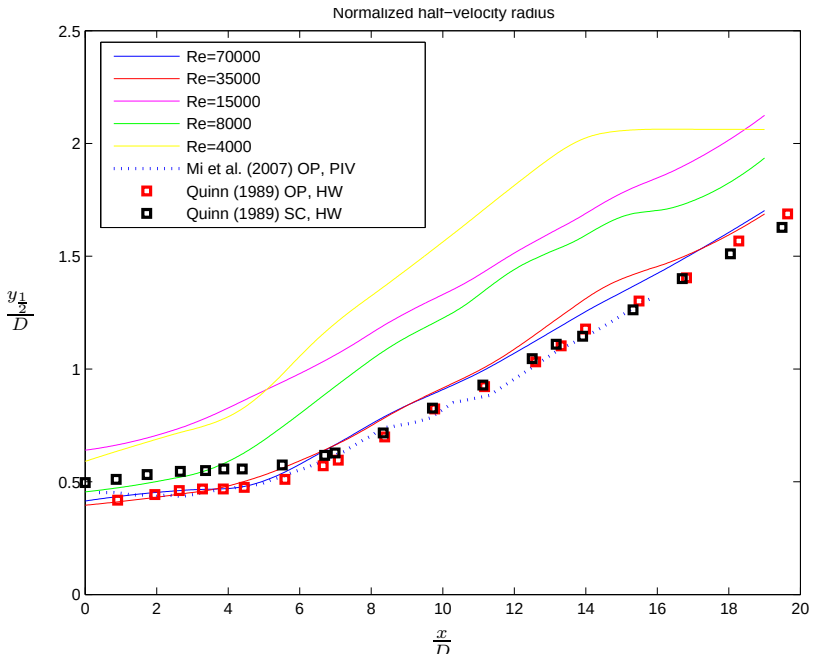

Figure 4.6: Longitudinal behavior of jet half width in correspondence to the centre of the jet

The results are compared with the ones of Mi et al (2007) [22] and Quinn (1989) [32], in this case for both the smooth contraction (SC) and orifice plate (OP) jets, and seem to split into three groups. The first made of the higher Reynolds number results (Re=70000 and 35000) and the literature

results, which are related to high Re too (respectively 72000 and ≈ 200000), the second made of the ones corresponding to intermediate Reynolds numbers (Re=15000 and Re=8000) and the one made of the lower Reynolds number (Re=4000). The results coming from setting Re=2000 are neglected because really different from the others due to its too low momentum. Blowing up into the far field further considerations can be made, figure 4.7.

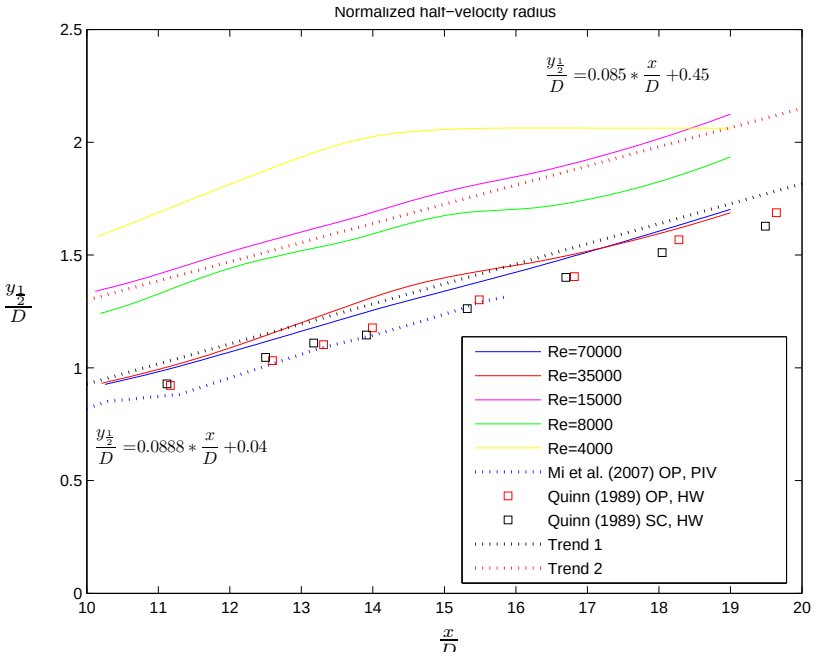

Figure 4.7: Magnification of the longitudinal behavior of jet half width in correspondence to the centre of the jet

First of all it is evident how the low Reynolds number jet lose quickly their spreading skill, e.g. near $\frac{x}{D} = 15$. Then the other two groups show in the far field a quite similar spreading rate, with the higher Reynolds number jets which seem slightly more able to penetrate into the still fluid, distinct only by the y-intercept of the spreading law.

Trying to better understand the vena contracta phenomenon and its dependence on the Reynolds number, a blow up on the very near field has been made. First of all it can be stated that the vena contracta seems to be a feature only of high speed orifice jets. In fact in correspondence to the two lower Reynolds jets, the axial velocity does not increase and then decrease but rather decays starting from the origin of the jet. Moreover the Reynolds number affects the exact location and extension of the vena contracta, which

is the position where the jet reaches its maximum velocity. Actually this site moves further downstream as the velocity of the jet increases moving from nearly $\frac{x}{D} = 1 - 1.5$ in correspondence to Re=8000 as far as $\frac{x}{D} = 4$ at Re=70000. That notwithstanding, the spatial acceleration encountered by the jet fluid becomes higher in absolute terms as the Reynolds number increases.

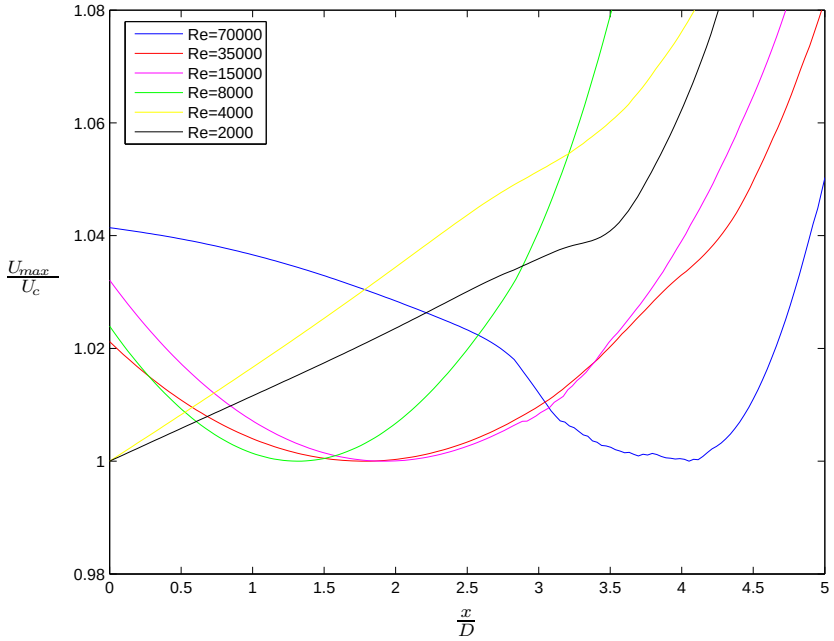

Figure 4.8: Location of the vena contracta

Another peculiar feature of turbulent jets is their tendency to reach self-similarity conditions in the far field. With regard to the mean velocity, the radial profiles, plotted with respect to to the coordinate y made non-dimensional by the so called jet's half-width $y_{\frac{1}{2}}$ (figure 4.9), show a fulfillment of the self-similarity condition for the higher Reynolds number already in correspondence to $\frac{x}{D} = 8$ and in correspondence to $\frac{x}{D} = 16$ for the lower ones, except Re=2000 whose particular behavior has been already enlightened and accounted for. This is in accordance with the findings of Mi et al. (2007) [22] (Re=72000), who stated that the self-similar mean velocity field was well developed at $\frac{x}{D} \geq 8$.

Moving to the turbulence intensities, namely the ratio between the RMS of the turbulent velocity fluctuations and the mean velocity, first of all the evolution of the this quantity moving along the axis of the jet from $\frac{x}{D} = 1$

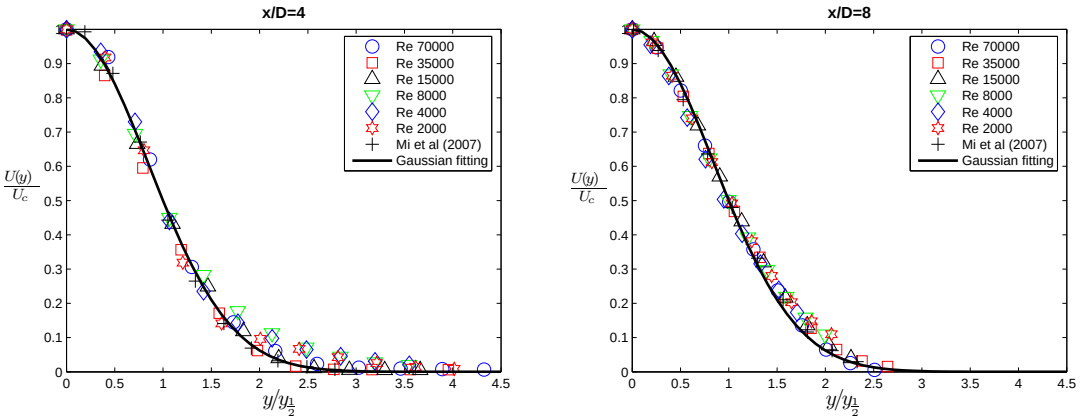

(a) $\frac{x}{D} = 4$.

(b) $\frac{x}{D} = 8$.

(c) $\frac{x}{D} = 12$.

(d) $\frac{x}{D} = 16$.

Figure 4.9: Radial profiles of the mean axial velocity

to $\frac{x}{D} = 16$ can be studied. The RMS of the axial velocity fluctuations was non-dimensionalized by the centerline exit mean velocity U_0 and the results in correspondence to Re=70000 are shown in figure 4.10. An increase of this quantity moving along the axis until $\frac{x}{D} = 4$, which is the approximate location of the vena contracta, and then a decrease can be stated, while the location of the peak values move toward the jet centreline with increasing streamwise distance from the orifice plate [32], except for the very near zone $\frac{x}{D} = 1 - 4$ which is influenced by the contraction and then widening of the flow due to the vena contracta.

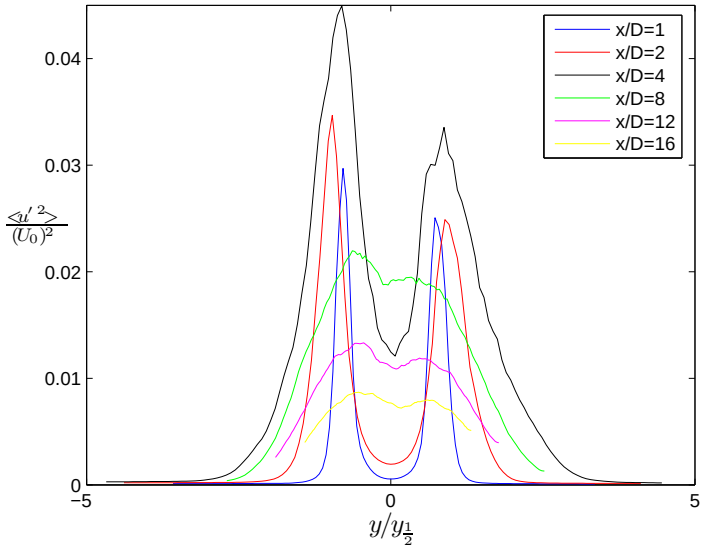

Figure 4.10: Radial profiles of the axial turbulence intensity along the axis of the jet

Trying to evaluate the attainment of self-similarity conditions, a comparison can be made with the results present in literature, namely the ones of Mi et al. (2007) [22]. They were limited to $\frac{x}{D} = 16$, and on the basis of them the authors could state that the self-similarity was far from being attained. Present work was able to extend the studied area up to $\frac{x}{D} = 19$. Figure 4.11 shows a comparison between Mi data (Re=72000) and the present ones which were the most similar to thosee experimental conditions (Re=70000). Can be seen how in the farthest studied regions the self-similarity condition is close to be attained.

Plotting the same profiles at different Reynolds number, figure 4.12, can be seen that in the furthest zones $\left(\frac{x}{D} = 18 - 19\right)$ the self-similarity condition

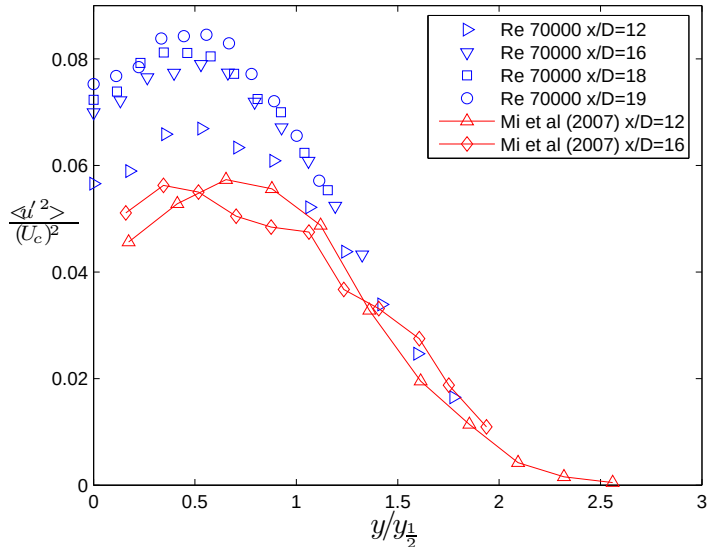

Figure 4.11: Radial profiles of the axial turbulence intensity in the far zone

of turbulence intensities is near to be attained. The results in correspondence to Re=2000 have been removed because too different from the rest due to the above mentioned reasons.

On the base of the turbulence intensities, one component of the Reynolds shear stress tensor can be evaluated, namely $\langle u'v' \rangle$, normalized by the U_c. Figure 4.13, shows as usual the radial profiles of this quantity at different downstream locations in correspondence to Re=70000. Again an increase of this quantity moving downstream to the orifice can be stated combined with the simultaneous shift of the location of the peak values toward jet centreline.

Studying the fulfillment of the self-similarity conditions of the Reynolds stress, the results can be compared with the ones obtained by Mi et al. (2007) [22] which attested that in correspondence to $\frac{x}{D} = 16$ the radial profiles of the Reynolds stress were far from being self-similar. Present study was able to move a little bit further (until $\frac{x}{D} = 19$) and discover a quite complete fulfillment of this condition in correspondence to a similar Reynolds number (Re=70000), figure 4.14.

Extending the study to the other Reynolds numbers (figure 4.15), the same statement can be extended to all the cases, except for Re=4000, in correspondence to which there is still a distance from the attainment of the

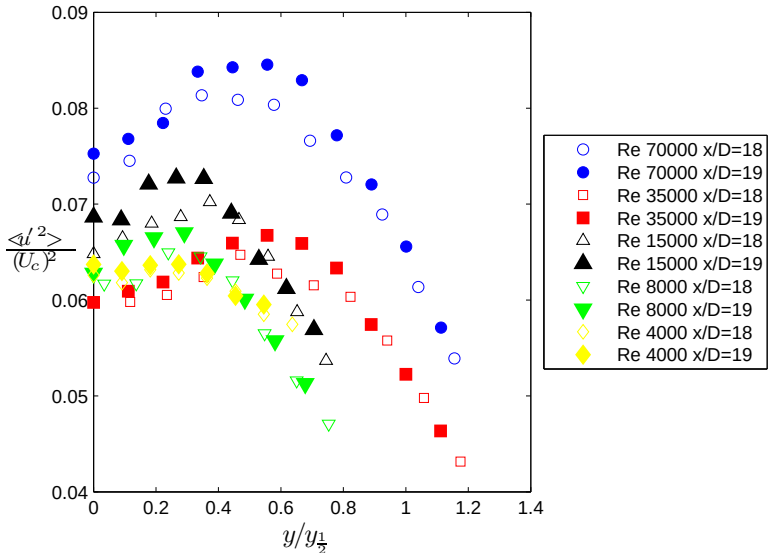

Figure 4.12: Radial profiles of the axial turbulence intensity at different Reynolds numbers

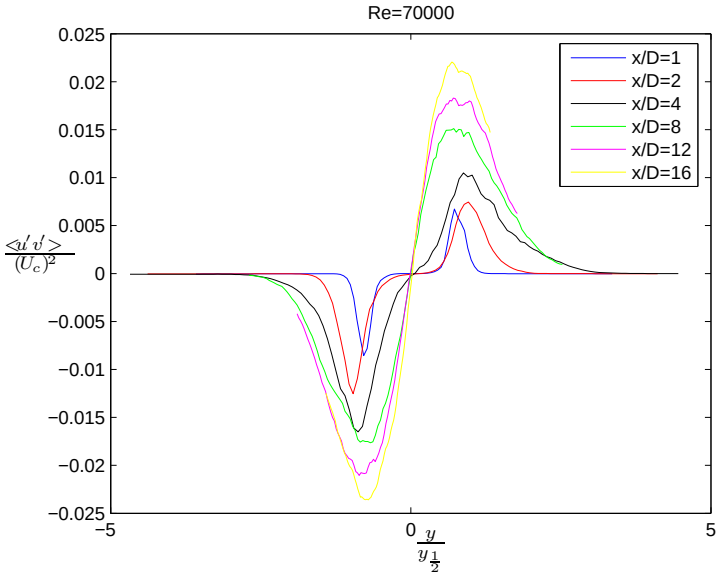

Figure 4.13: Radial profiles of the Reynolds shear stress along the axis of the jet

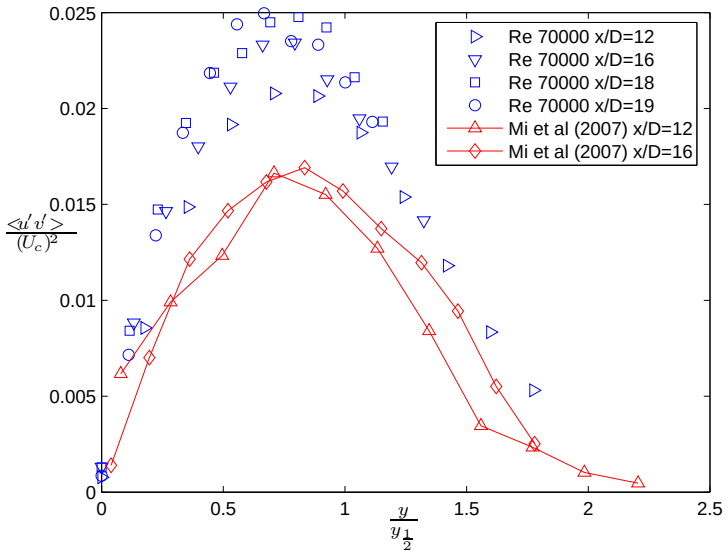

Figure 4.14: Radial profiles of the Reynolds shear stress in the far zone

self-similarity, and for Re=2000 due to the well-known reasons.

Basing on the amount of acquired images, has been possible to evaluate also the high order statistic of this jet, namely the skewness and the flatness. This is the first time that the influence of Reynolds number on high order statistics of orifice jets is investigated. First of all the longitudinal behaviour of these quantities has been investigated with regard to the tendency towards Gaussian distribution values. Figure 4.16 shows the behaviour of the skewness in the far zone $\left(\frac{x}{D} = 10 - 20\right)$ in correspondence to different Reynolds numbers.

An univocal tendency to the attainment of the Gaussian value can be stated for all the different Reynolds numbers, which means that, in the far field, all the different, with respect to the Reynolds number, orifice jets exhibit a random (gaussian) distribution of values. Moreover it can be seen how the more decreases the Reynolds number the nearer this Gaussian distribution of values is attained and the smaller are the initial fluctuations along this reference value.

As regards the flatness of velocity fluctuations a similar plot can be drawn, figure 4.17.

.

The attainment of Gaussian distribution conditions in correspondence

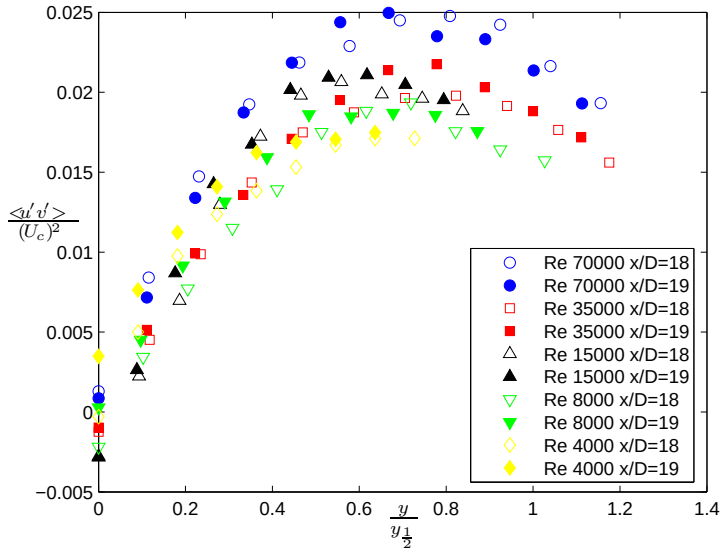

Figure 4.15: Radial profiles of the Reynolds shear stress at different Reynolds numbers

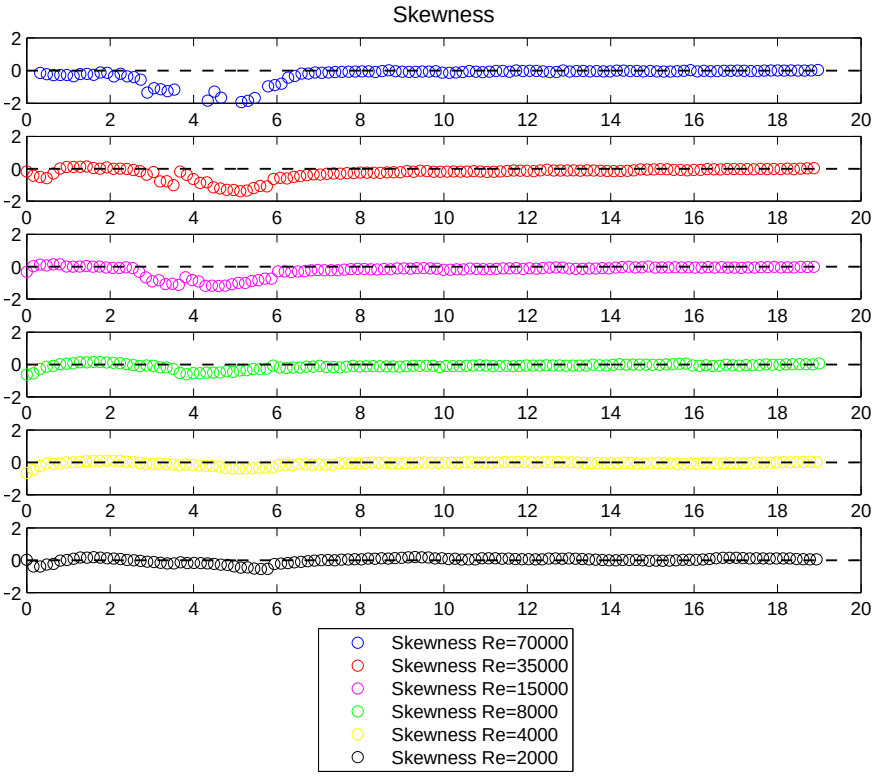

Figure 4.16: Longitudinal behavior of the skewness at different Reynolds numbers

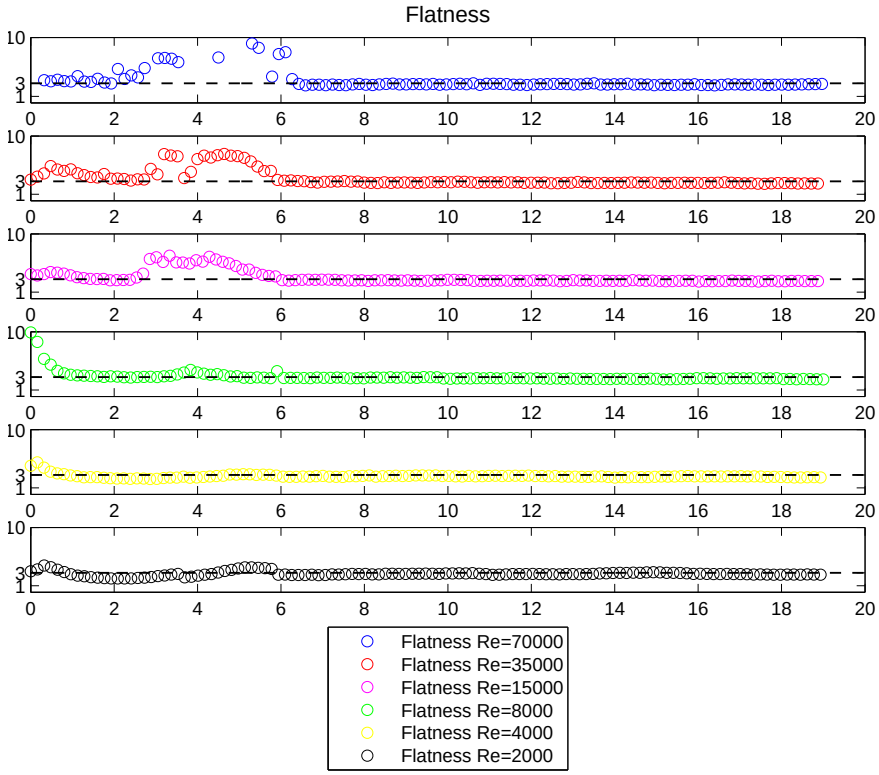

Figure 4.17: Longitudinal behavior of the flatness at different Reynolds numbers

to the far field can be clearly seen, as well as the influence of the Reynolds number that exhibits itself in the increasing fluctuations and in the moving further downstream of the position of attainment of the random distribution condition as the Reynolds number increases.

4.2 Large scale and small scale route to isotropy

An open issue of turbulent jets and especially of orifice jets concerns the fulfilment of large scale and small scale isotropy.

As already seen before, the ratio of streamwise to vertical *rms* velocities, i.e. $\frac{u'}{v'}$ [5],[7], is an indicator of large scales isotropy. Figure 4.18 shows a comparison between the results obtained at different Reynolds numbers and data present in literature concerning orifice jets (OP) [22] and [40], long pipe jets (LP) [7] and smooth contraction jets (SC) [54]. As already seen in section 3.2 all the results show a tendency towards a prevalence of longitudinal turbulence intensities compared to the transversal ones.

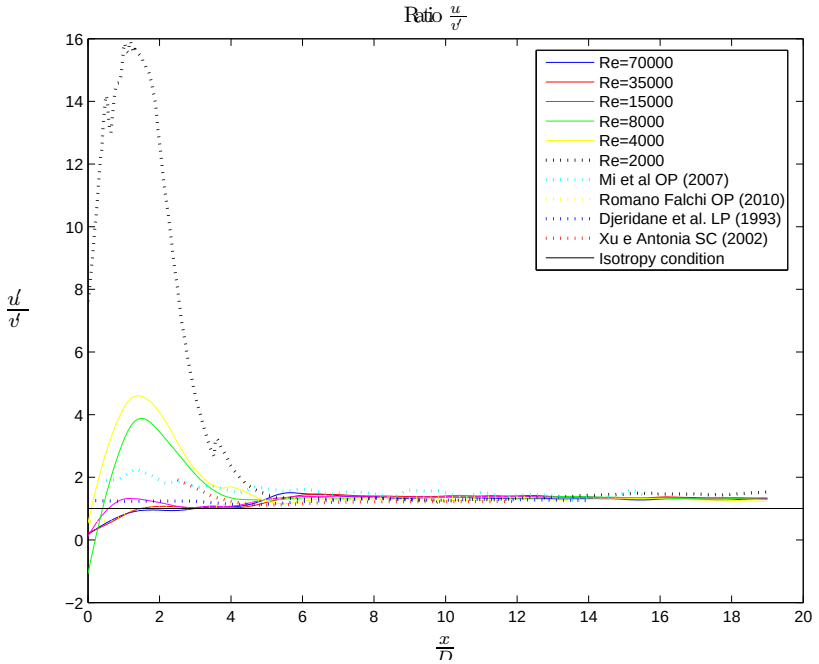

Figure 4.18: Axial evolution of large scale isotropy parameter $\frac{u'}{v'}$

Blowing up on the far field (figure 4.19) can be clearly seen how all the results tend to a value near to 1.3-1.4.

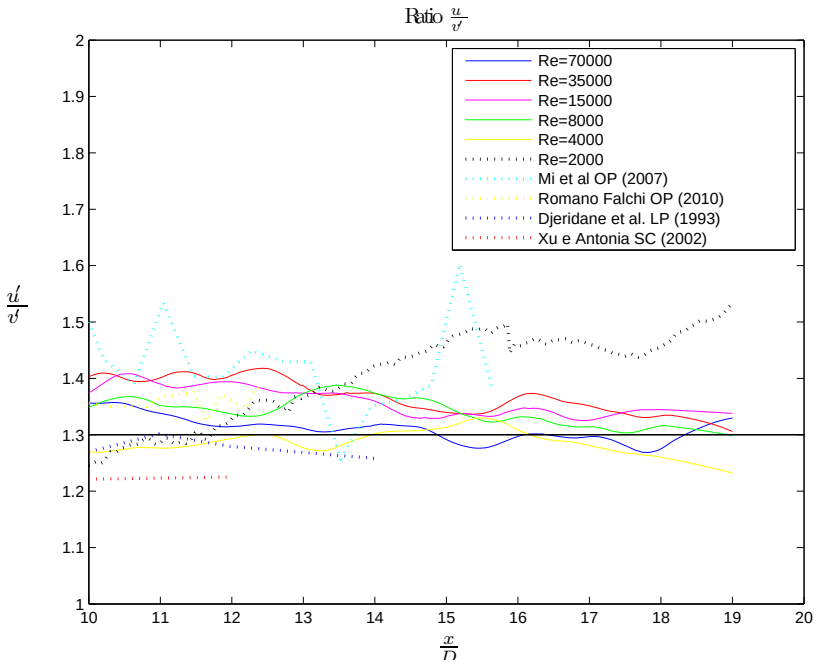

Figure 4.19: Magnificiation of the axial evolution of large scale isotropy parameter $\frac{u'}{v'}$

Moving to the small scale isotropy, the evaluation of the non-dimensional parameters K_1, K_3, K_4 and K_9 can be a useful tool to study the fulfillment of its conditions. First of all can be evaluated the ratio $K_1 = \frac{\left\langle \left(\frac{\partial v}{\partial y}\right)^2 \right\rangle}{\left\langle \left(\frac{\partial u}{\partial x}\right)^2 \right\rangle}$ which compares the spatial gradients of longitudinal and transversal velocities along their own direction. As can be clearly seen in figure 4.20 this condition gets almost satisfied already in the quite near field with no influence by the Reynolds number.

Involving also the cross-derivatives, the coefficient $K_3 = \frac{\left\langle \left(\frac{\partial u}{\partial y}\right)^2 \right\rangle}{\left\langle \left(\frac{\partial u}{\partial x}\right)^2 \right\rangle}$ can be evaluated. If the small-scale isotropy conditions were fulfilled its value should be equal to 2. As can be seen in figure 4.21 this condition doesn't seem to be satisfied even in correspondence to the far field, with some differences related to the Reynolds number, being the smaller Reynolds numbers and Re=35000 results nearer to the isotropic value.

The parameter $K_4 = \frac{\left\langle \left(\frac{\partial v}{\partial x}\right)^2 \right\rangle}{\left\langle \left(\frac{\partial u}{\partial x}\right)^2 \right\rangle}$ is similar to the K_3, involving the axial evolution of transversal velocity. Also the small scale isotropy conditions

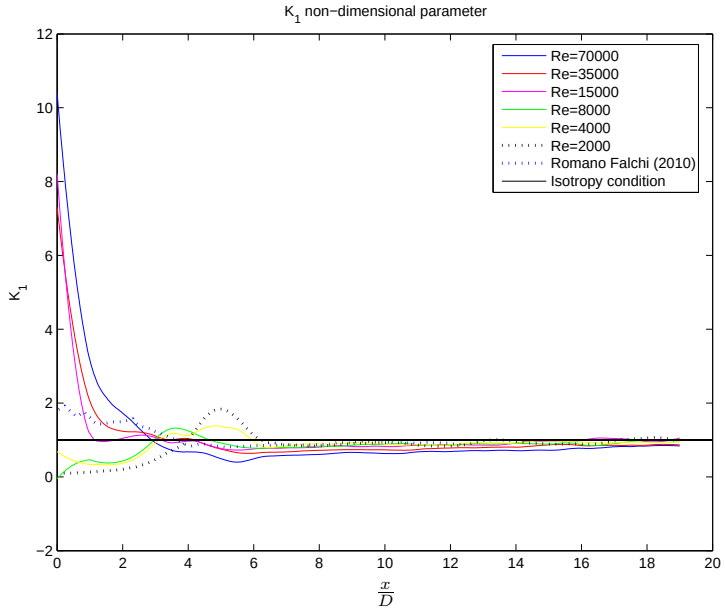

Figure 4.20: Axial evolution of small scale isotropy parameter K_1

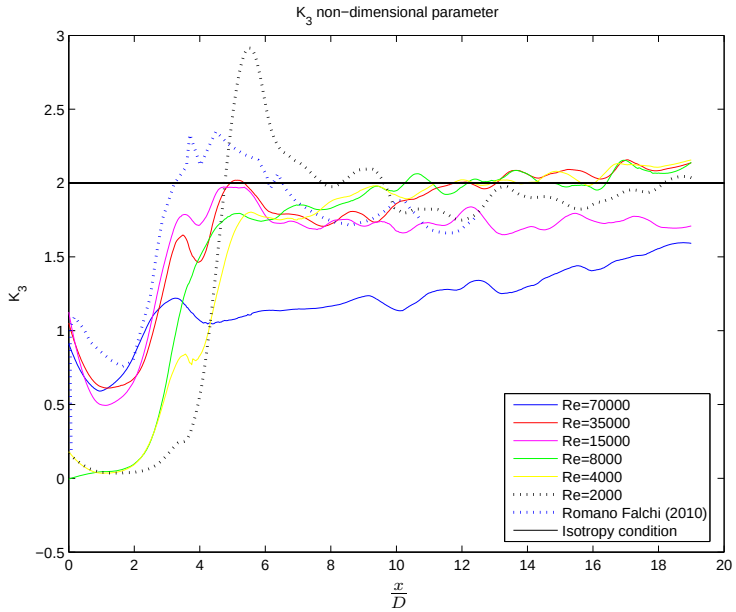

Figure 4.21: Axial evolution of small scale isotropy parameter K_3

related to this parameter $K_4 = 2$ are not satisfied being all the results far from the reference value, figure 4.22.

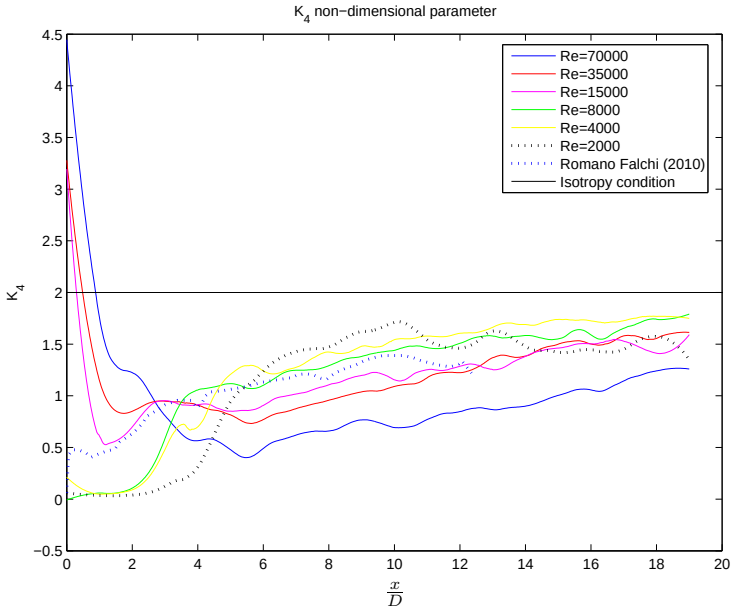

Figure 4.22: Axial evolution of small scale isotropy parameter K_4

Finally $K_9 = \frac{\left\langle \frac{\partial u}{\partial y} \frac{\partial v}{\partial x} \right\rangle}{\left\langle \left(\frac{\partial u}{\partial x} \right)^2 \right\rangle}$ depends simultaneously on cross derivatives of axial and transversal velocities. It has a trend similar to the one of K_3 with which it is related. Indeed the condition is not satisfied, while the smaller Reynolds results and Re=35000 are nearer to the reference value of small scale isotropy $K_9 = -05$, figure 4.23.

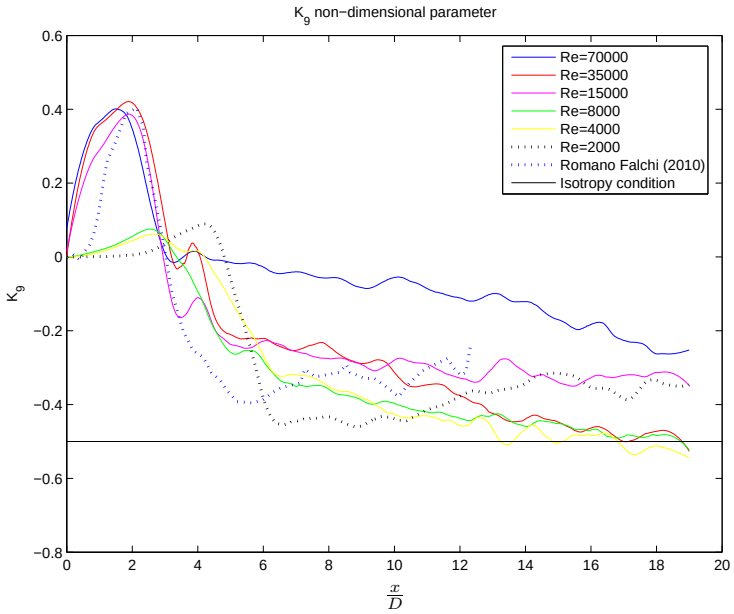

Figure 4.23: Axial evolution of small scale isotropy parameter K_9

Chapter 5

Stereo PIV Study

This chapter presents the results obtained making use of the Stereo-PIV technique. The aims of this part of the work were better understanding the orifice jet phenomenon, particularly concerning the third velocity component w, and then performing a comparison between the corresponding results obtained by different techniques.

In accord to these reasons, the study has been focused on two zones along the axis of the jet, from $\frac{x}{D} = 5$ to $\frac{x}{D} = 10$ and from $\frac{x}{D} = 15$ to $\frac{x}{D} = 20$, useful to study the far field behavior of the jet, and on two representative Reynolds number, namely Re=35000 and Re=8000, which are a fully turbulent and a transitional condition.

As already mentioned in chapter 2, the two cameras were placed on either side of the light sheet, as proposed by Willert in 1997 [51], figure 2.5. Thus both views can benefit of a higher and equal signal-to-noise ratio and an identical stretching.

In correspondence to each zone 10000 images (5000 couples) have been acquired in subsets of 1000 at a repetition rate of 8 Hz.

The Stereo-PIV technique requires a calibration process to associate image coordinates with physical coordinates. The most common approach to calibrating a stereo PIV imaging setup is based on acquiring images of planar calibration targets which are placed coincident with the light sheet plane and translated of a given distance. In present work the images have been acquired in correspondence to the light sheet plane, coincident with the vertical longitudinal axis of the jet, and translated along the z-axis of (-4.0, -2.0, +2.0, +4.0) mm. Moreover the calibration has been performed on

the basis of the pinhole method [52]. It originates in the fields of computer vision and photogrammetry, which commonly use so-called camera models to describe the imaging geometry. The simplest camera model reduces the imaging process to a pinhole configuration in which all rays passing from object to sensor must pass through a single point in space (pinhole), figure 5.1.

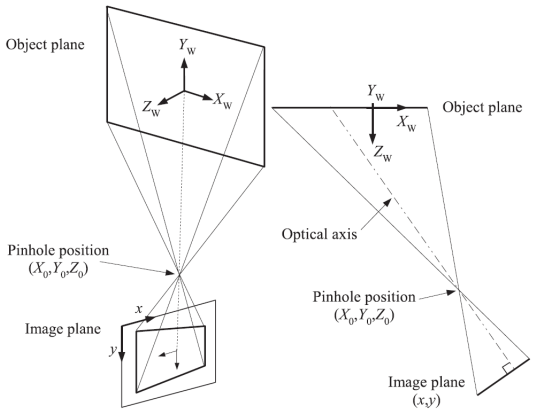

Figure 5.1: Simple pinhole imaging model. For clarity the projection onto the XZ plane is shown on the right, taken from [52]

Calibration approaches however assume that the calibration target is perfectly aligned with the center of the light sheet plane, but this alignment is difficult to be achieved. In order to account for slight out-of-plane positions and/or minor rotations of the target, a disparity correction procedure has been successfully performed. It is based on the acquisition of a limited amount of images, in present case 100 images, of a reference velocity field, e.g. a still water velocity field, and then on the performing of a cross-correlation of the corresponding frames of the two views, that is the frame A of the first view correlated with the frame A of the second view and similarly for the frames B of both the views. The resulting displacement field in fact represents the disparity of the views with respect to each other. The displacement data can now be used to correct the disparity by modifying the mapping coefficients accordingly.

Figure 5.2 shows the mean vector and scalar field in correspondence to $\frac{x}{D} = 5 - 10$ and Re=35000.

Obviously the transversal w velocity component is very small being the measurement zone vertical and in correspondence to the center of the jet.

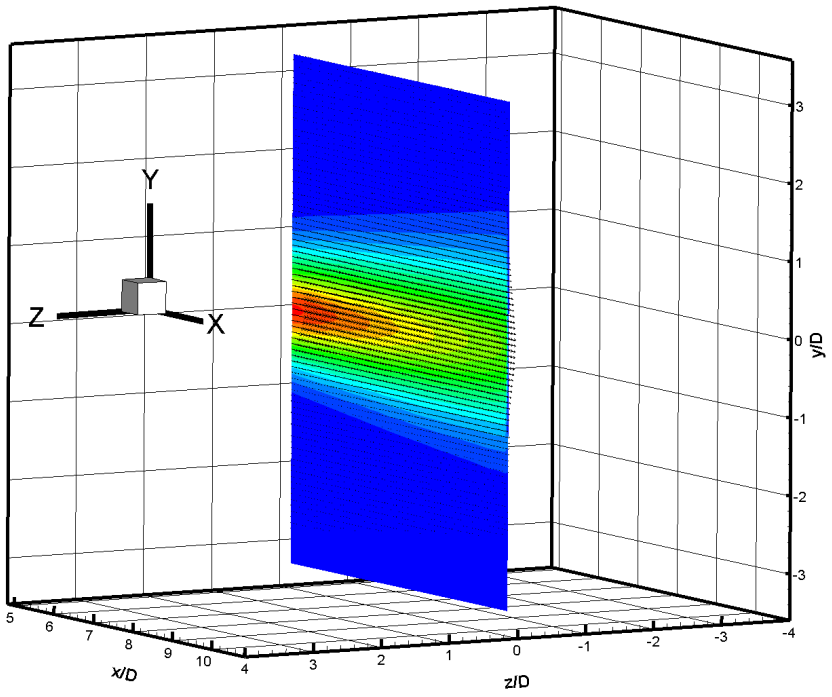

Figure 5.2: Vector and scalar mean field , Re=35000

5.1 Statistical moments

As already mentioned before, the Stereo-PIV technique allows to evaluate the three velocity components into a plane, in this case corresponding to the one of the PIV study, located along the axis of the jet. In order to avoid redundancy, all the results already shown as obtained by the PIV, although obtainable, will be not shown again. Moreover the results that can be obtained concerning the mean field of the w velocity component are extremely sensitive to the alignment of the laser beam. In fact, in correspondence to the location of the laser beam, the vertical plane along the axis of the jet, the w velocity component is null in average and any slight rotation around x and y axis involves non-zero values and differences in profiles shapes. Due to this fact the results involving the mean w velocity component will not be studied and shown.

Moving to the turbulence intensities, first of all a plot comparing the different velocity components can be made and it is shown in figure 5.3.

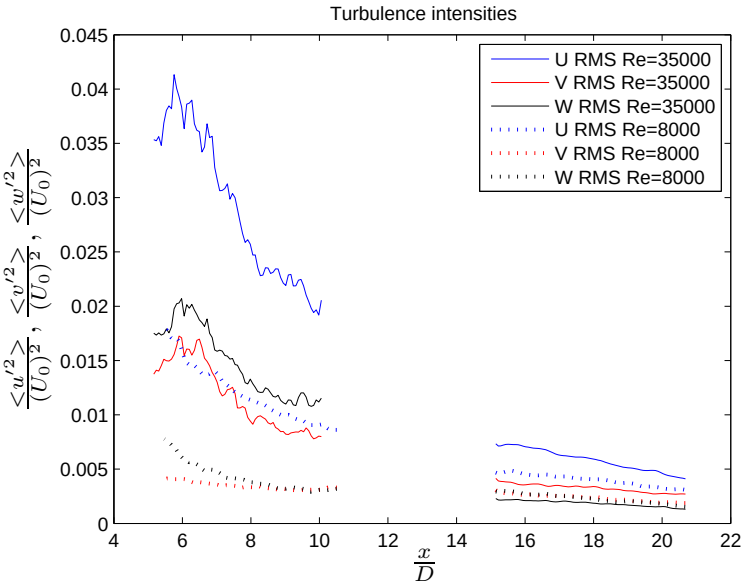

Figure 5.3: Longitudinal profiles of the turbulence intensities

From this figure several observations can be made. First of all, keeping Reynolds number constant, it can be stated that the turbulence intensities along the longitudinal direction (u component) are always higher than the two transversal ones (v and w). Than the fully turbulent con-

dition (Re=35000) shows a higher transversal turbulence intensity of the v velocity component in the near field and instead of the w velocity component in the far field, while in the transitional condition (Re=8000) the two transversal turbulence intensities are almost similar. Comparing the results obtained at different Reynolds numbers, it can be seen how in the near field the higher Reynolds number turbulence intensities are all higher than the lower Reynolds number ones , as it is obvious to be expected. In the far field these mutual relations still hold except the one involving the w component, becoming almost equal these turbulence intensities obtained at different Reynolds numbers.

An interesting study is the one concerning the attainment of self-similarity conditions, in particular applied to the w component turbulence intensities. Figures 5.4 and 5.5 show that in both cases the self-similarity is still close to be attained up to $\frac{x}{D} = 19$.

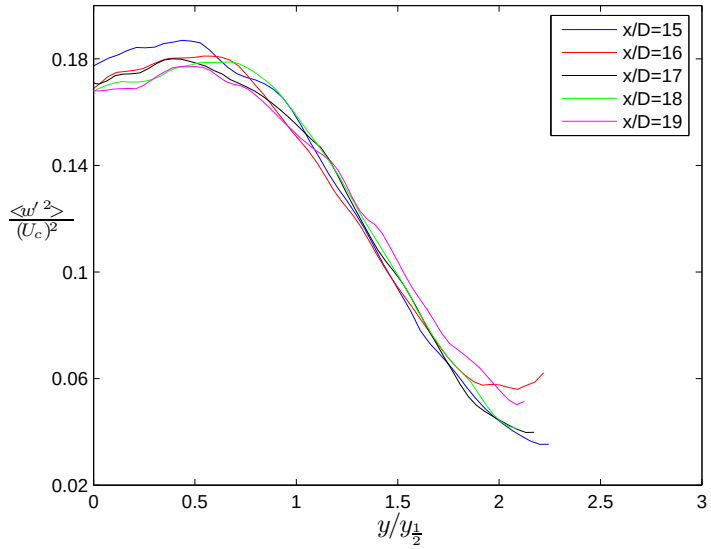

Figure 5.4: Radial profiles of the w component turbulence intensities in the far field, Re=8000

In addition the higher-order statistical moments skewness and flatness of the three velocity components have been evaluated and a comparison between these results has been carried out. In correspondence to Re=8000, figure 5.6 the skewness of all the velocity components and the flatness of the u and v components reach their Gaussian value while the w components exhibits an higher value, symptom of a peaked distribution, that is a relatively

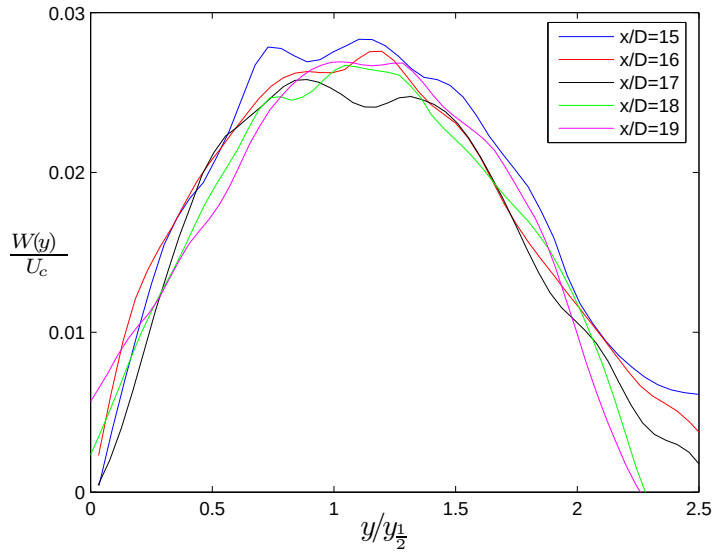

Figure 5.5: Radial profiles of the w component turbulence intensities in the far field, Re=35000

high probability of finding values of this velocity component both close to the mean and far from it.

Instead, figure 5.7 shows the results in correspondence to Re=35000. In the far field there is an univocal achievement of the Gaussian value both for the skewness and the flatness of the three velocity components.

5.2 Large scale and small scale route to isotropy

The Stereo-PIV allows to add some information usefull to the comprehension of the large scale and small scale route to isotropy, in this work concerning an orifice jet.

First of all the large scale isotropy indicators $\frac{v'}{w'}$ and $\frac{u'}{w'}$ can be evaluated. Figure 5.8 shows the behavior of the ratio between the two transversal velocity fluctuations v' and w' along the axis of the jet. In correspondence to Re=8000 the large scale isotropy condition seems to be near to be fulfilled, but a slight prevalence of the vertical fluctuations (v') still holds. In correspondence to Re=35000 instead this ratio tends to the value near to 1.3, which has already been encountered with regard to the ratios $\frac{u'}{v'}$ obtained studying different turbulent jets, see sections 3.2 and 4.2.

Figure 5.9 on the other hand shows the behavior of the $\frac{u'}{w'}$ indicator.

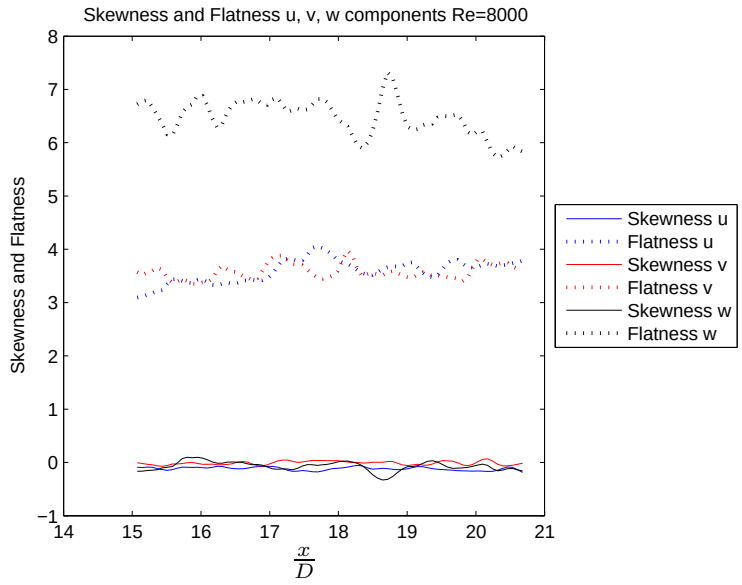

Figure 5.6: Longitudinal behavior of the skewness of the three velocity components, Re=8000

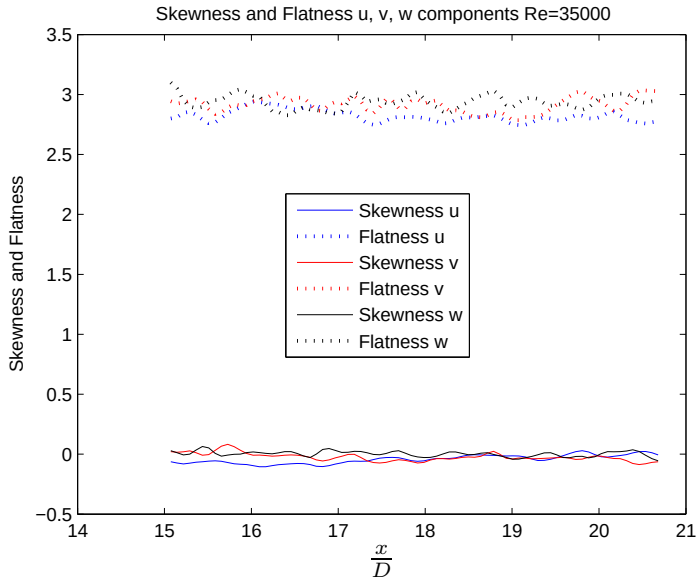

Figure 5.7: Longitudinal behavior of the skewness of the three velocity components, Re=35000

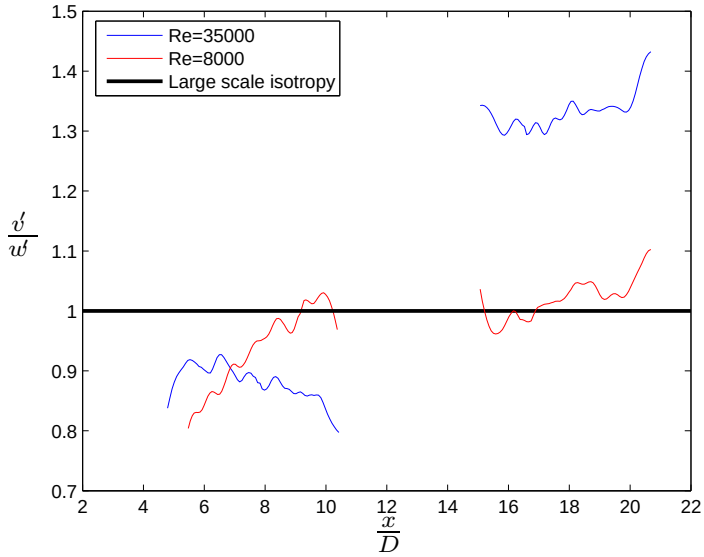

Figure 5.8: Axial evolution of large scale isotropy parameter $\frac{v'}{w'}$

Clearly the axial u' fluctuations are always higher than the transversal w' ones. In addition in correspondence to Re=8000 this ratio tends to the well-known and already mentioned value of 1.3, while in correspondence to Re=35000 the u' fluctuations in the far field become quite twice as much as the w' ones.

Clearly the large scale isotropy related to the velocity fluctuations is not attained until $\frac{x}{D} = 20$.

The study of the small scale route to isotropy becomes more complete becoming able to evaluate two further non-dimensional coefficients, namely K_6 and K_9.

The coefficient $K_6 = \frac{\left\langle \left(\frac{\partial w}{\partial x}\right)^2 \right\rangle}{\left\langle \left(\frac{\partial u}{\partial x}\right)^2 \right\rangle}$ compares the spatial gradients along the axial direction of the u and w velocity components, and therefore has an affinity with the K_4 from which is distinguished only by the transversal velocity component involved. As stated by equation 1.57 if the small scales isotropy conditions were fulfilled this coefficient should reach a value equal to 2. From figure 5.10 it can be seen how this condition is really far from being satisfied until $\frac{x}{D} = 20$ in correspondence to both the Reynolds numbers.

The coefficient $K_8 = \frac{\left\langle \left(\frac{\partial w}{\partial y}\right)^2 \right\rangle}{\left\langle \left(\frac{\partial u}{\partial x}\right)^2 \right\rangle}$ involves on the other hand the spatial

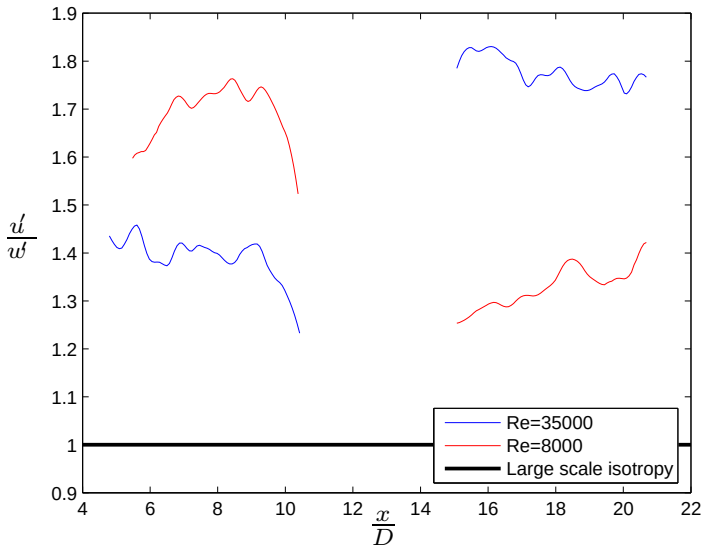

Figure 5.9: Axial evolution of large scale isotropy parameter $\frac{u'}{w'}$

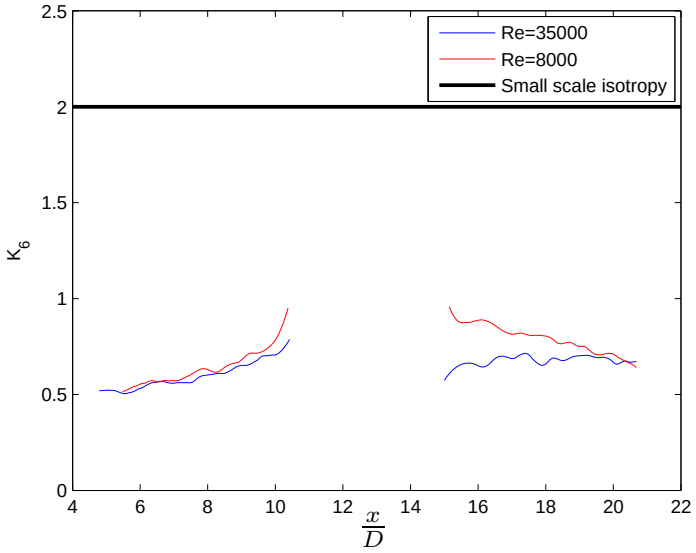

Figure 5.10: Axial evolution of small scale isotropy parameter K_6

derivative of the w velocity component in the y direction. The small scale isotropy involves this parameter to be equal to 2 (equation 1.57), but figure 5.11 shows how this condition is not satisfied even at $\frac{x}{D} = 20$.

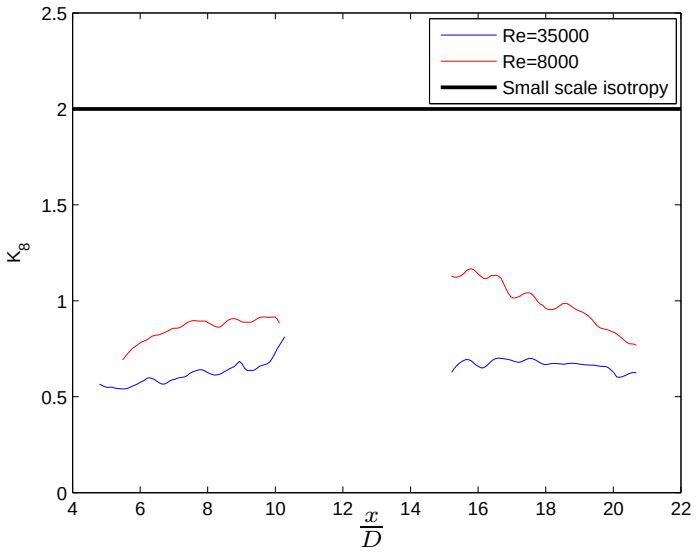

Figure 5.11: Axial evolution of small scale isotropy parameter K_8

5.3 Comparisons

Data obtained by the two techniques, PIV and Stereo-PIV, can be compared in order to evaluate the accuracy of the latter relative to the former. First of all the longitudinal behavior of the axial velocity can be compared. Figures 5.12 and 5.13 show the profiles in correspondence to Re=8000 and Re=35000 respectively.

Clearly a good agreement between the corresponding results can be stated.

Then a comparison of turbulence intensities in the far field can be made.

Figure 5.14 shows a comparisons of the axial profiles of the velocity components in correspondence to Re=8000. The Stereo-PIV seems to underestimate both the velocity components u and v.

Figure 5.15 on the other hand shows the same comparison in correspondence to Re=35000. In this case on the contrary the Stereo-PIV overestimate the both the components. These discrepancies can be ascribed to the

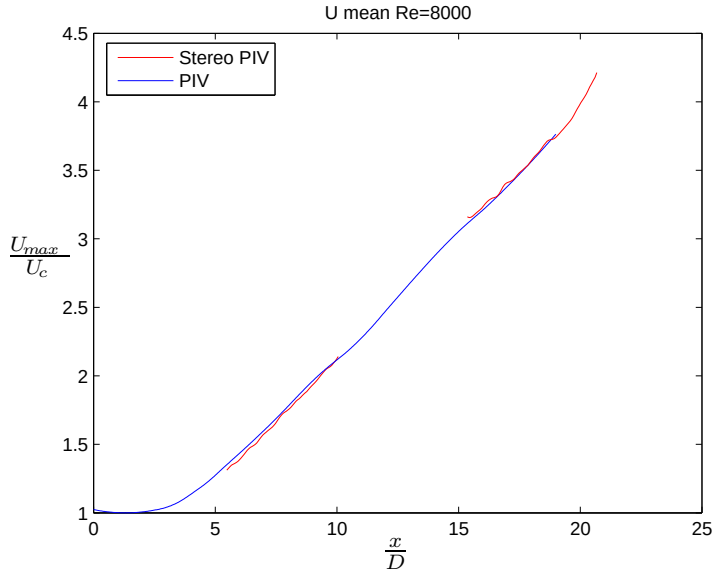

Figure 5.12: Comparison of the longitudinal profiles of the axial velocity, Re=8000

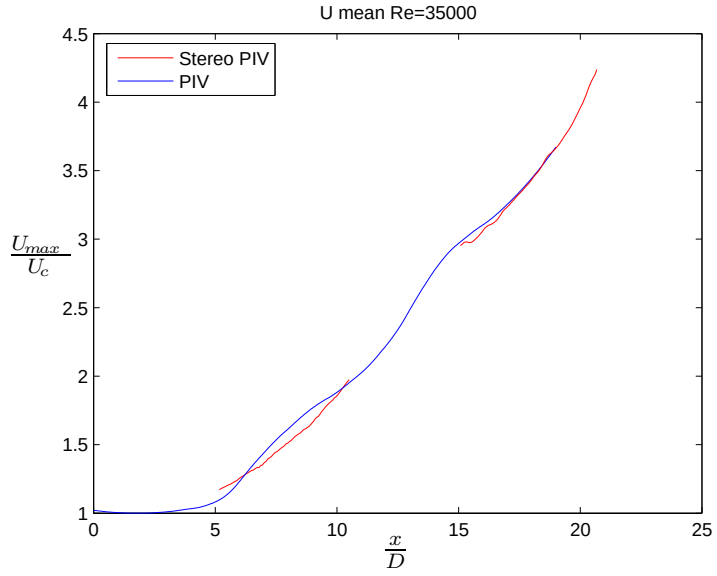

Figure 5.13: Comparison of the longitudinal profiles of the axial velocity, Re=35000

turbulence intensities of the third velocity component which can influence the results on the other components.

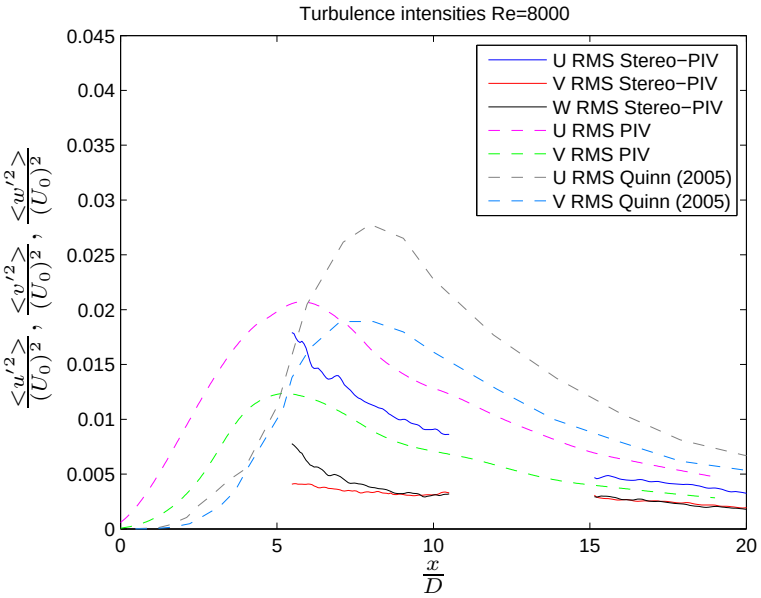

Figure 5.14: Comparison between the longitudinal profiles of the turbulence intensities, Re=8000

In both cases a result present in literature (Quinn 2005 [33]), obtained making use of Hot wire Anemometry technique in correspondence to a Reynolds number near to 184000, is also reported. The turbulence intensities of the u and v component show a decrease and then an increase of their value relative to the jet exit velocity U_0 and the location of the maximum turbulence intensities along the axis moves downstream as the Reynolds number increases. It should be pointed out that the maximum of the turbulence intensities is located more downstream than the maximum velocity (vena contracta).

Figures5.16 and 5.17 show the radial profiles of the axial turbulence intensities obtained by the PIV and the Stereo PIV in correspondence to Re=8000 and Re=35000.

From this figures it is evident how the Stereo-PIV underestimates the turbulence intensities, while the shape of the profile seems to be preserved. Moreover the results are compared with the one of Mi et al. (2007) [22] in correspondence to a comparable downstream distance. Stereo-PIV results seem to be nearer to the Mi ones compared to the PIV ones, however it

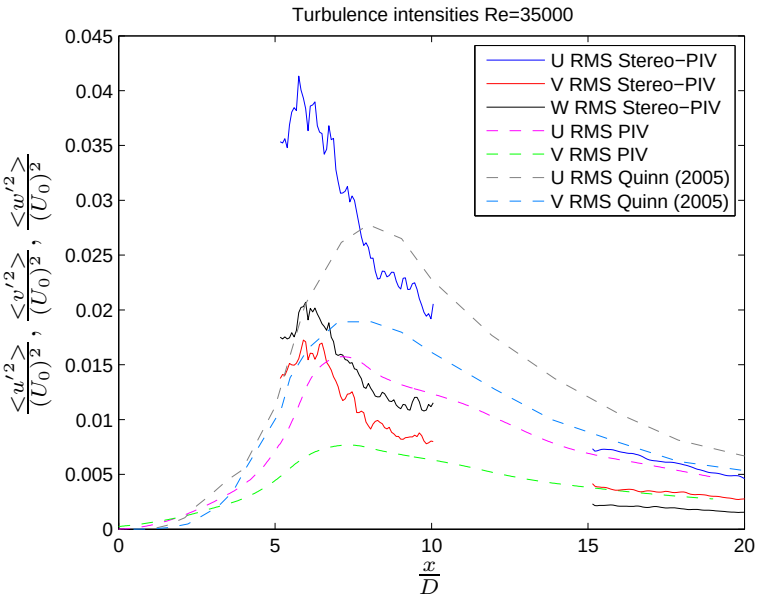

Figure 5.15: Comparison between the longitudinal profiles of the turbulence intensities, Re=35000

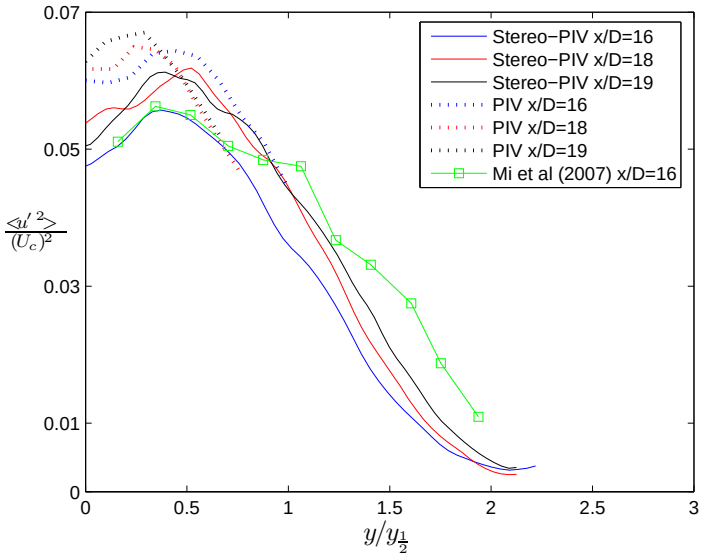

Figure 5.16: Comparison of the radial profiles of the axial turbulence intensities, Re=8000

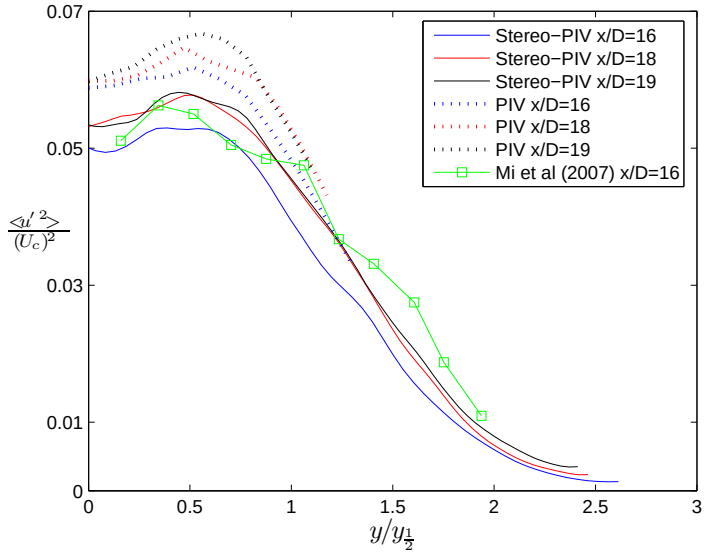

Figure 5.17: Comparison of the radial profiles of the axial turbulence intensities, Re=35000

should be stated that Mi setup is quite different, having a short pipe right upstream to the orifice plate, so that their jet behaves more like pipe jets [22], which have in comparison a lower value of turbulence intensity [23].

Then high order statistical moments, namely skewness and flatness, of the u velocity component can be evaluated. Figure 5.18 compares the results obtained by the two techniques in correspondence to Re=8000.

The two results are qualitatively similar, except the flatness in the far field which, according to the PIV, has already reached the Gaussian value, while according to the Stereo-PIV is still far from assuming it, involving an higher number of events (values of the u' velocity fluctuations) far from the mean value.

Figure 5.18 compares the corresponding results setting the Reynolds number to a value equal to 35000.

It is evident how the results obtained by the two measurement techniques are similar in the far field, showing an attainment of the Gaussian value, while in the near field the values of both the skewness and the flatness related to the Stereo PIV are higher the corresponding ones of the PIV, involving a bigger amount of values far from the mean with a predominance of the higher ones with respect to the lower ones.

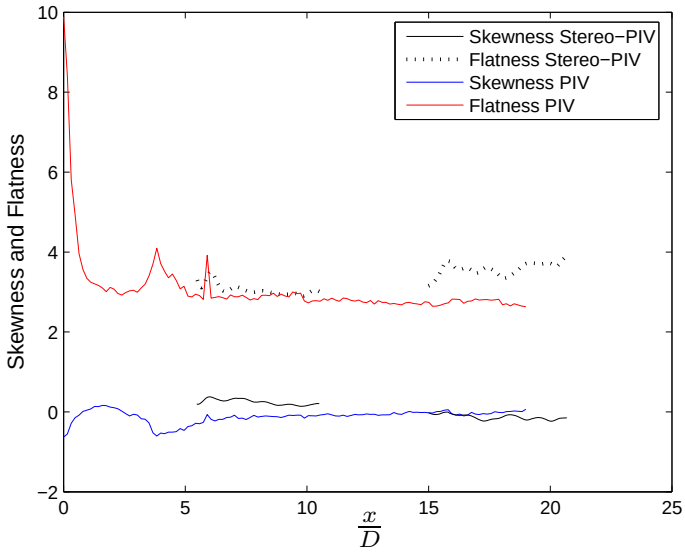

Figure 5.18: Comparison of the Skewness and Flatness longitudinal profiles, Re=8000

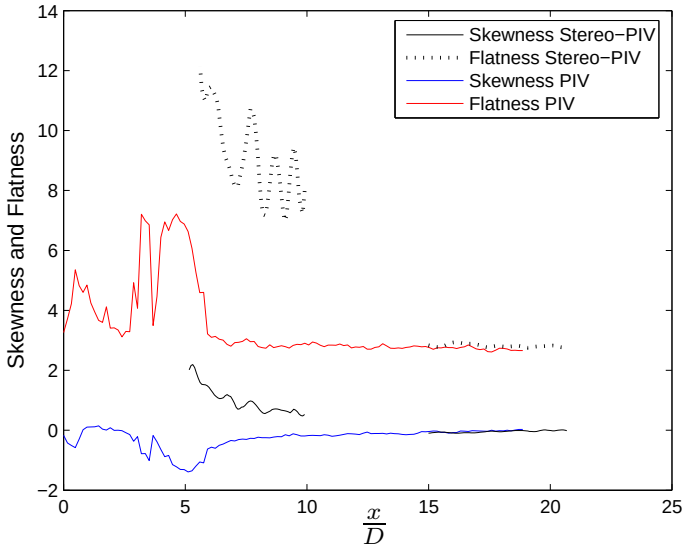

Figure 5.19: Comparison of the Skewness and Flatness longitudinal profiles, Re=35000

Then some comparisons can be made on the results related to investigation of the isotropy of the jet.

First of all the ratio $\frac{u'}{v'}$, indicator of large scale isotropy, can be evaluated. Figure 5.20 shows as usual a comparisons of the results obtained with the two experimental techniques.

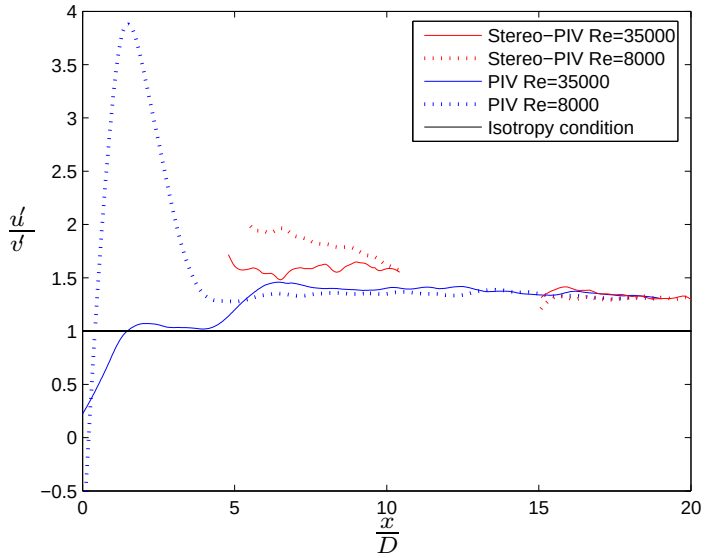

Figure 5.20: Comparison of the behavior of the large scale isotropy indicator

Notwithstanding some differences in the zone $\frac{x}{D} = 5 - \frac{x}{D} = 10$, the trend towards a value near to 1.3 in the far field is confirmed by both the techniques.

Moreover the fulfillment of small scale isotropy conditions can be studied and compared. The parameter K_1 compares the spatial derivatives of longitudinal (u) and vertical (v) velocities along their own direction. From figure 5.21 a closeness between the different techniques results can be stated with the Stereo-PIV ones a little bit shifted away from the isotropy condition ($K_1 = 1$) satisfied by the PIV data.

The coefficient K_3 compares the axial and the vertical spatial gradients of the axial velocity. Figure 5.22 shows how the Stereo-PIV results are quite different from the PIV ones, and turn out to be further from the isotropy condition ($K_3 = 2$) which is close to be attained in the far field according to the PIV technique.

The coefficient K_4 involves the axial gradient of the axial and vertical

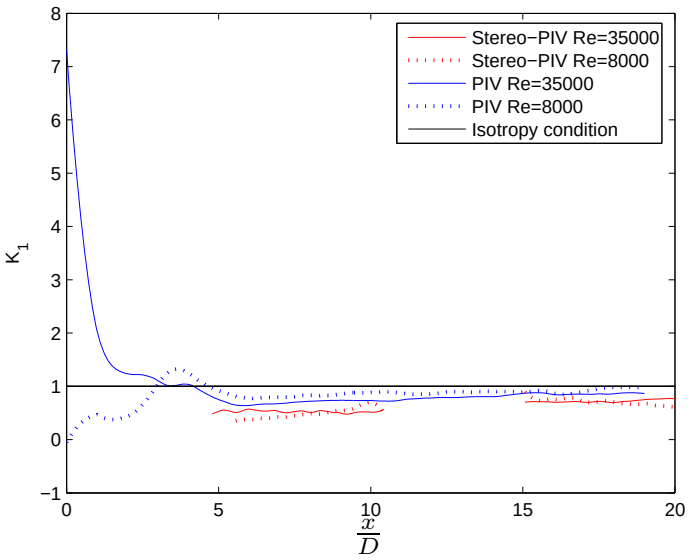

Figure 5.21: Comparison of the behavior of K_1 small scale isotropy indicator

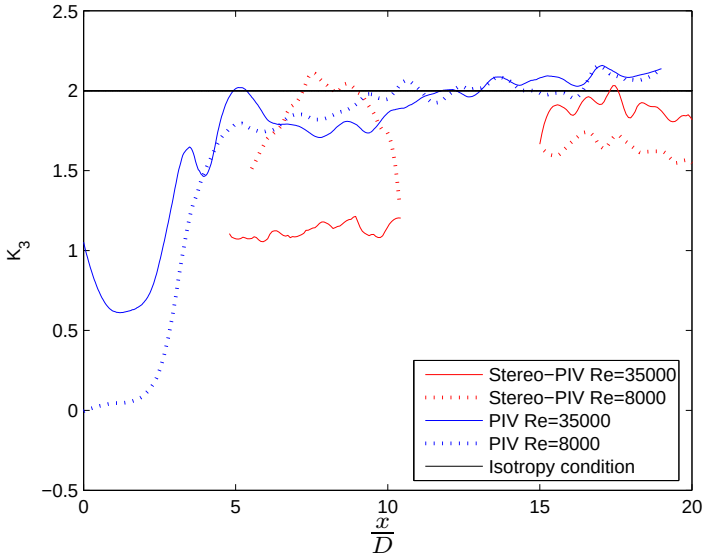

Figure 5.22: Comparison of the behavior of K_3 small scale isotropy indicator

velocities and compares their behavior. The small scale isotropy condition ($K_4 = 2$), results still far from being attained both by the PIV and the Stereo-PIV results, being the latter always further from the reference value, as can be seen in figure 5.23

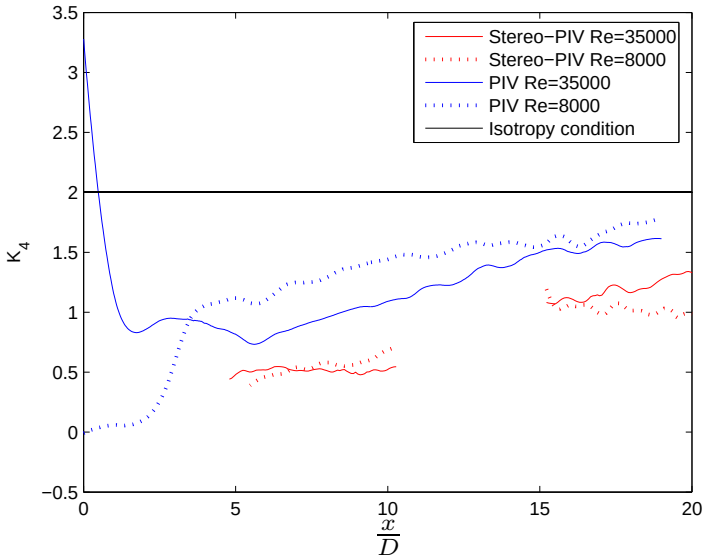

Figure 5.23: Comparison of the behavior of K_4 small scale isotropy indicator

Finally the K_9 coefficient involves the gradient of the axial velocity in the vertical direction and of the vertical velocity in the axial direction. Its reference small scale isotropy value ($K_9 = -0.5$) is reached by the PIV results and not by the Stereo-PIV results, which are as usual further from the isotropic value, as can be seen in figure 5.24.

Clearly the Stereo-PIV reveals to generate some errors in the evaluation of the spatial derivatives, which can be estimated to be in the order of 15-20 % in accordance to what can be found in literature, e.g. the paper of Wieneke and Taylor (2006) [50] which estimated Stereo-PIV error in spatial derivatives evaluation on the order of about 10 % for all derivatives. Moreover higher errors are expected in the zones of higher gradients.

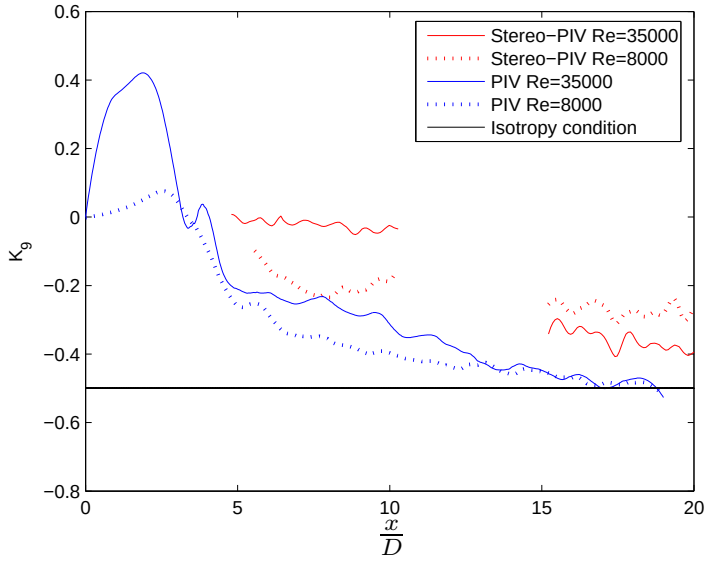

Figure 5.24: Comparison of the behavior of K_9 small scale isotropy indicator

Chapter 6

Defocusing PIV Study

This chapter presents the results obtained making use of the Defocusing-PIV technique. The aims of this part of the work were getting an overall view on the volumetric structure of an orifice jet and moreover comparing these results with the ones obtained by the planar techniques.

The study has been focused on the same two zones , from $\frac{x}{D} = 5$ to $\frac{x}{D} = 10$ and from $\frac{x}{D} = 15$ to $\frac{x}{D} = 20$, and two Reynolds numbers, Re=35000 and Re=8000, studied making use of the Stereo-PIV. The studied volume measured 5 D x 5D x 5D.

In correspondence to each zone 15000 images (5000 triplets) have been acquired at a repetition rate of 8 Hz.

A good calibration is critical for making good Defocusing-PIV measurements. The Defocusing-PIV system uses a three-aperture pinhole camera model to measure particle 3D positions in a volume. However the real camera deviates from the perfect pinhole camera due to several possible factors including the mechanical misalignment of CCD sensors, the optical distortion of lenses and wall, the deviation from pinhole camera model etc... Performing a good system calibration can reduce these errors down to a subpixel level.

During the calibration, a calibration target with a known grid pattern is mounted on a one-dimensional traverse system aligned with the z axis of camera coordinate system. The images of the calibration target are captured at multiple depth positions so as to scan the entire measurement volume with constant jog steps. The target has a 200 x 200 mm grid of dots equally spaced at 5 mm. The center dot of the grid is marked by 3 missing dots

around it; this allows the software to locate it and to take it as a reference in the reconstruction of the 3D positions. The length of the scanned area was 10 cm moving at steps of 5 mm. An useful method to evaluate the goodness of the calibration is reconstructing a regular grid analyzing the reconstructed positions of the target dots along the scanning movement, making use of the calibration images 6.1.

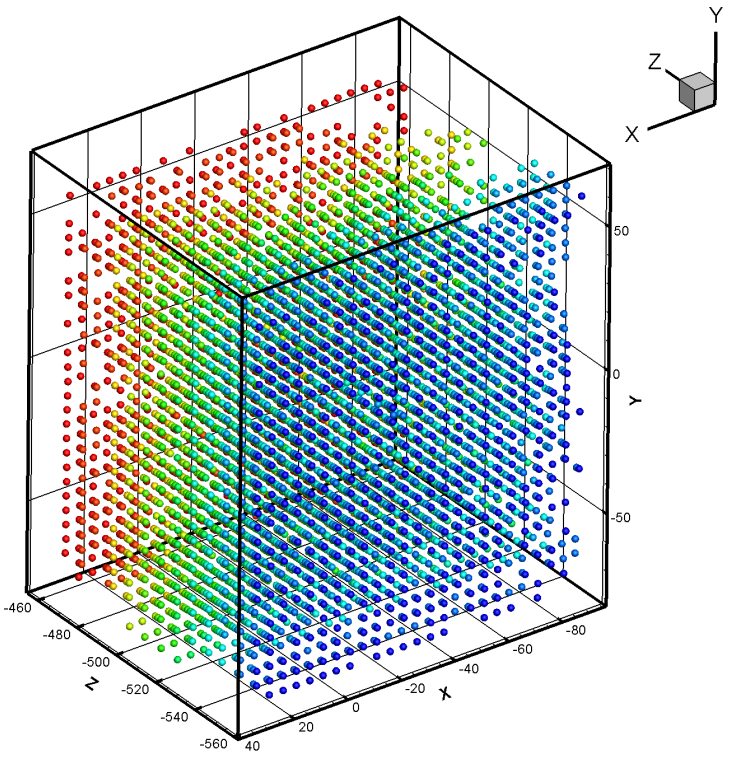

Figure 6.1: Grid points reconstruction

If the calibration is correct, in a top view all grid points should line up along the z positions where the calibration images were taken 6.2.

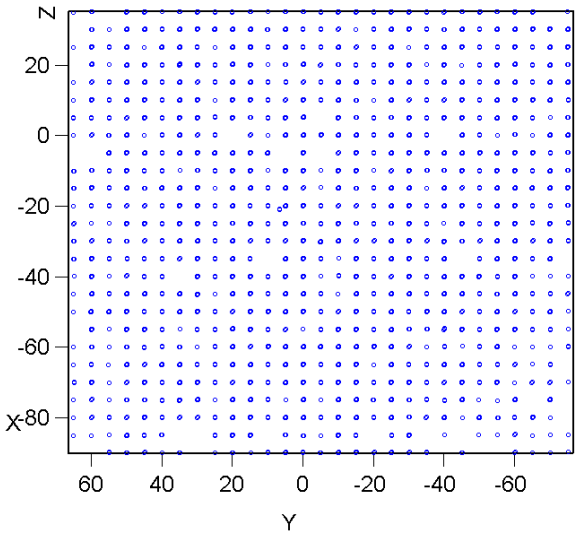

Figure 6.2: Top view of grid points reconstruction

6.1 Statistical moments

Defocusing-PIV data are still under analysis.

6.2 Large scale and small scale route to isotropy

Defocusing-PIV data are still under analysis.

Chapter 7

Conclusions

This chapter presents the most salient outcomes of the research project presented in this thesis.

The near and far fields of a turbulent orifice jet have been investigated by means of experimental non-intrusive optical techniques both spatial and volumetric. These techniques move from a planar information on two velocity components (PIV), through a planar information on three velocity components (Stereo-PIV), till volumetric data on three velocity components (Defocusing PIV). The raising amount of information is however in inverse proportion to their quality, as it has been shown in the comparisons between the results obtained by the different techniques. The PIV study has been extended to six different Reynolds numbers, namely 70000, 35000, 15000, 8000, 4000 and 2000, ranging from a high velocity condition to a small velocity one, in order to study the dependence on this quantity of jet statistical features. Moreover the study has been extended also to the so called "route to isotropy", making use of large scale and small scale indicators, the latter involving spatial derivatives., without analyzing coherent structures.

Hence a preliminary study on the influence of spatial resolution, related to different magnifications, on the resulting features of a jet has been carried on in order to properly design the setup. This study has highlighted the limited influence of this kind of spatial resolution on low order statistical moments, which slightly rises as the order of the statistics becomes higher. Then small scale features of the jet have been examined, particularly with interest to the evaluation of spatial derivatives of velocity components and then to the fulfillment of isotropy hypotheses of the jet. Based on those data,

an influence of spatial resolution moderate on the overall behavior of spatial derivatives and on the deductions about symmetry hypotheses and high on the determination of local features of such a jet is attained. Generally speaking, the size of the overall acquired region should not exceed a limiting value which is around 30-40 Taylor microscales. For smaller resolutions (i.e. for an acquired region which is larger than 50 Taylor microscales), the statistical moments are smoothed starting from mean velocity (at the vena contracta, x/D=0.5) and propagating further downstream as the order of the moment increases, e.g. the small scale contribution raises.

The PIV study has highlighted the dependency of the "vena contracta" phenomenon on the Reynolds number, moreover turning out to be a feature only of turbulent orifice jets, not of the laminar ones. The axial velocity shows a far field linear decay rate common to most the higher Reynolds numbers. The self-similarity of radial profiles of the statistical moments has been discovered in the far field, while the results present in literature didn't encounter it because limited to a smaller and nearer zone [22]. Then the dependence of the position of attainment of the Gaussian value of the skewness and flatness has been evaluated. With regard to the route to isotropy two main results have been brought to light. First of all the tendency of the large scale isotropy indicator towards a value suggesting an anisotropy which is common to several turbulent jets has been confirmed. Moreover, concerning the small scale isotropy, an incomplete attainment of the small scale conditions related to the spatial derivatives, especially the cross ones, can be stated.

Moreover a study based on the Stereo-PIV technique has been carried out in order to study the w velocity component and compare the results obtained by the two techniques. The w velocity component too reaches the self-similarity condition in the far field and shows a lower turbulent intensity compared to the u axial one and to the v transversal one. The Stereo-PIV results compared with the PIV ones show a good agreement of the mean field results while the turbulence intensities and the skewness and flatness results present some mismatches in the same way that spatial derivative related statistics, like the small scale isotropy indicators, do, especially the ones related to the cross derivatives.

Chapter 8

Acknowledgments

The Author would like to thank Prof G. P. ROMANO for the guide and the valuable scientific support, and the ITALIAN SHIP MODEL BASIN (I.N.S.E.A.N.), in particular Eng. Fabio DI FELICE and Francisco PEREIRA for the technological support.

The Author would like also to thank Prof. A. LECUONA and Prof. B. GANAPATHISUBRAMANI for the kind and careful reviews of the thesis.

Chapter 9

Appendix

Nowadays, it is common making use of imaging technique to obtain global quantitative non invasive information on flow fields. In most of hydrodynamic applications, the measurement of velocity fields is performed by means of PIV (Particle Image Velocimetry). Employing a similar set-up, particle size can be easily evaluated through defocusing techniques. Among the variety of such techniques, we used ILIDS (Interferometric Laser Imaging Droplet Sizing). It is a non-invasive technique, based on the interference between reflected and refracted rays by a transparent particle, which can provide the distribution of size of individual spherical droplets or bubbles on the illuminated plane. A set-up similar to that used in 2D PIV can be employed thus naturally claiming for the extension to simultaneous velocity-size measurements. However, such an extension is not straightforward due to the conflicting requirements of defocused particle images in ILIDS whereas almost in focus for PIV. Moreover, size measurements have been successfully performed especially in the study of sprays, i.e. water droplets in air where an optimal light scattering is attained. Applications of the proposed technique to air bubbles would be of strong relevance for the study of incipient cavitation in marine propeller wake (Liu et al., 1993 [13]) and other engineering device as well as in applied research for the reduction of greenhouse gas into seawater (Hirai et al., 1997 [8]).

The first application of this technique to droplets started with the work of Konig et al. (1986) [12]. They focused a stream of mono-dispersed droplets and recorded the fringe pattern on a linear array detector at a scattering angle equal to 45°. So far, they investigated the geometrical optics relation-

ship between droplet diameter and number of fringes. Unfortunately, with this experimental configuration they could study only a single droplet at a point. Later, an experimental configuration using the out of focus principle has been developed by Ragucci et al. (1990) [16]. Their setup was made by a laser sheet illuminating droplets and by a CCD camera acquiring at a scattering angle equal to 90° the out-focus images. According to this configuration, the interferometric pattern of each droplet could be imaged separately by Lorenz-Mie calculation. However, due to limitation of the intensity-peak counting method, it was possible measuring only patterns obtained by a single droplet. Then, Glovers et al. (1995) [7], combined the 45° scattering angle and the geometric analysis of Konig et al. (1986) [12] with the out of focus analysis of Ragucci et al. (1990) [16]. They developed the basis of ILIDS technique which allows measuring the interferometric pattern of several droplets simultaneously because their images are separated on the acquired fields.

Bubbles measurements have been firstly realized by Niwa et al. (2000) [15] and Maeda et al. (2000) [14]. Starting from geometrical optics, they derived the relation between bubble diameter and number of fringes valid for this case, thus being able to measure bubble size. They also pointed out limitations on the use of this technique in practical applications due to the possible overlapping between spatially close particles in out of focus images. Two possible solutions to this problem have been proposed. The first by Kawaguchi et al. (2001, 2002) [9], [10] and Kobayashi et al. (2002) [11] is obtained by an optical compression setup using a pair of cylindrical lenses. In this way, each particle generates a linear interferogram instead of a circular one, reducing overlapping among nearby particles. On the other hand, this technique seems to be more sensitive to the non spherical shape of particles and to optical misalignment, which can cause changes in fringe orientation. Almost at the same time, Damaschke et al. (2001, 2002) [2], [3] employed two cameras to acquire simultaneously on focus and out of focus images. Therefore, they identified particle location (to be used in particle displacement detection schemes) through the on focus image and evaluated their diameters through the out of focus one. So they improved particle measurements even if requiring a more complicated setup than before. In this work, we would like to retain the advantage of using a single camera set-up aiming to be able to derive simultaneously the velocity and size of

cavitation bubbles in water from defocused images.

9.1 Theoretical background

When a coherent laser sheet illuminates a particle, the incident light is partially reflected from the surface and partially transmitted and refracted in both forward and backward directions after one or more internal reflections (Van de Hulst, 1957 [17]). The theory of geometrical optics allows deriving the relationship between fringes and particle diameter considering only external reflection and first order refraction, which dominate the forward scattering region. The phase difference at the same scattering angle, θ_r, between reflected and first order refracted rays can be evaluated (Ragucci et al. 1990 [16], Maeda et al. 2000 [14], Niwa et al. 2000 [15], Damaschke et al. 2001 [2], 2002 [3], 2005 [4]):

$$\sigma_0 - \sigma_1 = \frac{2\pi d n_e}{\lambda}\left[sin\left(\frac{\theta_r}{2}\right) - \sqrt{m^2 + 1 - 2mcos\left(\frac{\theta_r}{2}\right)}\right] \tag{9.1}$$

where the real refractive index inside the particle is indicated as n_i, the surrounding medium refractive index as n_e, the relative refractive index as $m = \frac{n_i}{n_e}$ (here we assume $m > 1$, as for droplets in air), λ is the light wavelength and d is the particle diameter. By differentiating such a phase difference, and considering that in order to obtain the maximum and minimum intensity variation between fringes, the infinitesimal variation of the phase difference $\sigma_0 - \sigma_1$ should be equal to 2π, it is possible to write

$$\Delta(\sigma_0 - \sigma_1) = \frac{\pi d n_e}{\lambda}\left[cos\left(\frac{\theta_r}{2}\right) + \frac{msin\left(\frac{\theta_r}{2}\right)}{\sqrt{m^2 + 1 - 2mcos\left(\frac{\theta_r}{2}\right)}}\right]\Delta\theta_r = 2\pi \tag{9.2}$$

where $\Delta\theta_r$ is the angular spacing between the fringes.

If we now consider the condition $m < 1$ (as for gas bubbles in liquid flow), the only difference is a change of sign reflecting the different geometry of refracted rays, so that it is possible to obtain the relationship between particle diameter d and fringe angular spacing $\Delta\theta_r$

$$d = \frac{2\lambda}{\Delta\theta_r n_e}\left[cos\left(\frac{\theta_r}{2}\right) - \frac{msin\left(\frac{\theta_r}{2}\right)}{\sqrt{m^2+1-2mcos\left(\frac{\theta_r}{2}\right)}}\right]^{-1} \tag{9.3}$$

Lastly, by introducing fringe separation δ, the magnification factor M and the defocusing distance *def*, in the case of air bubbles in water $\left(m = \frac{1}{n_e} = 0.75\right)$, as for our interest, it is obtained from equation 9.3

$$d = \frac{2\,m\,\lambda\,M\,def}{\delta}\left[cos\left(\frac{\theta_r}{2}\right) - \frac{m\,sin\left(\frac{\theta_r}{2}\right)}{\sqrt{1+m^2-2\,m\,cos\left(\frac{\theta_r}{2}\right)}}\right]^{-1} \tag{9.4}$$

The previous relationship 9.4 can be written in a more compact form as

$$d = \frac{K}{\delta} \tag{9.5}$$

where the factor K is a function of relative refractive index, light wavelength, magnification factor, defocusing distance and scattering angle. Thus, large fringe separations correspond to small particle diameters and viceversa. In the present investigation, we decided to estimate fringe spatial frequency (i.e. wavenumber k) instead of their separation $\left(k = \frac{2\pi}{\delta}\right)$. This enables to obtain several advantages, as a more robust estimation at low signal-to-noise ratios or a lower effect of bubble overlapping which makes difficult direct fringe counting (Damaschke et al., 2005 [4]).

9.2 Limits on measured size

It is useful to give lower and upper limits of the measured particle diameter for a given experimental set-up. Regarding the smallest measurable diameters, two different conditions must be satisfied. The first limit, is related to the applicability of the theory of geometrical optics, i.e. to consider only reflected and first order refracted rays in the forward scattering region instead of the whole Lorenz-Mie scattering (Van de Hulst, 1957 [17]). This is possible only if

$$\chi = \frac{\pi d_{min}}{\lambda} \geq 20 \tag{9.6}$$

This relation states a minimum diameter as a function of the light wavelength only. The second lower limit depends on the specific set-up, being related to the size of the camera objective aperture, D_c, and to the distance between camera and object plane, R, through the value of the collecting angle $\alpha = 2arctg(\frac{D_c}{2R})$. This angle should be chosen to allow collecting a sufficient number of fringes to measure the diameter. The smallest measurable particle should display at least two fringes. Knowing the relationship between the collecting angle and fringe angular spacing

$$\alpha = N\ \Delta\theta_r \rightarrow \Delta\theta_r = \frac{\alpha}{2} \tag{9.7}$$

with N number of fringes, from 9.4 the second limit for the minimum measurable diameter can be obtained by considering N=2

$$d_{min} = \frac{K}{\delta_{max}} = \frac{4\,m\,\lambda}{\alpha}\left[cos\left(\frac{\theta_r}{2}\right) - \frac{m\,sin\left(\frac{\theta_r}{2}\right)}{\sqrt{1+m^2-2\,m\,cos\left(\frac{\theta_r}{2}\right)}}\right]^{-1} \tag{9.8}$$

Therefore, this minimum value is dependent on the specific optical setup. Note that in this limit, usually the light wavelength, the relative refractive index and the scattering angle are fixed by the specific fluid mechanics problem (m), by the optimal scattering (θ_r) and by the available equipments (λ). Thus, the remaining possibility is to change α, i.e. the ratio $\frac{D_c}{2R}$ (notice that for small angles this relationship is almost linear). The effective measured minimum diameter will be the largest between the two values obtained from 9.6 and 9.8 (usually the second). Another very important limitation to the minimum measurable size is given to the diffused light associated to each particle image, which gives rise to a low wave-number pedestal which can override the light distribution in the case of a low number of fringes (this is also reported in section 9.4.1) (Damaschke et al. 2000, [2]).

The largest diameter is related to the use of FFT transform to evaluate fringe wavenumber. According to Nyquist sampling theorem, in the case of fringes on the (x,y) plane (i.e. the imaged plane), if a two-dimensional FFT transform is carried out on a finite window sized $l_x \times l_y$ with minimum spatial separation between data equal to Δx and Δy, the highest wavenumber that can be represented to avoid aliasing corresponds to one-half of the minimum separation, i.e. $k_{xmax} = \frac{2\pi}{2\Delta x} = \frac{\pi}{\Delta x}, k_{y_{max}} = \frac{2\pi}{2\Delta y} = \frac{\pi}{\Delta y}$. On the other hand,

the minimum spacing between two adjacent fringes should be $\delta_{min} = 2\,px$, or equivalently each fringe should measure at least $\Delta x = 1\,px$ (similarly along y). However, this is a difficult condition for measurements because it would require an enhanced contrast to distinguish one pixel fringes. For this reason, it seems to be advisable to consider only fringes measuring at least $\Delta x = 2\,px$ and then a minimum spacing of $\delta_{min} = 4\,px$. Thus, from 9.5 the upper measurable particle diameter results to be

$$d_{max} = \frac{K}{\delta_{min}} = \frac{K\,k_{xmax}}{2\pi} = \frac{K}{2\Delta x} = \frac{K}{4} \tag{9.9}$$

as also along y (usually the optical system is arranged to have fringes along one axis, x in this case).

From 9.8 and 9.9 the dynamical range in diameter measurements is

$$\frac{d_{max}}{d_{min}} = \frac{\delta_{max}}{\delta_{min}} \tag{9.10}$$

In a typical experimental setup this dynamical range is lower than 10 (the minimum fringe spacing is 4 px, while the maximum can be around 30 px). Thus, the measurable diameter range derived from 9.8 and 9.9 is between 50 μm and 500 μm. Being cavitation bubbles also smaller than 50 μm, in the present set-up the values of the optical parameters and in particular of the ratio $\frac{D_c}{2R}$ (or equivalently α) is increased as much as possible to decrease the smallest measurable diameter to about 15 μm ($\alpha \sim 0.2rad$). This is obtained by simultaneous decreasing of the distance from the objective to the measuring region (R=500 mm) and increase of objective diameter (D_c=100 mm). By using interrogation windows as large as 64 px (as reported in the next section), the maximum measurable diameter is around 300 μm (for the experimental set-up used for bubble measurement calibration this maximum is limited to about 150 μm).

9.3 Experimental set-up and data processing

9.3.1 Set-up

The ILIDS technique has an experimental setup similar to the one of a PIV-2D investigation. It is fundamentally based on a laser source and a high resolution camera. One of them should be inclined relative to the other. The

illumination source was a Nd-Yag laser which emitted a laser beam at 532 nm with an output energy of 220 mJ per pulse. The laser illuminates a region of about $(15 \times 15)\ cm^2$ having a thickness of about 2 mm. Image acquisition was carried out by a frame straddle camera with a resolution of 1280 x 1024 pixels and 12 bit dynamic range. This camera had an objective with a focal length equal to 60 mm (f/2.8) (one acquisition with a 85 mm f/1.4 objective has been also performed), while the distance between camera and plane was R=500 mm and the objective diameter was about D_c=100mm. Thus the collecting angle is ($\alpha \sim 0.2rad$). A synchronizer allowed acquiring all the images in correspondence to a given phase (angle) of the propeller model rotation. In order to perform also PIV measurements, the interval between two exposures was initially set to 120 μm, so that it was possible a good correlation between two consecutive images. The camera and laser were controlled by dedicated software and the acquired images were stored on a computer hard disk. Measurements were performed at the Italian Navy Cavitation Tunnel (CEIMM) on a Wageningen modified type four blade model propeller (INSEAN E779A), whose features are resumed in table 9.1, as shown in Figure 9.1 where the reference system is also reported.

Number of blades	4
Diameter (mm)	272
Pitch-diameter ratio	1.1
Boss diameter max (mm)	45.5
Rake (degree)	4° 3”
Developed area-disk area ratio	0.688

Table 9.1: *E779A model propeller features*

In connection to this figure, the propeller turns clockwise at about 20Hz. The test section was a square closed jet type (0.6 m 0.6 m 2.6 m) with perspex windows on the four walls which enabled full optical access. The pressure in the water tunnel was equal to 0.6 atm. The laser incoming direction was normal to a lateral window while the camera was placed at an angle of 45°, as reported in Figure 9.1. A prism was used between the cavitation tunnel wall and the camera to minimize the effect of light refraction when changing the refractive index. The value of this angle, called collecting angle, is not arbitrary but it is linked to the scattered light intensities. For air bubbles in water, the scattered light intensities of reflection and first

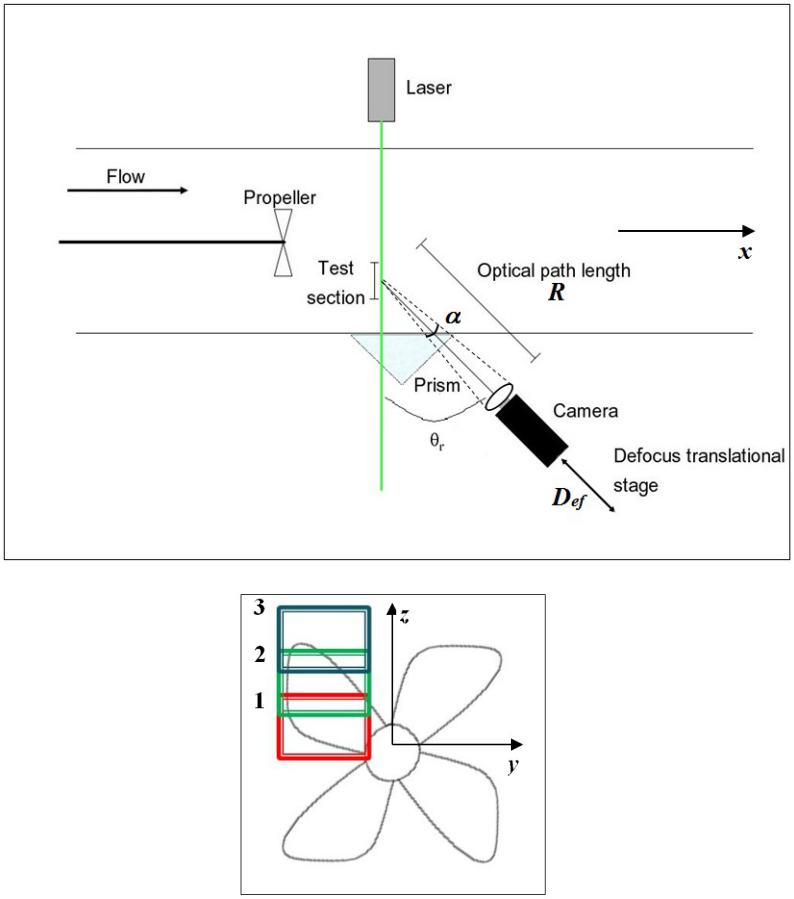

Figure 9.1: Top view of the experimental setup and the three measurement regions on the propeller model with reference system.

order refraction are almost equal just for an angle of 45° (Niwa et al., 2000 [15], Maeda et al. 2000 [14]). The illuminated area, i.e. the measurement section, was located nearly 1D downstream the propeller, in correspondence to the propeller's hub. Image acquisition was performed at different angular positions of the propeller and mean values are obtained by phase averaging 1000 data for each phase angle. The phase averaging has been performed in a region which corresponds to the left side of the propeller model (region 1 at the bottom part of Figure 9.1), while for a single phase (75°) also images in regions 2 and 3 have been acquired.

The present measurements have been performed in order to evaluate the best set-up conditions for size measurements as a function of the defocusing distance (that between the focal plane and the camera-objective system as measured by the defocus translational stage shown in figure 9.1), the size of the imaged field, the phase angle relative to propeller blade position, the objective lens focal length and the number of bubbles per unit volume, which is a function of the advance coefficient J defined as

$$J = \frac{V}{ND}, \tag{9.11}$$

being V the axial velocity at the propeller location (3 m/s) and N the revolutions per second (from 16 s^{-1} to 23 s^{-1}). The Reynolds number of the measurements (based on propeller diameter and axial velocity) is 7×10^5. In Table 9.2, the different experimental conditions are summarized. The fourth column makes reference to the regions previously mentioned and reported at the bottom of Figure 9.1 (the distance of the center of each region from the propeller axis is indicated in the table). The effects of these parameters on bubble size measurements are considered by changing only one of them at each time and keeping the others constant. In particular, the data in Table 9.2 are presented following the order in which each parameter is changed. Among those tested, for each one, the optimal value from the point of view of bubble size probability density distributions is selected and is indicated in bold in the table (except for column 2 and 3 which are not to be evaluated from this point of view) . The results will be detailed in section 9.4.

J	**Def [mm]**	**Phase angle**	**Region [cm]**	**Image field [cm^2]**	**Lens focal length [mm]**
0.83	50	0°	0	**7x6**	**60**
0.73	80	15°	5	11x10	85
0.63	**95**	30°	10		
0.565	110	45°			
		60°			
		75°			
		90°			

Table 9.2: The different parameters used in image acquisitions. In bold the optimal values

9.3.2 Data processing

In this section, the rationale behind the algorithm used for bubble sizing is described as represented in Figure 9.2. At first, each acquired image is converted in the wavenumber domain by direct FFT. Then, the cross-correlation function between this converted image and a reference image is performed. The aim of this operation is to evaluate the location of each bubble inside the acquired image by looking at cross-correlation local maxima. The reference image is simply a circular spot located at the centre of the image as reported in black and white in Figure 9.2. The spot diameter is selected from the average size of imaged bubbles which mainly depends on the defocusing distance. The light intensity profile along this spot is 2D Gaussian so that it is possible to account for slight variations in bubble image size due to changes in camera distance within the imaged region. Around the local maxima detected, a square window is applied (the size of the window is slightly larger than the previous spot diameter) and the auto-correlation function is computed to evaluate fringe wavenumber and then bubble diameter.

In Figure 9.3, an example of original image and of the corresponding cross-correlation with sample image is given. By analysing the bubble positions and size measured from this and similar images, it is obtained that for bubble image overlapping area not larger than 30% it is still possible to distinguish the contributions, whereas this distinction is not possible for higher overlapping. The resulting power spectral density is usually quite detailed as reported in Figure 9.3. By using sub-pixel interpolation, the error on the

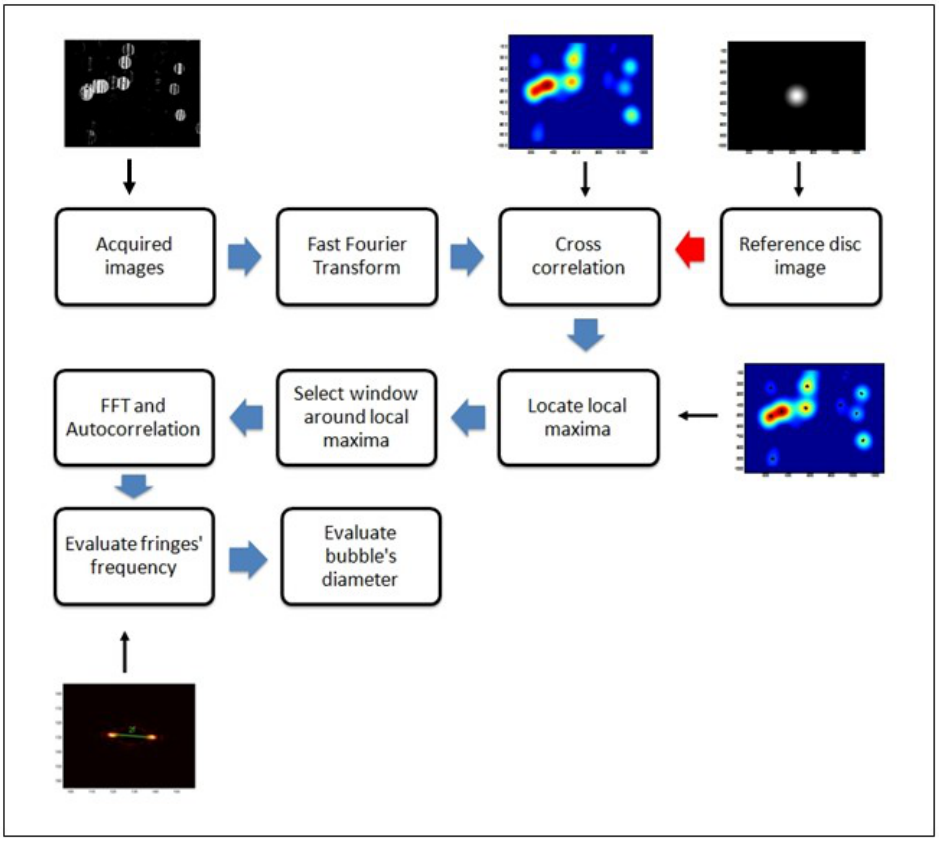

Figure 9.2: Rationale for particle sizing algorithm

measured fringe wave-number is similar to that in PIV (i.e. some fraction of a pixel). Therefore, being the interval among minimum and maximum fringe spacing between 4 pixel and 30 pixel (section 9.2), the relative error on fringe spacing and hence on measured size is not larger than 5 %, i.e. on the same level of PIV velocity measurement error.

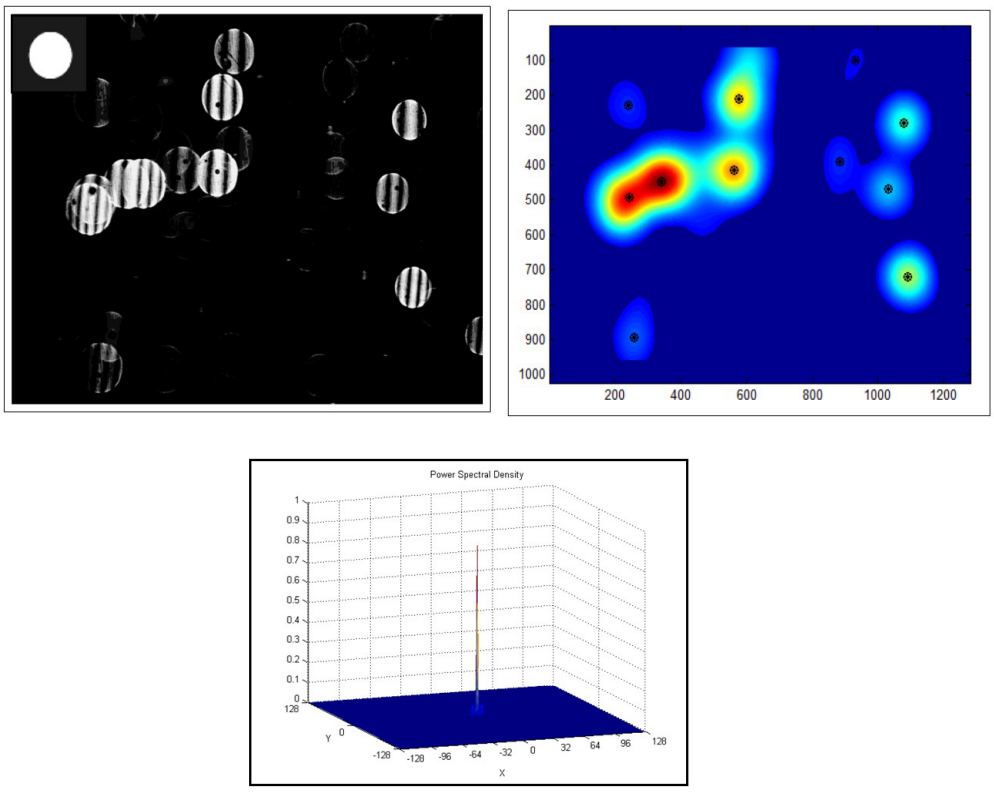

Figure 9.3: Sample image (on the left) and cross-correlation with reference image (on the right). The reference image is given at the top of left figure. An example of power spectral density on the bubble spot is given at the bottom.

For the simultaneous evaluation of bubble velocity, the usual cross-correlation between consecutive images is performed. The images acquired with the present set-up aim to maximize the correct detection of bubble location and size. Specifically, cross-correlated particle patterns are given by linear fringes embedded in a circle as depicted in Figures 9.2 and 9.3 rather than by groups of adjacent enlighten pixels as in usual PIV. Therefore, the resulting number of velocity vectors from each image couple will be much lower than in PIV and each velocity will be referred to a single bub-

ble. In this sense, the velocity measurement is closer to a Particle Tracking Velocimetry (PTV) approach. The size of the interrogation window which allows a good compromise between detection of single bubbles and consecutive fringes is equal to 64 pixel. The two measured velocity components are obtained on the image plane, i.e. the one which identifies the vertical velocity of the bubbles while the other component is inclined by 45° in respect to axial and transverse directions.

9.4 Results

9.4.1 Calibration of size measurements

To validate the measurement set-up, a preliminary calibration has been performed on a small tank in which electric wires generate bubbles by electrolysis. The electrode was made of one coated copper wire (cathode) and one platinum wire (anode), having a diameter equal to 100 μm, placed at a distance of 30 mm one from the other and power supplied at 3.3 V. The optical set-up is as close as possible to the propeller model investigations under similar defocused conditions and in particular the scattering angle between laser emission and camera acquiring direction is the same (45°). This configuration has been selected because air bubbles generated by an electrode, made of two wires of known diameter placed at a given distance and power supplied at a known voltage, have a diameter strictly related to that of the wires. Specifically, the relationship between bubbles and wire diameters is one half, although uniformity and evenness of size can be difficult to ensure, so that usually a Gaussian distribution could be expected (Azar, 1997 [1]). Thus we expected a measured average bubble size equal to 50 μm. This calibration study has been performed using 4000 images and the results in terms of number density distributions of bubble size are reported in Figure 9.4.

There is some remark to be underlined from these results. The distribution appear close to a Gaussian (consider the zoom on the right part of Figure 9.4) with mean value close to the expected one. However, from the left part of Figure 9.4, it can be pointed out that measures of bubble size also between 250 μm and 650 μm are reported. These bubble size measurements should be ruled out by the wire diameter, wire distance and voltage supply. Therefore, there is a source of error which has been related to the

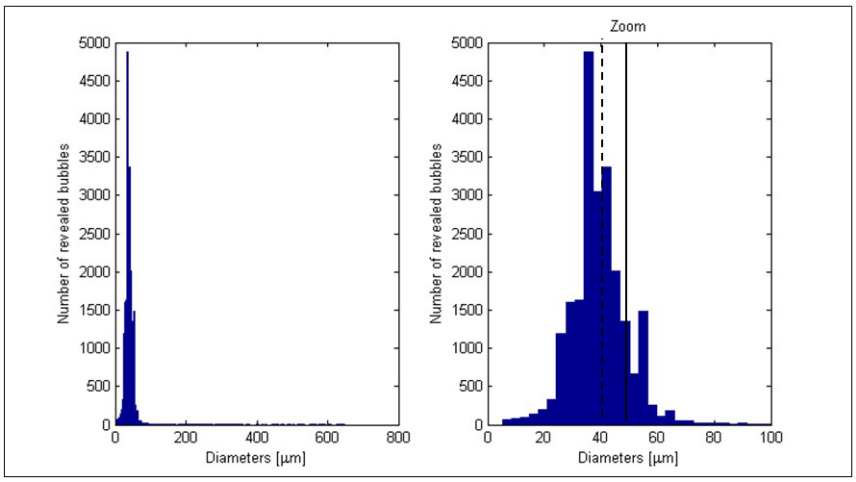

Figure 9.4: Number density distributions of particle size from calibration study with electric wires with a zoom of the region between 0 and 100 μm in the right part. The vertical lines indicate the measured mean value (dotted) and the expected value (continuous).

presence of bubbles smaller than the lower limit. Indeed, the smallest measured size is around 10 μm (which is reasonably closer to the prediction given in section 9.2) just corresponding to only 2 fringes. When the number of fringes is smaller, these bubbles are imaged erroneously as diffused indistinct light with overlapping low wave-number pedestal. Therefore, image analysis could misinterpret them as composed by multiple fringes with separation $\delta_{min} = 1\ px$ (corresponding to about 20 fringes), which from equation 9.9 corresponds to a measured size over 200 μm , i.e. just what observed. This can be filtered out, but one of the aims of this paper is just to point out such problems. In any case, the number of mismatched measurements is less than 5 % of the entire set (about 800 over 20.000 samples, which for the acquired 4000 frames corresponds to one mismatch every five frames). On the other side, the zoom reported in the right part of Figure 9.4 points out another problem, i.e. a systematic error among the expected (around 50 μm) and the measured mean value (around 40 μm). Although the expected value cannot be strictly considered as exact and the measured standard deviation (around 11 μm) could account for the observed differences, this point should be retained as a possible drawback of the present size measurements based on ILIDS. The previous results are in agreement with previous investigations on calibrated spherical particles in air in which

also some systematic deviation has been measured due to fringe overlapping and distortions and to low wave-number contributions due to fringe pedestal (Fiore and Romano, 2003 [5]).

9.4.2 Parametric study of size measurements

The investigation on the propeller wake considers separately the effect of the different parameters previously described. Each acquisition was composed of 1000 images. The pressure in the water tunnel is equal to 0.6 atm. It must be clarified that, in water tunnels cavitation nuclei size distribution is very complicated depending on several variables, such as air content, water tunnel running time, velocity and pressure. As a consequence of the specific values of the previous variables, we expect an average bubble diameter equal to 200 μm (Franc et al., 1995 [6]) with changes in measured diameters of about one order of magnitude, i.e. from 30 μm to more than 300 μm (Liu et al., 1993 [13]). An example of instantaneous acquired image with overlapped measured bubble size is given in Figure 9.5, where almost 10 data are collected. All these parametric investigations are performed on region 1 of Figure 9.1.

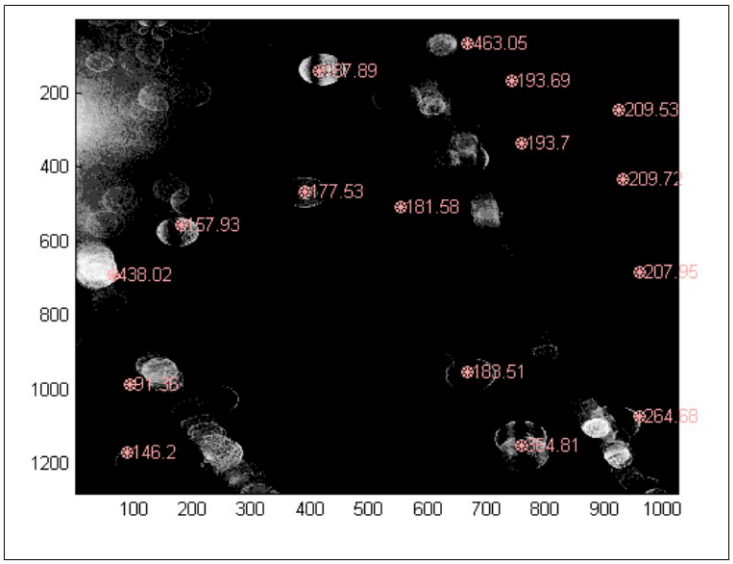

Figure 9.5: Example of acquired image with overlapped measurements of bubble diameters.

The first variable whose influence is studied is the defocusing path length,

Def, which is measured by the displacement of the objective-camera system on the translational stage (figure 9.1), must be different from zero to generate the fringe pattern used to evaluate bubble size. This choice is critical, because while for small Def problems of detecting large diameters are involved (as detailed in the calibration study, a small number of fringes should be misinterpreted as a larger number), for large Def a high overlapping between nearby strongly defocused bubble images is observed. Starting from the minimum working condition, Def=50 mm, also 80 mm, 95 mm and 110 mm have been tested (by keeping constant the other parameters, J=0.83 and phase angle equal to 0). Made non-dimensional by the objective focal length, these values correspond respectively to 0.83, 1.33, 1.58 and 1.83. The results in terms of number density distributions of the diameter measurements are represented in Figure 9.6 .

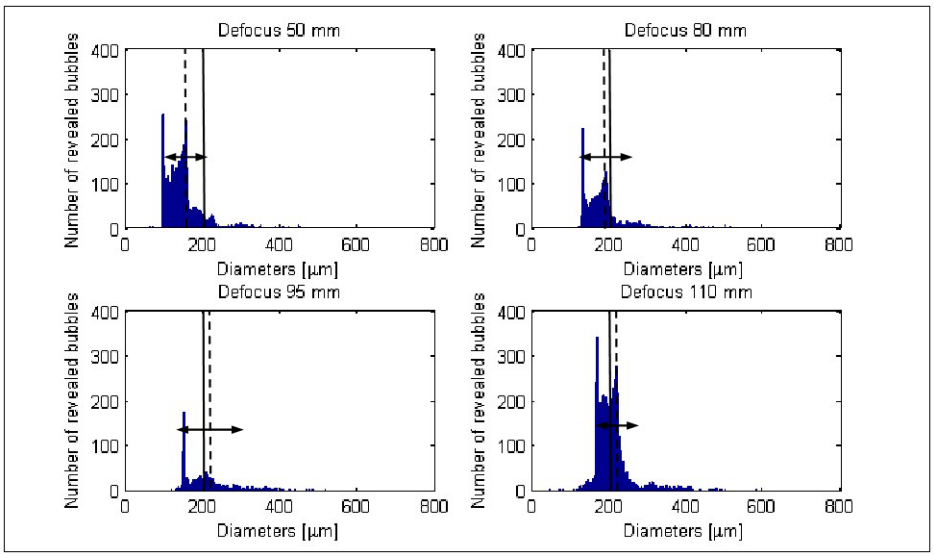

Figure 9.6: Number density distributions of particle size. Effect of defocusing length on measured diameters with J=0.83, phase=0°. The vertical lines indicate the measured mean value (dotted) and the expected value (continuous). The arrows indicate ± one standard deviation around the mean..

From this figure, it is clearly seen how the smaller defocusing path length (Def=50 mm) is not sufficient for a correct measurement of bubble size (as in Figure 9.4, the measured and expected mean values are given as vertical lines, while the interval of two standard deviations around the mean is represented by arrows). For Def=50 mm, there is a large systematic error

(more than 50 μm), even much larger than in the calibration study. By increasing the defocusing length, a better resolution on large diameters is achieved (as reported in sections 9.1 and 9.2) resulting an increasing measured mean value. Indeed, from Figure 9.6, the total number of detected bubbles decreases as Def increases (due to increasing overlapping between bubble images) and simultaneously the measured value approaches the expected one. For Def =95 mm, the best result is obtained even if the result obtained with Def=110 mm cannot be ruled out (the main difference with the previous one being the increased number of measured large size bubbles). Both measured mean value and standard deviation are reasonably close to expected values. At the end, the optimal defocusing distance is obtained as a good compromise between defocused bubble overlapping and fringe resolution. As reported in Figure 9.1, the measurement region involves a large part of the blade tip and the present measurements point out that bubbles from this part of the propeller have an average diameter equal to 200 μm. In each size distribution, a sharp peak close to 150 μm is also observed. This peak is present in all performed measurements also when the propeller is not working. Thus, it has been related to the presence of diffused bubbles in the facility for the given underpressure conditions.

The second parameter investigated is related to the number of bubbles per unit volume by the advance coefficient, J, which is moved progressively closer to the fully-developed cavitation. The direct consequence of this action is an increasing number of bubbles. The reason resides in the fact that constant velocity is selected in the tunnel, so that cavitation conditions and growing number of bubbles are achieved when increasing N, thus lowering J, as noticed from equation 9.11. Indeed, the higher the propeller rotational speed, the larger the inlet side surface portion of the propeller blade where pressure drops below the vapor pressure of water, thus inducing cavitation. The tested values are J=0.83, 0.73, 0.63, 0.565 and the results are represented on Figure 9.7.

From these number density probability distributions, it is clear how the number of measured bubble diameters increases when decreasing J (from about 600 to 20.000). On the other hand, the interval of measured bubble diameters as well as the difference between measured and expected values are not changing significantly (only the standard deviation is slightly decreased). Thus, the present setup allows performing size measurements also

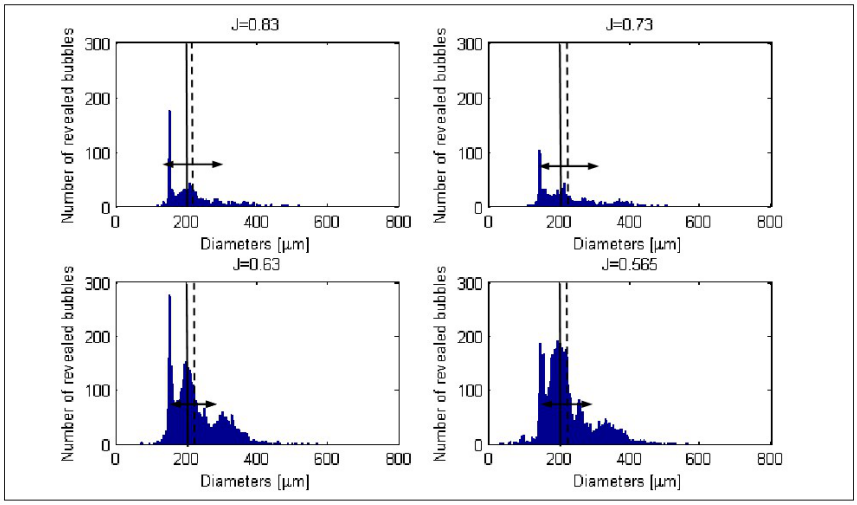

Figure 9.7: Number density distributions of particle size. Effect of advance coefficient, i.e. bubble number on measured diameters with Def=95mm, phase=0°. The vertical lines indicate the measured mean value (dotted) and the expected value (continuous). The arrows indicate ± one standard deviation around the mean.

in experimental conditions in which the number of bubbles is high (on average about 20 bubble size measurements in each frame). However, to avoid too much overlapping between bubbles, the value J=0.63 has been selected for further investigations. It is interesting to note that in addition to the peaks at 150 μm and 200 μm (already considered in Figure 9.6), two other enlarged peaks at 250 μm and 350 μm are measured. Their origin is related to the different cavitating parts of the propeller as reported in the following section 9.4.3.

Before considering these different cavitation bubble sources, two other parameters detailed in Table 9.2 are considered, starting from the effect of the acquired imaged field. This is changed from a small value (with linear side in the order of D/3) to a larger one (in the order D/2) and the results are presented in Figure 9.8.

It is important to point out that this acquisition has been performed at a phase angle different from the previous ones (75° rather than 0°.). The measured mean diameters are almost equal whereas the standard deviation is lower in the case of a large imaged field. Thus, the data obtained with such a large imaged field have a lower size resolution (lower minimum diameter and bin size) in comparison to those obtained with the smaller one. This

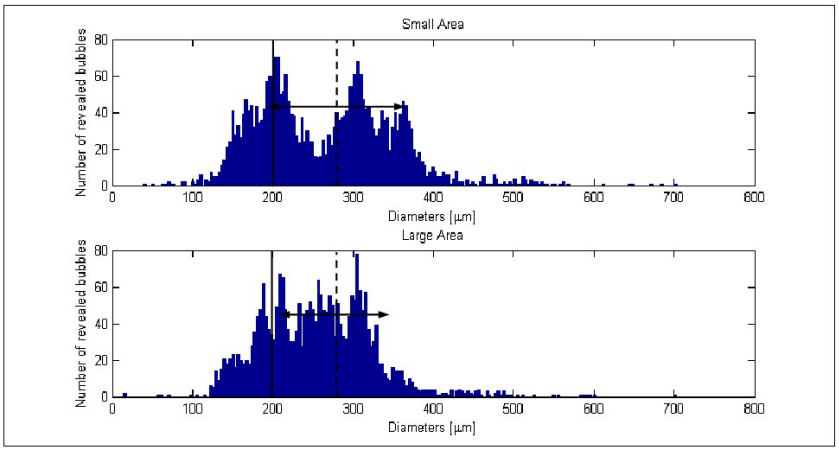

Figure 9.8: Number density distributions of particle size. Effect of imaged field on measured diameters with Def=95mm, J=0.83, phase=75°. The vertical lines indicate the measured mean value (dotted) and the expected value (continuous). The arrows indicate ± one standard deviation around the mean.

is because the use of a large field involves a high defocusing path length to correctly evaluate fringe patterns due to the reduction of collection angle (basically an increase of R, being D_c a constant). Even if for the large imaged field the maximum defocusing distance, Def=180 mm, has been selected, this was still not sufficient to attain the same results of the smaller one with Def=95 mm (due to the different apertures of the two objectives as reported in section 9.3.1). In any case, this is a very important indication of the sensitivity of the diameter measurements to the size of the imaged field. Secondly, the effect of lens focal length is studied by mounting an objective having a focal length equal to 85 mm (rather than 60 mm). Thanks to its higher brightness, which allows acquiring also less luminous bubbles it was possible detecting a larger number of samples. The results obtained are not presented because the effect is similar to the previous case of changing imaged area. Indeed, even for a change in lens focal length, it is necessary to select the correct defocusing length and this fact rules out the larger focal length at least for the present experimental set-up.

9.4.3 Cavitation bubbles in the propeller wake

Making reference to the position of the propeller blade, as reported in Figure 9.1, the effect of the phase angle is evaluated. We have studied positions

spanning from 0 to 90 degrees, on steps of 15° at a time in the region numbered as 1 in Figure 9.1 (the propeller position at a phase angle equal to 0° is just the one displayed in the figure). It is important to point out that measurements are performed at about 1D downstream of the propeller when on the average one revolution of the entire vortex pattern takes place. The size distributions at the different phase angles are given in Figure 9.9, where also the propeller blade positions in relation to the imaged field have been pointed out.

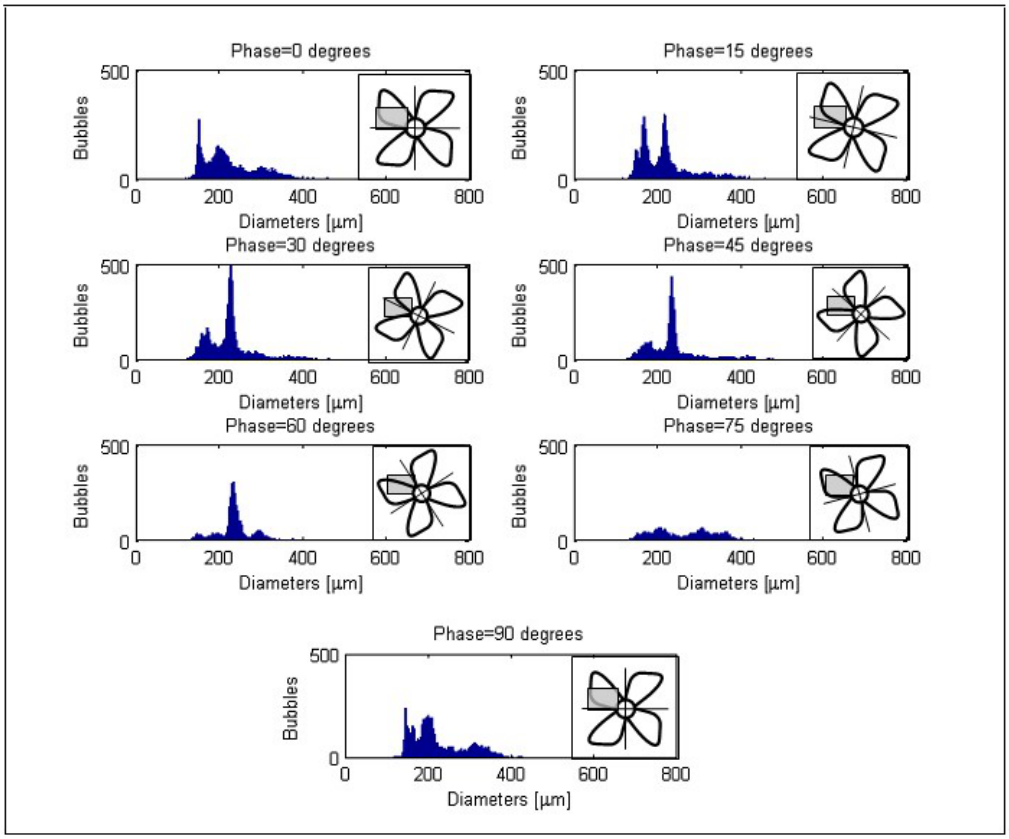

Figure 9.9: Number density distributions of particle size. Effect of phase angle on measured diameters with Def=95mm, J=0.83, with a small imaged area. The propeller blade positions in relation to the imaged field are indicated on the right part of each figure.

The size distributions show that after a rotation of the propeller equal to 90° (i.e. same positions of the blades as at 0°) the bubble size distribution is more or less the same (from the first to the last plot in Figure 9.9), thus confirming the periodicity of the phenomenon linked to the blade rotation.

On the other hand, there are strong differences among the results derived at intermediate phases between 0° and 90° . While the mean size value is almost independent on the phase angle (differences no larger than 10 %), single peaks are raised or damped when changing the propeller phase angle. These facts suggest the idea that the sources of such bubbles are mainly located on different parts of the propeller blades themselves. In particular, a more or less sharp peak around 200 μm is measured in size distributions at all phases as also a peak at about 150 μm which were already noticed in almost all other tests (except possibly for a phase angle equal to 75° where the imaged field is entirely covered by one blade). The first of these two peaks is mainly present at phase angles equal to 90° , 0° , 15° and 30°, i.e. when the blade is partially present in the measurement region. In addition, some smooth peak appears around 250 μm and 350 μm especially at phase angles 30° , 75° , 90° and 0°, i.e. when the blade is passing over the measurement region. These last contributions seem to be the same already observed in Figure 9.7. The previous observations suggest that size contributions around 200 μm are mainly derived from the blade wake (maybe the trailing vortices from the propeller tip), whereas those at 250 μm and 350 μm originate on the blade body surface.

To investigate in more detail the sources of such different size contributions in the propeller wake, the measurements have been performed at different positions as reported in Figure 9.1 (regions 1, 2 and 3, respectively centred at z=5cm, 10 cm and 15 cm from the horizontal plane, i.e. z/D=0.22, 0.44, 0.66 respectively). The attention is focussed onto a phase angle equal to 75°, for which from the previous analysis the major relative contribution of bubbles with size around 250 μm and 350 μm in comparison to 150 μm and 200 μm is observed. From the data reported in Figure 9.10, in comparison to the results obtained in the first region (reported in the previous paragraph), the contribution of size class around 250 μm is at first increasing and then decreasing in comparison to the raising importance of bubble size around 200 μm in regions 2 and 3 (i.e. closer to the propeller tip). On the other hand, the contribution from 350 μm is almost disappearing when moving from region 1 to 2 and 3 (consequently the measured mean values and standard deviation decrease). These observations indicate that while the size class around 200 μm is closely linked to the tip vortex position, the size classes around 250 μm and 350 μm are related to bubbles

generated progressively much closer to the propeller center, i.e. presumably to the central part of the blade and to the hub.

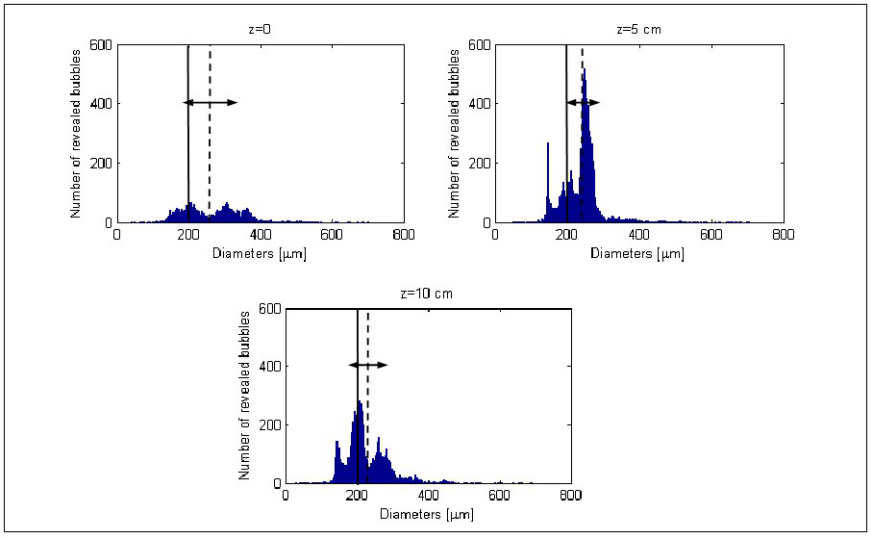

Figure 9.10: Number density distributions of particle size. Results obtained at different positions with Def=95mm, J=0.83, phase=75°, with a small imaged area. The arrows indicate one standard deviation around the mean.

All bubble size contributions from these tests are summarized in Figure 9.11 from which clearly the different classes are pointed out.

Following what previously reported, a possible explanation relating such size contributions to the different part of the propeller is summarized at the top right part of this figure. While the contribution from the hub (diameter around 350 μm) comes from the central part of the propeller disc (in light green) and is measured mainly in region 1, bubbles from the central part of the blades (diameter equal to about 250 μm) are mainly observed in region 2. On the other hand, bubble contributions from the blade tip (diameter about 200 μm) derived from region 3. Of course, due also to some overlapping between the different measurement regions, this separation is not complete and some overlapping is observed among the different contributions from the propeller as also from bubbles diffused into the facility.

9.4.4 Simultaneous measurements of bubble velocity and size

Simultaneously, the velocity field has been measured, by applying image analysis techniques on each image pair of the acquired sequence as described

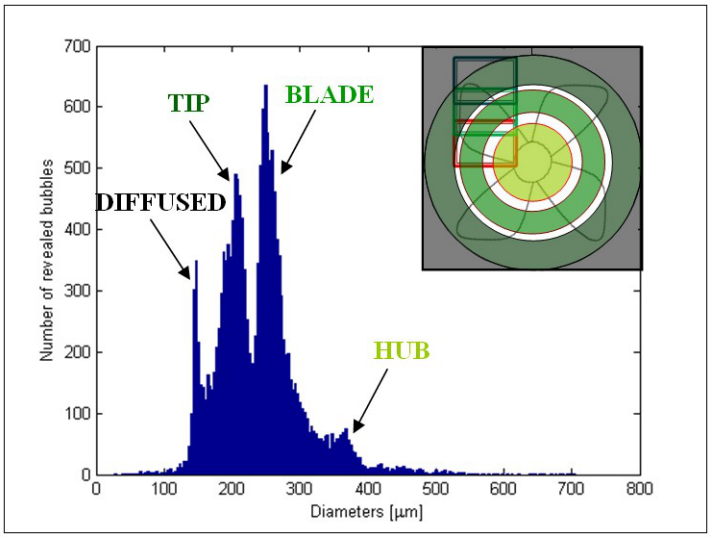

Figure 9.11: Global size distribution along the different positions as derived by overlapping of data from Figure 9.10. The hypothetic contributions from the propeller parts are sketched at the top right corner.

in section 9.3. Figure 9.12 shows examples of instantaneous velocity fields in the three regions along the vertical direction z already described in the previous section in the focal plane.

The different parts of the helicoidal pattern generated by the propeller tip vortex are clearly recognized when moving towards the upper part of the channel. The measured velocity vectors for bubble velocity are in the order of 3 m/s or slightly larger with significant vertical components dependent on the tip vortex position. When averaging all images in the data set at the different positions, an average velocity field can be derived. This is shown in the left part of Figure 13 for the three measured regions at a phase angle equal to 75°.

Note that tip vortex contributions have been eliminated from this figure because it is not located on the camera focal plane and size measurements on that vortex are generally not accurate. Moreover, the tip vortex overlaps onto a part of the imaged field on the focal plane, so that contributions from this part of the field have to be filtered out to avoid erroneous statistics. In such a figure, the measured velocity field shows the velocity vectors more or less aligned along the main flow directions with the deviations due to the helicoidal pattern of the whole flow field. The measured velocity components

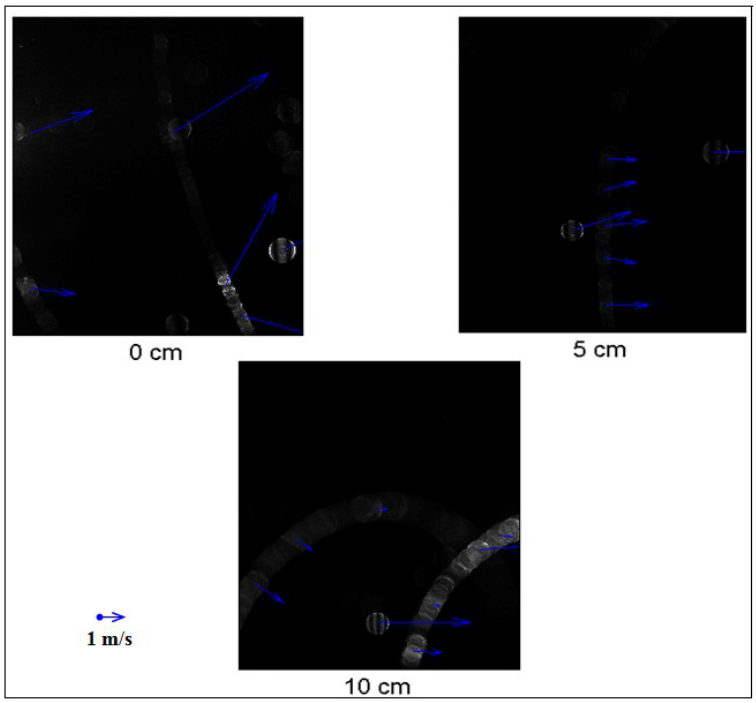

Figure 9.12: Instantaneous bubble velocities obtained at the same positions as in Figure 9.10 (0, 5, 10 cm from the axis).

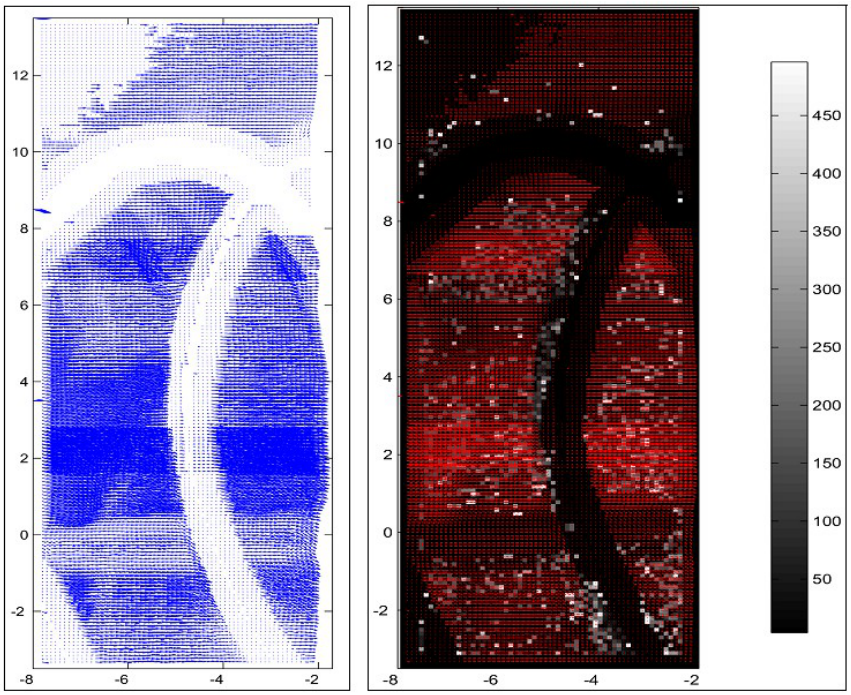

Figure 9.13: Mean velocity field downstream of the propeller model (on the left) and simultaneous measurement of bubble velocity and diameter (on the right, with size scale in μm) on the focal plane. The horizontal and vertical axes are given in cm.

are projected onto the focal plane, so that the vertical velocity component is undisturbed and the horizontal is multiplied by the cosine of the scattering angle (45°). Bubble velocities are not the same along the propeller radius, while showing higher velocities at the centreline (hub wake). Considering also that in this work only bubble velocities are measured (and not that of water), so that the non homogeneous distribution corresponds to the fact that bubbles move in separate clouds (for tip and hub vortices this is rather known). In the same figure (on the right), the simultaneous measurements of bubble size and velocity are overlapped. For each square region over which PIV velocity measurements are computed, the average measured diameter of bubbles in that area is also derived (on the average, in one half of the cases size measurements are not validated and only the velocity measurement is provided). The comments already given from results presented in Figure 9.11 can be here reported into a spatial distribution of measured bubble velocity and size. In particular, measured bubble size of about 200 μm (given in grey colours) is observed close to the tip vortex, whereas bubble diameters as large as 350 μm are revealed far from the tip (in white). The diffused bubbles into the facility are around 150 μm. In Figure 14, the correlation between simultaneously measured bubble velocity and size is given.

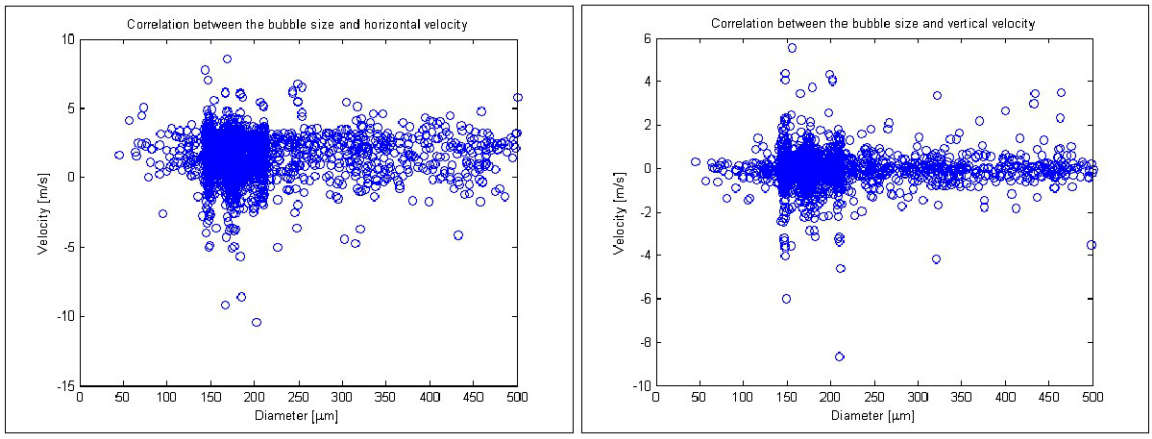

Figure 9.14: Correlation among bubble size and horizontal (on the left) or vertical (on the right) velocity components.

The average vertical velocity is around zero, while the horizontal is around 2 m/s and these values are almost the same for all measured bubble

size. This means that all bubbles move with the same velocity. As derived from the previous description, the bubble size values are contained within the interval 100 μm - 250 μm.

9.4.5 Remarks and conclusions

The main parameters influencing the performances of interferometric imaging methods for particle sizing (namely ILIDS) are investigated. The aim of the work is detecting the optimal set-up to simultaneously measure air bubble size and velocity to detail incipient cavitation phenomena downstream propellers working in hydrodynamic facilities. The technique requires a careful optical alignment due to specific relationships to derive the bubble size especially in comparison to the well tested conditions of solid particles or droplets in air. In particular, the refractive index change from air to water must be taken into account and optical path deviations must be minimized by means of one or more prisms. Moreover, a preliminary system calibration on a small tank using the same set-up as used in the main facility measurements should be performed. Although not strictly necessary, this calibration would contribute to detect the main sources of systematic and random errors in size measurements. Among these sources, the main one derives from incorrect evaluation of the fringe spacing in the case of too large or too small number of fringes with a possible cross-talking between the lower and upper limits. In this sense, the calibration procedure allows deriving the expected limits of measured size in connection to the specific set-up.

In the present measurement, the previous analysis of expected size limits has been performed indicating that the interval of bubble diameters between 15 μm and 350 μm can be detected from the present set-up. For given relative refractive index, laser wavelength and scattering angle, the lower limit depends inversely on the collection angle of the optics, i.e. almost linearly on the ratio between the distance between camera and object and the camera objective aperture. On the other hand, the large diameter limit depends on the maximum number of fringes which can be measured, i.e. on the defocusing distance and interrogation area. The interval selected for the present measurements includes the expected values for air bubble diameters in underpressure conditions (0.6 atm) employed in the cavitation tunnel, i.e. about 200 μm.

Among the parameters to be changed in ILIDS technique, as given in

relation 9.4, the attention has been focused onto the main ones which are the defocusing length, the number of bubbles per unit volume, the extension of the imaged field and the lens focal length. The defocusing length is probably the most important of these and should be optimized also in connection to the imaged field size and to the length focal length. The best results in terms of number density distributions of bubble size measurements have been obtained with a value around 100 mm (i.e. about 1.6-1.7 times the objective focal length). This choice ensures a good compromise between defocused bubble overlapping and fringe resolution. The second important parameter is the number of bubbles per unit volume which has been changed by variations of the advance coefficient, J, which was decreased progressively to values closer to the fully-developed cavitation regime. This parameter has been selected because a high overlapping among bubble images (as in the case of a high bubble number) avoids the correct measure of diameters. On the average, good results are still obtained even when fringes from bubble images are partially overlapped (say area overlapping not larger than 30 %). In terms of number of size measurements per frame, this corresponds to about 30 bubble size measurements per frame. To be conservative, an average number of 20 size measurements per frame should be considered as a good compromise between the highest possible accuracy of each single size result (obtained in the limit of a very small number of measurements per frame) and the high number of samples required to derive significant statistics. Considering the imaged volume size (as reported in section 9.3.1), this limiting number of bubbles per frame corresponds to a limiting bubble density equal to about 50 cm^{-3}. The other parameters which have been tested appear to have secondary importance or to be included in the previous ones (expecially the defocused distance).

Using the best choice of parameters, an investigation on the main sources of cavitating bubbles in the propeller wake has been performed. The analysis suggests that the propeller hub, blade and tip contribute with significantly different size class to the production of cavitation bubbles (respectively around 350 μm, 250 μm and 200 μm) with superimposed ambient bubbles around 150 μm. These distributions overlap together to yield the overall size distribution in the wake which can also be related to the simultaneous measurement of the velocity field (which is influenced by the tip vortex helicoidal pattern).

Appendix Bibliography

[1] Azar K (1997), "Thermal measurements in electronics cooling", CRC Press.

[2] Damaschke N, Nobach H and Tropea C (2001), "Global Phase Doppler Technique for Size and Velocity Measurements", 4^{th} International Symposium on Particle Image Velocimetry. Göttingen, Germany, pp 1-13.

[3] Damaschke N, Nobach H, Nonn T I, Semidetnov N and Tropea C (2002), "Size and Velocity Measurements with the Global Phase Doppler Technique", 11^{th} International Symposium on Application of Laser Tecnique to Fluid Mechanics, Lisbon, Vol 10, Paper 3.

[4] Damaschke N, Nobach H, Nonn T I, Semidetnov N and Tropea C (2005), "Multi-dimensional particle sizing techniques", Experiments in Fluids, Vol 39, pp 336-350.

[5] Fiore L., Romano G.P. (2003), "Simultaneous measurements of particle size and velocity using imaging methods" Proceedings of the 5th International Workshop on PIV, Busan, 2003

[6] Franc J P et al.(1995), "La Cavitation: Mécanismes physique et aspects industriels", Presses Universitaires de Grenoble.

[7] Glover A R, Skippon S M and Boyle R D (1995), "Interferometric laser imaging for droplet sizing: a method for droplet-size measurement in sparse spray systems", Applied Optics, Vol 34, pp 8409-8421.

[8] Hirai S, Okazaki K, Yazawa H, Ito H, Tabe Y and Hijikata K (1997), "Measurement of CO_2 diffusion coefficient and application of LIF in pressurized water", Energy, Vol 22, Paper 2, pp 363-367.

[9] Kawaguchi T, Kobayashi T and Maeda M (2001), "Improvement of interferometric laser imaging for droplet sizing (ILIDS) and application to spray flows", 6^{th} International Congress on Optical Particle Characterisation, Brighton, UK.

[10] Kawaguchi T, Akasaka Y and Maeda M (2002), "Size measurements of droplets and bubbles by advanced interferometric laser imaging technique", Measurement Science and Technology, Vol 13, pp 308-316.

[11] Kobayashi T, Kawaguchi T and Maeda M (2002), "Measurements of spray flow by an improved interferometer laser imaging droplet sizing (ILIDS) system", Laser Techniques for Fluid Mechanics. Springer-Verlag, Berlin, pp 209-220.

[12] Konig G, Anders K and Frohn A (1986), "A new light-scattering technique to measure the diameter of periodically generated moving droplets", Journal of Aerosol Science, Vol 17, Paper 2, pp 157-167.

[13] Liu Z, Sato K and Brennen C E (1993), "Cavitation nuclei population dynamics in a Water Tunnel", ASME Cavitation and Multiphase Flow Forum, 1993. Fluids Engineering Division, FED-153 (153). American Society of Mechanical Engineers, New York, pp. 119-124.

[14] Maeda M., Kawaguchi T. and Hishida K. (2000) Novel interferometric measurement of size and velocity distributions of spherical particles in fluid flows. *Measurement Science and Technology*, **11**, L13–L18.

[15] Niwa Y, Kamiya Y, Kawaguchi T and Maeda M (2000), "Bubble Sizing by Interferometric Laser Imaging", 10^{th} International Symposium on Application of Laser Technique to Fluid Mechanics, Lisbon, Vol 38, Paper 1.

[16] Ragucci R, Cavaliere A and Massoli P (1990), "Drop sizing by laser light scattering exploiting intensity angular oscillation in the Mie Regime", Particle and particle systems characterization, Vol 7, pp 221-225.

[17] Van de Hulst H C (1957), "Light Scattering by Small Particles", John Wiley & Sons, Inc., New York.

Bibliography

[1] R. J. Adrian. Twenty years of particle image velocimetry. *Experiments in fluids*, 39(2):159–169, 2005.

[2] G. K. Batchelor. The theory of axisymmetric turbulence. *Proceedings of the Royal Society A, London*, 186:480–502, 1946.

[3] G. K. Batchelor. *An introduction to Fluid Dynamics*. Cambridge University Press, 2000.

[4] F. Billy, L. David, and G. Pineau. Single pixel resolution correlation applied to unsteady flow measurements. *Measurement Science and Technology*, 15:1039–1045, 2004.

[5] L. W. Browne, R. A. Antonia, and A. J. Chambers. The interaction region of a turbulent plane jet. *Journal of Fluid Mechanics*, 149:355–373, 1984.

[6] S. Chandrasekhar. The theory of axisymmetric turbulence. *Proceedings of the Royal Society A, London*, 242:557–577, 1950.

[7] T. Djeridane, H. Amielh, F. Anselmet, and F. Fulachier. Velocity turbulence properties in the near-field region of axisymmetric variable density jets. *Physics of Fluids*, 8(6):1614–1630, 1996.

[8] G. Falkovich. *Fluid Mechanics - A Short Course for Physicists*. Cambridge University Press, 2011.

[9] U. Frisch. *Turbulence: The Legacy of A. N. Kolmogorov*. Cambridge University Press, 1995.

[10] W. K. George. Processing of random signals. In *Proceedings of the Dynamic Flow Conference*, pages 20–63, 1978.

[11] W. K. George and H. J. Hussein. Locally axisymmetric turbulence. *Journal of Fluid Mechanics*, 233:1–23, 1991.

[12] J. O. Hinze. *Turbulence* 2^{nd} *Edition*. Mc Graw-Hill, New York, 1975.

[13] H. J. Hussein, S. P. Capp, and W. K. George. Velocity measurements in a high-Reynolds-number, momentum-conserving, axisymmetric turbulent jet. *Journal of Fluid Mechanics*, 258:31–75, 1994.

[14] C. J. Kähler and U. Scholz. Transonic jet analysis using long-distance micro PIV. In 12^{th} *International symposium on flow visualization, Göttingen, Germany*, 2006.

[15] R. D. Keane, R. J. Adrian, and Y. Zhang. Super-resolution particle imaging Velocimetry. *Measurements science and technology*, 6:754–768, 1995.

[16] H. W. King. *Handbook of Hydraulics*. Mc Graw Hill, New York, 1918.

[17] A. N. Kolmogorov. Dissipation of energy in locally isotropic turbulence. *Doklady Akademii Nauk SSSR (reprinted in Proceedings: Mathematical and Physical Sciences (1991) Volume 434 Pages 15-17)*, 32:16–18, 1941.

[18] A. N. Kolmogorov. The local structure of turbulence in incompressible viscous fluid for very large reynolds numbers. *Doklady Akademii Nauk SSSR (reprinted in Proceedings: Mathematical and Physical Sciences (1991) Volume 434 Pages 9-13)*, 30:9–13, 1941.

[19] H. Lamb. *Hydrodynamics*. Cambridge University Press, 1895.

[20] P. Lavoie, G. Avallone, F. De Gregorio, G. P. Romano, and R. A. Antonia. Spatial resolution of PIV for the measurement of turbulence. *Experiments in Fluids*, 43:39–51, 2007.

[21] C. L. Lubbers, G. Brethouwer, and B. J. Boersma. Simulation of the mixing of a passive scalar in a round turbulent jet. *Fluid Dynamics Research*, 28:189–208, 2001.

[22] J. Mi, P. Kalt, G. J. Nathan, and C. Y. Wong. Piv measurements of a turbulent jet issuing from round sharp-edged plate. *Experiments in Fluids*, 42:625–637, 2007.

[23] J. Mi, D. S. Nobes, and G. J. Nathan. Mixing characteristics of axisymmetric free jets from a contoured nozzle, an orifice plate and a pipe. *Journal of Fluids Engineering - Transactions of the ASME, 2001*, 123(4):878–883, 2001.

[24] J. H. Michell. On the Theory of Free Stream Lines. *Philosophical transactions of the Royal Society A*, 181:389–431, 1890.

[25] J. Nogueira, A. Lecuona, and P.A. Rodriguez. Limits on the resolution of correlation piv iterative methods. fundamentals. *Experiments in fluids*, 39(2):305–313, 2005.

[26] N. T. Obot, M.L. Graska, and T.A. Trabold. The near field behaviour of round jets at moderate reynolds numbers. *The Canadian Journal of Chemical Engineering*, 62:587–593, 1984.

[27] N. R. Panchapasekan and J. L. Lumley. Turbulence measurements in axisymmetric jets of air and helium. Part 1: Air Jet. *Journal of Fluid Mechanics*, 246:197–223, 1993.

[28] F. Pereira and M. Gharib. Defocusing digital particle image velocimetry and the three-dimensional characterization of two-phase flows. *Measurements science and technology*, 13:683–694, 2002.

[29] S. B. Pope. *Turbulent flows*. Cambridge University Press, 2000.

[30] A. K. Prasad. Stereoscopic particle image velocimetry. *Experiments in fluids*, 29:103–116, 2000.

[31] A. K. Prasad and K. Jensen. Scheimpflug stereocamera for particle image velocimetry in liquid flows. *Applied optics*, 34(30):7092–7099, 1995.

[32] W. R. Quinn. On mixing in an elliptic turbulent free jet. *Physics of Fluids*, 1(10):1716–1722, 1989.

[33] W. R. Quinn. Upstream nozzle shaping effects on near field flow in round turbulent free jets. *European Journal of Mechanics B/Fluids*, 25:279–301, 2005.

[34] M. Raffel, C.E. Willert, S.T. Wereley, and J. Kompenhans. *Particle Image Velocimetry - A Practical Guide*. Springer, 2007.

[35] N. Rajaratnam. *Turbulent Jets.* Elsevier Publishing Co., Amsterdam and New York, 1976.

[36] C. D. Richards and W. M. Pitts. Global density effects on the selfpreservation behaviour of turbulent free jets. *Journal of Fluid Mechanics*, 245:417–435, 1993.

[37] L. F. Richardson. *Weather Prediction by Numerical Process.* Cambridge University Press, 1922.

[38] W. Rodi. A new method of analyzing hot-wire signals in highly turbulent flow, and its evaluation in a round jet. *DISA Information*, 17:9–18, 1975.

[39] G. P. Romano and R. A. Antonia. Longitudinal and transverse structure functions in a turbulent round jet: effect of initial conditions and reynolds number. *Journal of Fluid Mechanics*, 436:231–248, 2001.

[40] G. P. Romano and M. Falchi. Recovering isotropy in turbulent jets. In 8^{th} *International ERCOFTAC Symposium on engineering turbulence modelling and measurements, Marseille, France*, 2010.

[41] F. Scarano. Iterative image deformation methods in PIV. *Measurement Science and Technology*, 13:R1–R19, 2002.

[42] F. Scarano. Theory of non-isotropic spatial resolution in PIV. *Experiments in Fluids*, 35:268–277, 2003.

[43] A. Stitou and M. L. Riethmuller. Extension of piv to super resolution using ptv. *Measurement Science and Technology*, 12:1398–1403, 2001.

[44] G. I. Taylor. Statistical theory of turbulence. *Proceedings of the Royal Society of London. Series A, Mathematical and Physical Sciences*, 151(873):421–444, 1935.

[45] H. Tennekes and J. L. Lumley. *A first course in turbulence.* The MIT Press, Cambridge, 1972.

[46] A. A. R. Townsend. *The structure of turbulent shear flow, 2nd edn.* Cambridge University Press, Cambridge, 1976.

[47] C. Tropea, A. Yarin, and J. Foss. *Springer Handbook of Experimental Fluid Mechanics*. Springer, 2007.

[48] J. Westerweel, D. Dabiri, and M. Gharib. The effect of a discrete window offset on the accuracy of cross-correlation analysis of digital piv recordings. *Experiments in Fluids*, 23:20–28, 1997.

[49] J. Westerweel, P. F. Geelhoed, and R. Lindken. Single-pixel resolution ensemble correlation for micro-PIV applications. *Experiments in Fluids*, 37:375–384, 2004.

[50] B. Wieneke and S. Taylor. Fat-sheet piv with computation of full 3d-strain tensor using tomographic reconstruction. In *13th international symposium on applications of laser techniques to fluid mechanics, Lisbon, Portugal, paper*, volume 13, 2006.

[51] C. Willert. Stereoscopic digital particle image velocimetry for application in wind tunnel flows. *Measurements science and technology*, 8:1465–1479, 1997.

[52] C. Willert. Assessment of camera models for use in planar velocimetry calibration. *Experiments in Fluids*, 41:135–143, 2006.

[53] I. Wygnanski and H. Fiedler. Some measurements in the self-preserving jet. *Journal of Fluid Mechanics*, 38:577–612, 1969.

[54] G. Xu and R. A. Antonia. Effect of different initial conditions on a turbulent round free jet. *Experiments in Fluids*, 33:677–683, 2002.

Publications

Peer-reviewed journal articles:

- G. Lacagnina, S. Grizzi, M. Falchi, F. Di Felice, G. P. Romano. "Simultaneous size and velocity measurements of cavitating microbubbles using interferometric laser imaging", Experiments in Fluids, Volume 50, Number 4, 1153-1167 (2011).
- G. Lacagnina, G. P. Romano. "PIV investigations on small-scales and spatial resolution in the near-field of an orifice jet", submitted to Experiments in Fluids.
- G. Lacagnina, G. P. Romano. "Comparison between planar and volumetric techniques in the study of a turbulent jet", in preparation.

Papers in Conference Proceedings:

- G. Lacagnina, G. P. Romano."Experimental study on large and small scale turbulence in an orifice plate jet", XVIII A.I.VE.LA. (Associazione Italiana di Velocimetria Laser) national meeting, Rome 16-17 December 2010.
- G. Lacagnina, G. P. Romano."Effects of spatial resolution on PIV investigation of a turbulent orifice jet", 16th International Symposium on Applications of Laser Techniques to Fluid Mechanics, Lisbon 9-12 July 2012.
- G. Lacagnina, G. P. Romano. "Comparison between planar and volumetric velocimetric techniques applied to a turbulent jet", 10th International Symposium on Particle Image Velocimetry, Delft, 1-3 July 2013, accepted for oral presentation.